UNIVERSITÀ della CALABRIA
Facoltà di Ingegneria
Dipartimento di Meccanica

Scuola di Dottorato "Pitagora" in Scienze Ingegneristiche

Dottorato di Ricerca in Ingegneria Meccanica XXII Ciclo

SETTORE SCIENTIFICO DISCIPLINARE: ING-IND/08

Tesi di Dottorato

CFD Investigation of the Seakeeping Behavior of a Catamaran Advancing in Regular Waves by an Unsteady RANS Code

Coordinatore

Prof. Sergio Rizzuti

Supervisori

Prof. Sergio Bova

Prof. Frederick Stern

Candidata

Ing. Teresa Castiglione

Dissertazione finale sottomessa per ottenere il titolo di Dottore di Ricerca in Ingegneria Meccanica

Anno Accademico 2008/2009

Contents

List of symbols iii

Introduction

I.1 Background I.1
I.2 Objectives I.3
I.3 Thesis Outline I.6

Chapter 1 – Ship Hydrodynamics and the Use of Models in Ship Design

1.1 Introduction 1
1.2 Ship Resistance 2
1.2.1 Viscous resistance 3
1.2.2 Wave-making resistance 9
1.3 Model testing of ship resistance 13
1.4 Effects of ship geometry on resistance 16

Chapter 2 – The Role of CFD in Ship Hydrodynamics and Use of the URANS Code CFDSHIP-Iowa

2.1 Introduction 20
2.2 State of the art 21
2.3 Reynolds Average Navier-Stokes Equations 23
2.4 CFDShip-IOWA 25
2.4.1 Governing differential equations 26
2.4.2 Turbulence modeling 28
2.4.3 Free surface modeling 30
2.4.4 Rigid body equations and 6DOF module 33
2.4.5 The code SUGGAR 35
2.4.6 Numerical modeling and solution strategy 36

Chapter 3 – Simulation Conditions for predicting the Seakeeping Behavior for Delft Catamaran in Regular Head Waves

3.1 Introduction 41
3.2 Model Geometry and Test Conditions 43
3.3 Grids 46
3.4 Initial and Boundary Conditions 48
3.5 Verification and Validation 49

Chapter 4 – Computational Results for the Delft Catamaran

4.1 Introduction 55
4.2 Natural frequency 57
4.3 Ship motions 59
4.4 Effects of wave steepness on ship response 68
4.5 Total resistance coefficient in waves 70
4.6 Calm water tests 73
4.7 Added resistance in waves 75
4.8 Verification and Validation for the DELFT Catamaran 77

Chapter 5 – Circulating Water Channel for Experimental Test on Ship Models

5.1 Introductions 81
5.2 Background 82
5.3 Channel description 83
5.4 The PIV system 86
5.5 Model tests 87

Conclusions 91

Appendix 93

References 100

Acknowledgements

List of symbols

A	area, wave amplitude
$\underline{a}$	outward pointing area vector
AIAA	American Institute of Aeronautics and Astronautics
Ak	wave steepness
AP	after perpendicular
$\underline{a}_r$	non-inertial acceleration
A_{SS}	area of the superstructure of a ship
ATTC	American Towing Tank Conference
Aw	water-plane area
B	beam
b	wave width, damping coefficient
b_i^k	metrics of transformation from physical domain to computational domain
c	spring coefficient
C_B	block coefficient
C_D	drag coefficient
C_f	friction coefficient
C_{f0}	friction coefficient of the equivalent flat plate
CFD	computational fluid dynamics
C_{FORM}	resistance form coefficient
$C_{k(t\ or\ G)}$	correction factor (time step or grid)
COG	center of gravity
C_R	residuary resistance coefficient
$C_{R,M}$	residuary resistance coefficient of model
$C_{R,S}$	residuary resistance coefficient of full scale ship
C_T	total resistance coefficient
C_{TM}	total resistance coefficient of model
C_V	viscous resistance coefficient
C_{VM}	viscous resistance coefficient of model
C_W	wave-making resistance coefficient
C_{WM}	wave-making resistance coefficient of model
D	draft, benchmark data
E, E_C	comparison error, corrected
EFD	experimental fluid dynamics
E_W	energy of wave system
f	non-dimensional encounter frequency

F_1	blending function in turbulence model
fe	encounter frequency
$\underline{F}_e$	force on ship in *(X,Y,Z)*
$\underline{F}_{e,f}$	force on ship due to frictional actions
$\underline{F}_{e,p}$	force on ship due to pressure actions
FFT	fast Fourier transform
Fn	Froude number
f_n	ship natural frequency
FP	fore perpendicular
$\underline{F}_S$	force on ship in (x,y,z)
f(t)	exciting load
g	acceleration of gravity
H_W	wave height
ITTC	International Towing Tank Conference
J	Jacobian of transformation from physical domain to computational domain
J_1	transformation matrix from *(X,Y,Z)* to *(x,y,z)*
k	form factor, wave number, turbulent kinetic energy, input parameter in convergence study (i.e. grid size, time step)
KCG	vertical center of gravity
L	ship length
LCG	longitudinal center of gravity
LDV	laser doppler velocimetry
L_{OA}	length overall
L_{PP}	length between perpendiculars
L_W	length of waves
L_{WL}	length of designer's load waterline
m	solution number in convergence study
M	coefficient in C_f formulation according Prandtl-Von Karman, moment
M_e	moment acting on ship in *(X,Y,Z)*
M_S	moment acting on ship in *(x,y,z)*
$\underline{n}$	surface normal vector
n_a	neighbor point in air
n_w	neighbor point in water
p	pressure, distance between two hulls
P_E	power
p_{int}	pressure at the interface
PIV	particle image velocimetry
$p_{k(t\ or\ G)}$	order of accuracy of numerical solution(time step or grid)
P_P	propeller power
$\underline{R}$	position vector of *(x,y,z)* origin in *(X,Y,Z)*
$\underline{r}$	position vector in *(x,y,z)*
R_A	air resistance

RANS	Reynolds Average Navier-Stokes
RAO	response amplitude operator
Re	Reynolds number
R_f	frictional resistance
$R_{k(t \text{ or } G)}$	ratio between solution changes (time step or grid)
$r_{k(t \text{ or } G)}$	refinement ratio (time step or grid)
R_P	pressure resistance
R_R	residuary resistance
$R_{R,M}$	residuary resistance of the model
$R_{R,S}$	residuary resistance of the ship
R_S	ship resistance
R_T	total resistance
R_V	viscous resistance
R_W	wave-making resistance
$\underline{S}$	position vector in *(X,Y,Z)*
S, S_C	simulation value, corrected
SDB	simulation based design
t	instantaneous time in physical domain
T	draft, wave period, truth
TF	transfer function
T_P	force developed by propeller
$\underline{U}$(U,V,W)	Reynolds-averaged velocity components
U_0	reference velocity (ship speed)
$\underline{U}_b$	velocity of the vessel in *(x,y,z)*
U_D	experimental data uncertainty
U_G	grid size uncertainty
$\underline{U}_G$	velocity of *(x,y,z)* origin
U_I	iteration uncertainty
U_i	flow velocity component in the *i* direction
u_i	Reynolds-averaged velocity component in the *i* direction
u'_i	fluctuating velocity component in the *i* direction
$U_{k(t \text{ or } G)}$	numerical uncertainty (time step or grid)
$U_{kc(t \text{ or } G)}$	corrected numerical uncertainty (time step or grid)
$\underline{U}_r$	fluid velocity vector in *(x,y,z)*
U_{SM}	simulation modeling uncertainty
U_{SN}	simulation numerical uncertainty
U_t	time step size uncertainty
$\underline{U}_V$(u,v,w)	vessel velocity in *(X,Y,Z)*
U_V	validation uncertainty
(X,Y,Z)	absolute inertial earth-fixed reference frame
(x,y,z)	non-inertial ship-fixed reference frame
$x_3(t)$	heave motion
$x_5(t)$	pitch motion

x_{3_1}	first harmonic amplitude of heave motion
x_{5_1}	first harmonic amplitude of pitch motion
x_i	coordinate in the *i* direction
y^+	wall coordinate

Greek symbols

(ξ,η,ζ).	curvilinear coordinates
Δ	displaced volume
ΔF	interference effect between hull and propeller
Ω	angular velocity
β^*	turbulence model constant
β_1, β_2	turbulence model constant
$\delta_{(t, G, I)}$	error (time step, grid or iteration)
$\delta^*_{(t, G, I)}$	error estimate with sign and magnitude (time step, grid or iteration)
δ^*_{RE}	error estimate using Richardson Extrapolation approach
$\delta C_T/A^2$	added resistance coefficient
δ_D	experimental data error
δ_{ij}	Kroenecker Δ
δ_S, δ_{SC}	simulation error, corrected
$\delta_{SM}, \delta_{SMC}$	simulation modeling error, corrected
$\delta_{SN}, \delta_{SNC}$	simulation numerical error, corrected
ε	turbulent dissipation
$\varepsilon_{k(t \text{ or } G)}$	solution change (time step or grid)
ϕ	level-set function, roll angle
γ_{x3}	heave phase
γ_{x5}	pitch phase
η	propulsion efficiency, relative distance between grid points and interface, Euler angles vector
φ	generic variable
κ	turbulence model constant
λ	wavelength, ratio between full scale length and model length
μ	dynamic viscosity
μ_t	turbulent dynamic viscosity
ν	kinematic viscosity
ν_t	turbulent kinematic viscosity
θ	pitch angle
ρ	water density
ρ_A	air density

$\rho\overline{u'_i u'_j}$	Reynolds stresses
$\sigma_{k1,k2}$	turbulence model constant
$\sigma_{\omega1,\omega2}$	turbulence model constant
τ	instantaneous time in computational domain
τ_{ij}	newtonian stress
τ_w	frictional stress on hull surface
ω	specific turbulent dissipation
ω_n	ship natural pulsation
ψ	yaw angle
$\zeta(x,t)$	wave elevation

Introduction

I.1 Background

One of the most important aspects of ship design is to improve safety and efficiency of ship hulls in response to environmental impact. A ship is a buoyancy body providing freight or people transportation in different sea conditions at prescribed speeds. According to service speed, ships are usually classified as displacement, semi-displacement or planing vessels, and they exhibit different behavior and are used for different applications. However, independently of the specific application, in the ship design the following common requirements have to be satisfied:

I. Buoyancy
II. Stability
III. Good seakeeping behavior
IV. Structural strength
V. Maneuvering

Usually a ship is optimized in calm water conditions, but a good behavior of the hull in calm water does not mean also a good behavior in seaway. For a high speed vessel a good seakeeping behavior is a very important feature, if we consider that in seaway it should have large vertical resonant motions. This was shown by a simple experiment made by some students [5]. They studied a catamaran, which is usually classified as a high speed vessel, in which each of the two side hulls had a very small beam-to-draft ratio. Even though this granted a very good behavior for resistance, in seakeeping conditions the vessel jumped out of water when the wave period was in resonant heave and pitch conditions. This and other examples found in literature, demonstrate that hydrodynamic optimization studies must consider resistance, propulsion, maneuvering and seakeeping. The above requirements depend on the hull shape. Therefore the main task for hydrodynamicists is the optimization of hull shape but also the determination of the best combination of hull/propeller that satisfies the requirements of maximum performances and maximum efficiency.

The performances of ships are actually assessed by model testing. This technique, introduced by William Froude in late '800 [8,9], is nowadays still used to verify ship resistance and propulsion performances and represents a milestone in experimental ship hydrodynamics. The early attempts to predict ship resistance and to evaluate the influence of hull shape on resistance and ship motion are referred to Leonardo da Vinci [43], who conducted some experiments on three ships having different shapes at bow and stern. Also

Bernouilli and Eulero worked on theories about ship design but they did not find any practical application. In 1721 Emanuel Swedenborg was the first scientist to suggest the use of model tests in predicting ship resistance, and, after that, many towing tanks were built. Some interesting results were obtained about the influence of bow and stern shapes on resistance, but many doubts affected the predictions on resistance itself for two main reasons:

I. The waves created in the tank by towing the model were more prominent than the ones created by the ship advancing in the sea;
II. The effects of viscosity were not well known and the scaling law from model to ship was unclear.

Therefore only experience and empirical techniques were the guidelines for ship constructors and resistance was studied towing the ships in real dimensions in the sea.

William Froude was sure of the advantages of model testing and in 1870 he had the authorization by British Admiralty to conduct the experiences on models that led him to the formulation of the transfer law from model to ship [8]. The towing tests were carried in the sea with a ship having length L=52,6m and displacement of 1157 tons, and the relation between the resistance and the ship speed was investigated. The same geometry with scaling factor of 1:16 was tested in the towing tank with a speed ratio between model and ship proportional to the square root of length ratio and the comparison of the curve of resistance of both model and ship were very similar in shape. During the experiences, he also observed that the wave configurations created both by the ship and the model advancing in calm water were precisely similar and this led him to distinguish the components of resistance acting on the ship in wave-making resistance and friction resistance, treating them independently. According to his theory, only the component of resistance due to waves could be transferred from the model to ship while frictional and eddy resistance both for model and ship were calculated by empirical formulas derived from experiments on flat plates. Combining both components of resistance, the total resistance of model and consequently of ship could be calculated. A more detailed description of the scaling method will follow in the next chapters.

Since William Froude, ship design is based on towing tank tests that have been standardized by procedures developed by International Towing Tank Conference (ITTC). The actual towing tanks, besides measuring model resistance, are equipped with advanced instrumentations that allow more detailed analysis of the flow field around the model and in the wake region to study the flow around the propeller, giving a better understanding of ship hydrodynamics. Optical measurement techniques based on laser as Laser Doppler Velocimetry (LDV) and Particle Image Velocimetry (PIV), have provided a deep insight into complex flow fields like ship flows. LDV allows measurements of velocity vector at prescribed points of complex flow field with high accuracy and information on the mean and fluctuating velocity is obtained. LDV has some limitations deriving from being a single point

measurement technique. In fact, it requires long periods of operation to get a whole velocity field but it is also difficult to reconstruct the spatial characteristics of large structures found in complex flows. Recently, another laser technique that has found wide application in naval field is the Particle Image Velocimetry (PIV). This technique overcomes the limits related to the single-point techniques allowing whole field measurements and then reducing the testing times.

In addition to EFD (Experimental Fluid Dynamics), CFD (Computational Fluid Dymanics) codes predicting ship behavior were developed and nowadays offer a valid support to ship design. In fact, a design process based only on experiments is quite expensive and time consuming consisting on repeated building and testing on models of candidate designs. The increasing predictive capabilities of Reynolds-Averaged Navier-Stokes CFD codes are revolutioning the design process leading, combined with optimization tools, to the simulation based design. Today the CFD technology is not enough mature to become an alternative to the traditional build & test technique. However, improvements in numerical methods can be achieved by a proper interaction with EFD that gives experimental benchmark data used for codes validation.

The present work is an attempt to apply the Unsteady RANS codes to high speed multi-hull ships that are of increasing interest for different applications including fast ferries, fast cargo ship and fast combatants requiring innovative hull design.

I.2 Objectives

The main objective of the present work is to investigate the behavior of a high speed catamaran advancing in regular waves, using the Unsteady RANS Code CFDShip-Iowa V.4.

Why a catamaran?

The increasing interests for catamarans has to be seen in the context of the rapid socio-economically driven development of international trade. The concept of maximizing speed and keeping the installed propulsion power at the lowest possible levels to ensure the economic viability for the waterborne vessels, has become extremely important. This goal can be achieved by minimization of resistance, that for conventional monohulls would require very small beam, very large hull length and limited displacement. That would have an adverse effect on the stability characteristics and the payload capacity in terms of weights and areas.

The advantages that catamarans offer can be summarized in the following points:

I. The separation between the catamaran side hulls provides adequate stability

II. The slenderness of the hulls provides superior resistance

characteristics

III. The rectangular platform generated by the cross structure provides attractive layout possibilities to the vessel, performing almost any kind of operation such as passengers, cars, container carrying or even be used in military applications.

In the present work, the main focus is on the seakeeping behavior of the DELFT catamaran, designed and tested at Delft University of Technology [44], for which experimental data are available.

In particular, heave and pitch motions will be predicted for different ship speeds and wavelength ranges, and the effects of resonance and exciting forces of the incoming wave on maximum response of the catamaran are investigated. Previous studies focused on resonance conditions for monohulls [15,39] while no literature exist on the response of multi-hull vessels to waves effects.

Another important issue that will be considered in ship response, is the evaluation of the effects of the incoming wave steepness on ship motions, therefore linearities and non-linearities in ship behavior with wave amplitude will also be investigated.

Finally the influence of waves on resistance is also a relevant aspect to consider for a ship advancing in seaway. This component, called added resistance, is a consequence of interaction between incident waves and the ship and this aspect, and the parameters that affect it, will also be studied in the present work.

Why the use of CFD?

As previously mentioned, CFD is becoming a fundamental tool in ship design and optimization for at least two reasons:

I. It gives a deep insight in the flow physics, calculating all the flow variables (local or global) in the whole computational domain and therefore gives a better understanding of complex flows, of turbulence and vortical structures that are common in ship flows;

II. It is less time consuming and less expensive than build & test technique.

The application of RANS codes to predict ship motions in seaway is very recent. The early applications of RANS methods have been devoted to the problem of steady resistance and propulsion, where the problem of ships advancing in calm water at constant speed without and with propeller was modeled. Actually a high accuracy in resistance predictions has been demonstrated in the results presented in the Gothenburgh 2000 Workshop [17] on CFD in Ship Hydrodynamics. Difficulties arise in modeling a ship advancing in waves and dynamic effects have generally been neglected in the actual design process due to the complexity of simulating unsteady flows. This has lead to the separation of the three main aspects of ship analysis in the areas of resistance and propulsion, seakeeping and maneuvering. Seakeeping problems involve the response, in terms of ship motions, of the ships advancing on a straight course in regular waves, depending on ship speed and

wavelength. In fact, due to the interaction between the hull and the incoming waves, a ship undergoes motions in the vertical plane consisting in vertical translation (heave motion) and rotation (pitch motion). Maneuvering attitude of ships is an other important issue to analyze. For instance, emergency maneuvers may be necessary to avoid collisions especially for high speed vessels. Hence maneuvering tests are usually performed in calm water conditions as the turning circle maneuver and the zigzag maneuver and in both cases the ship undergoes translation (sway and surge) and rotation (yaw and roll) motions in the horizontal plane.

Traditionally these problems have been treated as separate issues and modeled using the strip theory where no viscous effects were included. Recently, predictive capabilities of Reynolds-Averaged Navier-Stokes (RANS) CFD codes for each area are increasing, therefore research has been devoted to predictions of ship motion both in maneuvering conditions and in head seas including effects of viscosity. Earlier applications of RANS codes simulate simple geometries advancing in head seas and motions in vertical plane are predicted [4,36]. A detailed analysis of vertical plane motions is found in Weymouth et al. (2005) [46] where different conditions are modeled:

I. the model moves with constant forward speed fixed in the design condition and a regular traveling wave is introduced in the domain (forward speed diffraction problem);
II. the hull is forced to oscillate in the vertical plane with prescribed harmonic motion (radiation problem)
III. an incident wave is introduced and the hull moving with constant speed is free to respond to the resultant forces and moments (predicted motions problem)

Comparison with results obtained from strip theory are presented. Also maneuvering conditions have been modeled and prediction of roll motion for model 5512 of a surface combatant can be found in Wilson et al. (2005) [47].

Herein, the code will be applied and validated for particular working conditions that will include high amplitude heave and pitch motions and resonant conditions, and another relevant aspect that will be analyzed is the interference between both hulls of the catamaran, while previous mentioned works were referred to monohulls.

In addition to the main CFD activity, the Ph.D. program also included the design of a circulating channel, built and tested in the Mechanics Lab. of Dept. of Mechanical Engineering, University of Calabria. As previously mentioned, models are tested in towing tanks of various lengths going from 100m to 250m or more, with ship models having lengths about 3m. Also circulating channels of limited dimensions are used to test models [6,18].

In the specific circumstance, the choice to make the channel, more than the tank, was forced by the limited available areas. The channel was equipped with a PIV measurement system and a model of the DELFT catamaran was tested in

calm water conditions. A more detailed description of channel and test conditions follow in the next chapters.

I.3 Thesis Outline

The present work will include the following chapters:

Chapter One deals with the theoretical background. The components of ship resistance are introduced and the main correlations between ship resistance and ship geometry are presented. An overview on the scaling techniques and the Froude scaling method and its use in prediction of ship resistance, propulsion, seakeeping and maneuvering behavior of hull forms is included.

Chapter Two includes an introduction on the role of CFD in prediction of ship motion and resistance and the evaluation of the state of the art in CFD techniques for ships. The numerical approach used for prediction of motions of the DELFT Catamaran advancing in regular waves is presented.

In *Chapter Three* the definition of modelling conditions and parameters in simulating the seakeeping behavior of the catamaran are included.

Chapter Four presents in detail the numerical simulation results. The main focus is on heave and pitch response, including time histories, transfer functions and phases for heave and pitch, for a range of speeds, wave steepness values and wave frequencies. Comparison with available experimental results allow Verification and Validation study based on three different time steps and three levels of grid refinement.

In *Chapter Five* a description of the circulating channel is introduced and the results of experimental measurements with PIV and the comparison with numerical results are also included.

Chapter 1

Ship Hydrodynamics and the Use of Models in Ship Design

1.1 Introduction

A ship can be considered as a dynamic system composed by the hull, the propeller and the devices to transform the power into effective thrust. The main purpose in ship design is that the ship has to perform at the required speed with the minimum shaft power. This can be achieved by a proper combination hull/propeller. The hydrodynamic efficiency of a ship depends, mainly, on hull shape, on propulsion system and on interaction between them. In fact, in a propelled model, the flow field in the vicinity of the ship stern is affected by the presence of propulsion system itself and ship motions, like sinkage and trim, that are different from the un-propelled case, influence resistance. Similarly, the difference in ship motions affects the flow along the hull and at the inlet of propulsion system and varies the thrust. Traditionally, in ship hydrodynamics, each component of the system is tested separately, then interaction effects are evaluated and finally optimization of the whole system is made so that it can achieve the maximum propulsive efficiency.

To evaluate the hydrodynamic quality of the ship hull, it is common to consider the ship without an integrate propulsion system. In this case the ship resistance, R_T, is defined as the force needed to tow the ship in calm water with constant speed, U_0, on a straight track and the power needed to tow the ship is therefore:

$$P_E = R_T U_0 \tag{1.1}$$

To evaluate the interference effects between hull and propeller, tests are also made in self-propelled models that advance in calm water at constant speed. In this case, the propeller has to develop a force that must equal the resistance met by the ship in its advancing motion.

Therefore, indicating with R_S the ship resistance and with T_P the force developed by propeller, we have :

$$R_S = T_P = R_T + \Delta F \tag{1.2}$$

where ΔF takes into account the interference effects. In this case the power developed by the propeller is:

$$P_P = R_S U_0 \tag{1.3}$$

and the propulsion efficiency of the system is therefore defined as:

$$\eta = \frac{P_E}{P_P} \tag{1.4}$$

The practice to test models in smooth water makes sense because the contractual obligations between shipbuilders and ship owners are based on ship performances in calm water. The ship has to ensure a certain speed with a specified power in good weather or trial, hence in smooth water. The effects of seaway on ship performances are accounted for with a power margin above the power required in smooth water, the allowance depending on the average weather on the sea routes on which the ship is designed to operate. It is obvious that this approach in ship design is based on unrealistic conditions, therefore, from an hydrodynamic point of view, the optimization of hull and propeller is not achieved.

To ensure a good behavior under average service conditions at sea and not only in smooth water, the effects of waves and wind have to be considered too. As a consequence, recent ship research is devoted to improve computing techniques and model testing to predict ship behavior in different and realistic operative conditions, achieving the requirements of maximum performances and maximum efficiency.

In the following paragraphs the different components of ship resistance are discussed and the role of model testing in predicting ship resistance is introduced.

1.2 Ship Resistance

As previously mentioned, the resistance is defined as the force necessary to tow the ship at constant speed on a straight course in calm water. The total resistance is made up of a number of different components which interact in a very complicated way. Therefore, to have a simpler approach these components are generally treated separately [5,19].

In the towed model in calm water the air effects on the superstructure of the ship can be neglected and in absence of eddies caused by appendages, the ship resistance is composed of the viscous resistance (R_V), due to the motion of the hull through a viscous fluid, and the wave making resistance (R_W), due to the energy lost by the ship that creates and maintains a wave system advancing in calm water. Therefore the total resistance is:

$$R_T = R_V + R_W \tag{1.5}$$

The viscous resistance, in turn, is made up of a frictional component (R_f) due to the tangential actions and of a component due to pressure actions (R_P). It is common practice to express the total resistance as the sum of the frictional component and of a residuary component (R_R):

$$R_T = R_f + R_R \tag{1.6}$$

where:

$$R_R = R_P + R_W \tag{1.7}$$

1.2.1 Viscous resistance

The main component of ship resistance is caused by frictional forces on the hull surface (R_f). Experiments have shown that, even for smooth ships, this component amounts to the 80-85 % of total resistance for slow speed ships, while it is close to 50 % for high speed ships. The fluid in contact with the hull surface is carried along with the surface and in proximity of the body moves in the same direction as the ship (Fig.1.1). In the boundary layer, which is thicker going from the bow to the stern, the fluid velocity varies from that of the body at its surface to the undisturbed flow pattern at the outer edge of the body. The body leaves behind it a wake that moves in the same direction of the ship, therefore undisturbed water is enclosed in the wake and represents a continuous energy drain supplied by the hull.

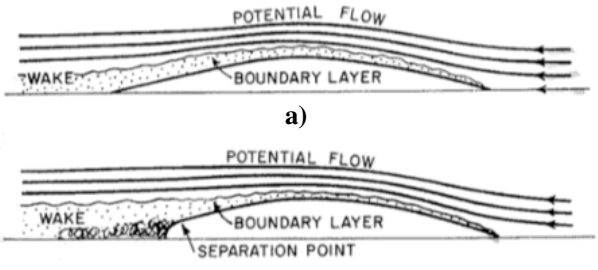

Fig.1.1 Flow around a body advancing at constant speed in a fluid. In a) no separation of the boundary layer occurs, in b) separation is due to the blunt shape of the body at its after end.

To quantify the frictional actions, usually, the wetted surface of the hull is considered as a flat plate where the flow is moving on, at constant speed U_0 as evident if we look at the flow from a reference frame following the ship. In this case, the forward speed of the ship is like an incident flow with velocity U_0 on a stationary hull.

The initial investigations on ship resistance are due to William Froude [8], who separated it in two main components, residuary and frictional resistance. To have a better understanding of frictional actions on ships, he made a lot of experiences on flat plates having lengths varying from $0.61m$ to $15.2m$, in a speed range going from $0.5ms^{-1}$ to $4.1ms^{-1}$ with different values of surface roughness, arriving to the following law for ship resistance:

$$R_f = fAU_0^n \tag{1.8}$$

where f and n are two coefficients that depend on the length and nature of the surface, A is the wetted area and U_0 the flow speed. Although the boundary layer theory was still unknown, this law was consistent with the concepts of laminar and turbulent boundary layers. Based on his experiences, Froude expressed the concept of the *"equivalent plank"* calculating the ship resistance on the hypothesis that it is equivalent to that of a rectangular surface having the same area as the wetted surface of the hull and of length equal to that of the model, moving at the same speed [9]. The validity of the method was clear and since William Froude many experiments and theoretical studies were made on it. In modern skin friction formulations, it is common practice to introduce the friction coefficient (C_f) defined as:

$$C_f = \frac{R_f}{0.5\rho A U_0^2} \tag{1.9}$$

where ρ is the water density, A is the wetted area and U_0 is the ship speed. Different formulations have been proposed for C_f as function of Reynolds number (Re) [19,23,38].

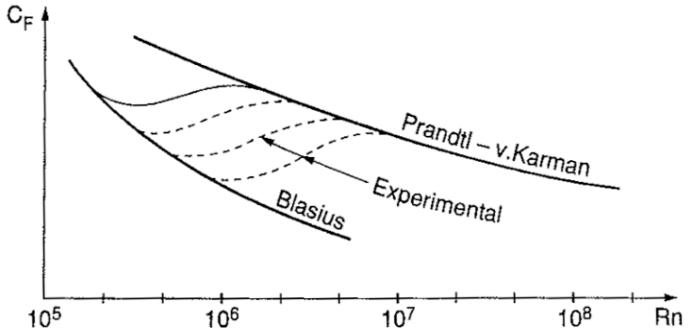

Fig.1.2 Friction coefficient C_f for flow along a flat plate as function of Reynolds number.

From Fig.1.2 it can be observed that at low Reynolds numbers (*Re*), the flow on the plate is laminar and the friction resistance coefficient is described, according to Blasius formulation, as:

$$C_f = \frac{1.328}{\mathrm{Re}^{0.5}} \tag{1.10}$$

When the flow becomes turbulent, for values of Re close to 3.0×10^6, the resistance coefficient increases rapidly above the values calculated according to the Blasius formulation, therefore the law of friction resistance coefficient follows the Prandtl-Von Karman formulation:

$$C_f = \frac{0.072}{\mathrm{Re}^{1/5}} \tag{1.11}$$

The dashed lines in Fig.1.2 indicate the transition from laminar to turbulent flow and begin when the Reynolds number reaches a critical value Re_{Cr}. Beyond this value, as the flow speed *U* increases, the transition happens closer to the leading edge of the plank. Therefore, a bigger share of the plank is interested by turbulent flow, increasing the value of resistance. Many transition lines can be observed and this depends on initial state of turbulence in the fluid, on shape of the leading edge and on characteristics of hull surface. To predict the values of C_f at Reynolds numbers appropriate to a ship only the results for fully turbulent flows can be properly used.

Many formulations for C_f have been proposed (Fig.1.3) in accordance with Prandtl-Von Karman formulation [19]:

$$K/\sqrt{C_f} = \log_{10}(\mathrm{Re}\,C_f) + M \tag{1.12}$$

Schoenherr collected a series of data obtained from many experiments and plotted them as function of Reynolds number. His data were good fit by the formulation given in Eq.(1.12), in which *K=0.242* and *M=0*:

$$0.242/\sqrt{C_f} = \log_{10}(\mathrm{Re}\,C_f) \tag{1.13}$$

This curve, known as *Schoenherr line*, is also called *ATTC line* because it satisfied the requirements of the American Towing Tank Conference that in 1946 began to consider the necessity to adopt standard criteria to calculate the skin friction and to extend the data from model to full scale. This curve, that gives good estimate of C_f for Reynolds numbers higher than 10^7, is not steep enough at the lower Reynolds numbers therefore not appropriate to describe small models.

A further formulation for C_f was given by Hughes and Telfer [19], valid for *Re* as high as 3.0×10^8 that is:

$$C_{f0} = \frac{0.066}{(\log_{10}\mathrm{Re} - 2.03)^2} \tag{1.14}$$

It is a curve of minimum turbulence resistance, valid for the case of a plane smooth surfaces in two-dimensional flow.
Finally, the ITTC (International Towing Tank Conference) in 1957 [13] proposed two possible solutions: one was to use two lines, the *ATTC line* for *Re* higher than 10^7 and a steeper line for lower values. The other was to use a unique line crossing the *ATTC line* at *Re* close to 10^7 and a little steeper throughout. This solution was finally accepted and is still in use, it is called *ITTC '57 line* and has the following expression:

$$C_f = \frac{0.075}{(\log_{10}\mathrm{Re} - 2)^2} \tag{1.15}$$

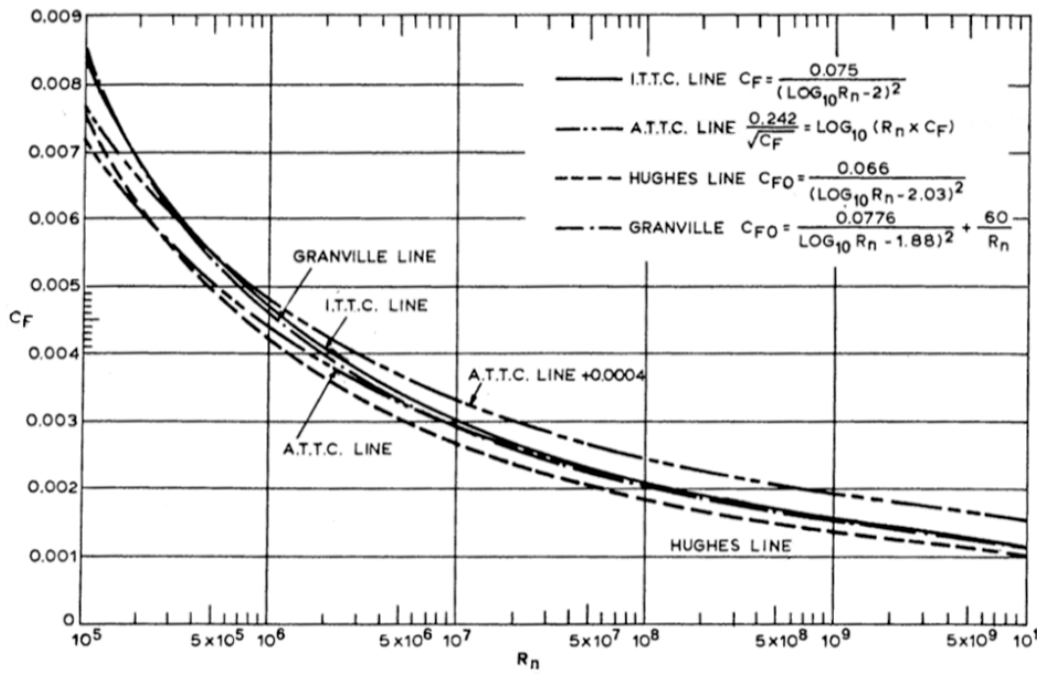

Fig.1.3 Skin friction lines as functions of Reynolds number.

The formulations discussed so far, are valid for a flat plate. However, the effects due to the three-dimensional shape of the hull have to be also considered. In particular, the form resistance is due to the viscous pressure distribution on the hull and to the flow separation, which are three-dimensional

effects (Fig.1.4).

For a better understanding of the effects due to pressure distribution, we can make the following considerations. If we consider a body that moves at constant speed deeply immersed in a non-viscous fluid, there is not any frictional component acting on the hull while the pressure distribution assumes the configuration shown in Fig. 1.4 that can be described by potential flow considerations.

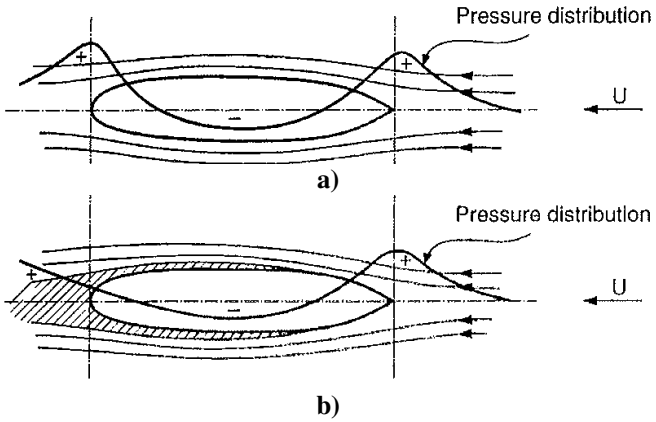

Fig.1.4 Pressure distribution along a ship advancing at constant speed. In a perfect fluid (a) the resulting force on the ship due to pressure distribution is zero and the body experiences no forces. In a real fluid (b) the boundary layers alters the shape of the body and the pressure distribution. A net force acts in the direction opposite to the motion and generates a resistance component.

In particular, the pressure increases above the hydrostatic value near the nose, decreases along the middle of the body and increases again at the stern, while, according to Bernoulli law, velocity has the inverse distribution. As the flow is non-viscous (Fig.1.4.a), the pressure actions are normal to the hull surface in each point and in the forward part of the body they have a total component acting towards the stern therefore resisting the motion. In the after part of the body the total pressure component in the speed direction has opposite direction therefore assists the motion. The resulting force due to both components is zero and therefore the ship does not experience any resistance. This is the well-known D'Alembert paradox [5,19]. On the contrary, in a real fluid, the presence of the boundary layer alters the virtual shape and length of the hull. Therefore the pressure distribution changes (Fig.1.4.b) and the pressure action in the forward part of the ship does not compensate the after component. This originates a net force in the direction opposite to the flow. As a consequence, a resistance component, that is the viscous pressure drag or form drag, is experienced by the hull.

The effects due to flow separation [38], originate another resistance components, whi is the eddy resistance. If the body is blunt, the flow separates from the surface in a specified point of the hull surface and the total pressure in

the after part of the body is reduced therefore the form resistance component is increased.

Both three-dimensional effects are usually taken into account as a component of the residuary resistance (R_R). In the Froude scaling method, that will be discussed later, the residuary resistance that includes also form drag is completely transferred from the model to the ship. An alternative approach to consider the effects of hull form (Fig.1.5) is to introduce a form factor, k, that is defined as:

$$(1+k) = \frac{C_{TM}(\mathrm{Re}_0)}{C_{f0}(\mathrm{Re}_0)} \tag{1.16}$$

This approach is based on the consideration that C_{TM}, the total resistance component of the model, is composed of the the viscous resistance C_{VM} and the wave-making resistance C_{WM}. At low Froude numbers C_{WM} is negligible therefore C_{TM} equals C_{VM}. From Eq.(1.16), it follows that $C_{VM} = (1+k)C_{f0}$ where C_{f0} is the resistance of the equivalent flat plate. Therefore, there is an increase in viscous resistance, and it can be seen in Fig.1.5 where the total resistance curve is parallel to the resistance curve obtained for the flat plate.

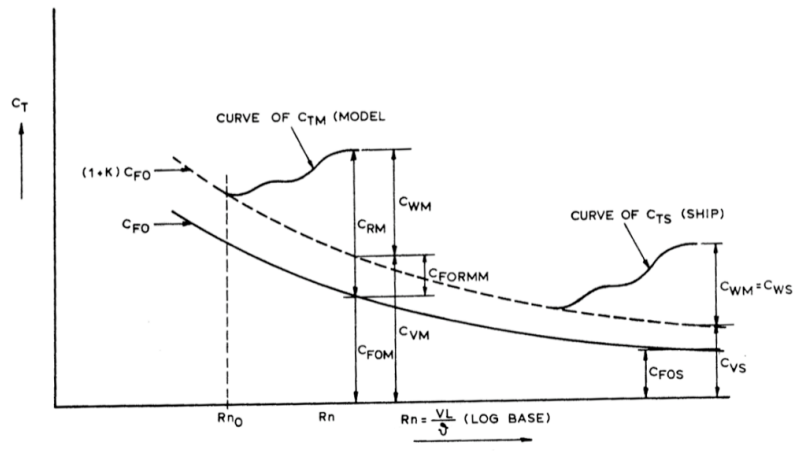

Fig. 1.5 Effects of the form factor k on ship resistance and extrapolation of ship resistance from model (M) to full scale (S). C_{f0} is the resistance coefficient of the equivalent flat plate as function of Reynolds number, $(1+k)C_{f0}$ takes into account the resistance due to the 3D shape of the hull and the difference between both components is called C_{FORM} that is referred to the form of the hull. C_{FORM} and C_{f0} give the total viscous component (C_V). C_W is the wave making resistance. C_T is the total resistance given by wave-making and viscous components. The curves at low Reynolds numbers are relative to model resistance (M), for higher Reynolds numbers the C_T is extended to ships (S).

The form factor k is usually determined empirically, as no satisfactory method to derive appropriate values for k has still been found[19].

1.2.2 Wave-making resistance

The wave-making resistance R_W is caused by the waves that the vessel creates when it follows a straight course at constant speed U. This resistance arises from the pressure distribution on the hull surface in proximity of a free surface and it is also present in the absence of fluid viscosity. As previously seen, if we consider the pressure actions on a deep submerged body in a perfect fluid, the total resistance component is zero. However, if we consider the same body in proximity of the free surface, the pressure distribution creates a surface elevation that gives origin to a characteristic wave system. Therefore, the pressure distribution is modified and a net force acting in the opposite direction to ship motion is generated. This force is called wave-making resistance. Initially, at the bow, where pressure increases, the free surface elevates and causes the bow wave. Downstream, along the body of the hull, where pressure decreases, the surface level decreases too, creating a through that can be seen on the hull. Finally at the stern, the pressure increases again and a wave crest is generated which is lower that the bow wave crest. This behavior follows from Bernoulli theorem.

For the wave-making resistance there is no simple formulation as for frictional resistance, and much of knowledge is due to experiences and model tests [19,23] .

A typical wave pattern is depicted in the following figure (Fig.1.6):

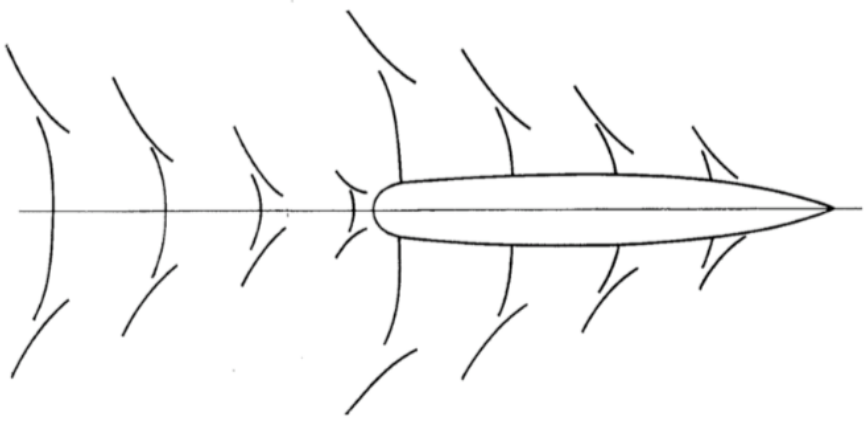

Fig. 1.6 Schematic diagram of bow and stern wave systems. The lines are referred to wave crests. Two wave systems are prominent: diverging waves radiating from the hull sides, and transverse waves normal to the direction of motion.

This wave pattern is very similar to the one obtained by Lord Kelvin (Fig. 1.7) that observed and described the phenomenon of ship waves generation, considering the simplest case of a point advancing on a straight line over the water surface.

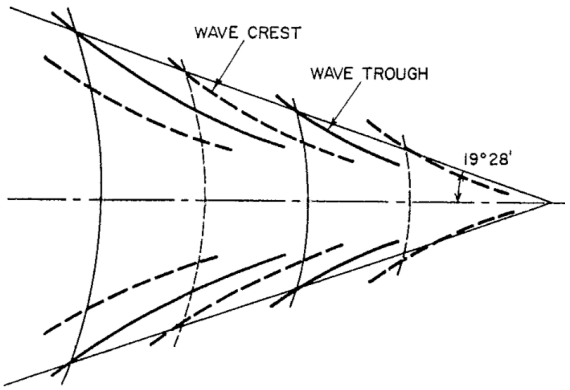

Fig. 1.7 Kelvin wave pattern. Wave system generated by a point advancing at constant speed on a straight line over the water surface. The whole wave pattern formed by diverging and transverse waves is contained in two straight lines starting from the point and forming an angle of 19° 28' with the direction of motion. The angle is constant in deep water but is larger in shallow water.

A typical wave system can be observed that is characterized by transverse and diverging waves which develop behind the point. The whole pattern is contained within two straight lines starting from the point and making an angle of 19° 38' with the direction of the point motion. The transverse waves are curved back at a certain distance from the centerline and meet the diverging waves in cusps where the height increases. This height decreases more slowly than the transverse waves height therefore at a long distance from the point, the diverging waves are usually prominent.

How can be seen in Fig.1.6 this wave system is very similar in the case of ships. In particular, ships generate different wave systems. The most prominent is the one created by the bow, but other wave systems are created in correspondence of shoulders and at the stern. The individual wave systems are not always easily distinguishable because of their mutual interactions that have a relevant effect on wave-making resistance.

The evaluation of wave height, H_W, is fundamental for wave resistance because the higher the waves, the higher the energy to maintain the wave system and therefore the higher the resistance. This is strictly related to ship speed. In fact, the energy loss, E_W, in maintaining the wave system is characterized by:

$$E_W \propto \lambda b H_W^{\,2} \tag{1.17}$$

where λ is the wavelength and b is the wave width. On the other hand, wave height is proportional to the square ship speed:

$$H_W \propto U_0^{\,2} \tag{1.18}$$

and from Eq.(1.18) the following dependence is derived for wave-making resistance, R_W:

$$R_W \propto U_0^{\,6} \tag{1.19}$$

As a consequence, the wave-making resistance coefficient varies as U_0^4. This dependence is emphasized in the total resistance diagrams where the ship resistance is plotted as function of the Froude number. It is a non dimensional parameter that takes into account the wave elevation and is defined as:

$$Fn = \frac{U_0}{\sqrt{gL}} \tag{1.20}$$

where L is a characteristic ship length and g is the gravity acceleration.

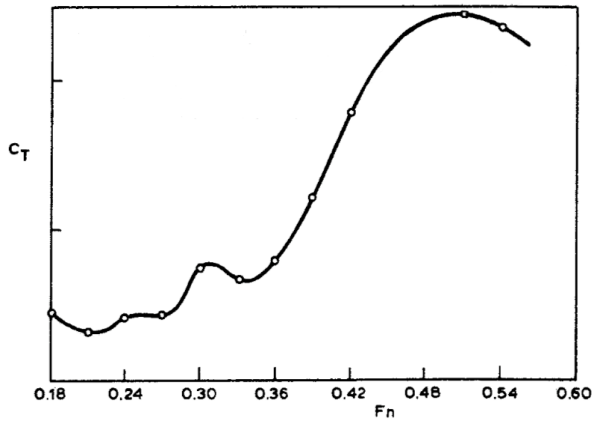

Fig. 1.8 Typical resistance curve as function of Froude number. For low speeds (low Fn) only the viscous effects are relevant and the curve follows the curve of C_f . As speed increases, wave-making resistance becomes the most relevant component and it increases as U^4. Humps and hollows are due to interference effects between the different wave systems.

If we look at a typical diagram of resistance coefficient for a ship as function of Froude number (Fig.1.8), it can be observed that at low speeds the waves generated by the ship, are very small and the viscous resistance is dominant therefore the diagram follows the shape of C_f as previously seen. For higher Froude numbers(i.e. higher speeds) the most dominant component of resistance is due to the wave generation, therefore the most part of the curve represents the wave-making resistance. It can be observed that this component of resistance grows as speed increases and it presents some hollows and humps, caused by the interference effects of the wave systems generated by the hull. For instance, if we consider only the interference between the bow and the stern wave systems, as the ship speed increases, the wave pattern changes according to the following expression for wavelength:

$$L_W = 2\pi U^2 / g \tag{1.21}$$

Furthermore, as the wavelength changes, also the relative positions of the crests and the troughs of both wave systems change. In particular there are some speed values, in correspondence of which the crests of both systems reinforce each other, and a higher resulting wave produces an increase in resistance. On the contrary, there are other speed values which determine the cancellation of crests and the through of both systems, creating, thus, a lower energy dissipation.

The above considerations on interference effects between wave systems, can be well explained in the following example (Fig.1.9), that shows the results of an experience made by Wigley to investigate this phenomenon[19]. He showed that the final wave profile was made up of five components: a symmetrical disturbance of the free surface, the bow wave system beginning with a crest, the forward shoulder system, the after shoulder system and the stern system. This simple wedge-shaped body illustrates the mechanism of wave interference and its influence on wave resistance. As the wavelengths change with ship speed while primary crests and troughs originate at fixed points (bow, stern and shoulders), the shape of the total wave profile is continuously changing. This creates the effects of superposition or cancellation of the crest and troughs of the different wave systems.

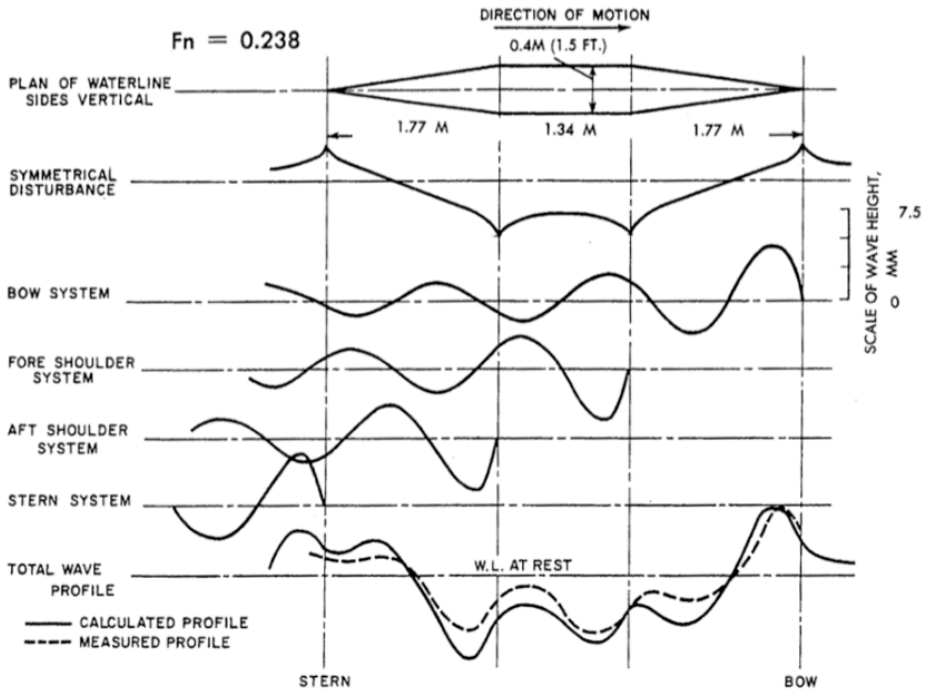

Fig. 1.9 Wave system for a simple wedge-shaped form and interference effects. Five wave systems are generated in correspondence of the bow, stern and shoulders. The points where waves generate are fixed, while variations in the ship speed cause changes in wavelengths. The wave profile generated by combining all the wave systems is changing too and the superposition or cancellation of the crests and troughs of the different wave systems create the humps and hollows in the resistance curve.

1.3 Model testing of ship resistance

The ship resistance is predicted by model testing. This procedure consists in testing a model geometrically similar to the ship and scaling the results from model scale to full scale[5,19,23]. This principle of extrapolation from model to ship is still in use in all towing tanks and the procedure is well illustrated in Fig(1.10).

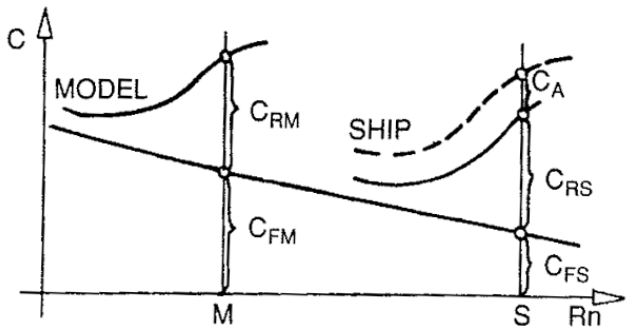

Fig. 1.10 Scaling of ship resistance from model, M, to ship, S. Test is conducted on the model for a specified Froude number and C_{TM} is measured, C_{FM} is then calculated according to the ITTC '57 line and C_{RM} is calculated with Eq.(1.33). Under Froude similarity conditions C_{RM}=C_{RS}, C_{FS} is calculated form the ITTC '57 correlation for the Reynolds number relative to the ship and C_{TS} is then calculated using Eq.(1.34).

By using the dimensional analysis, it has been observed that ship resistance depends on two non-dimensional groups, the Reynolds number, that takes into account the viscous actions, and Froude number, that controls the surface wave system. Therefore:

$$C_T = \frac{R_T}{0.5\rho A U_0^{\,2}} = f\left(\frac{U_0 L}{\nu}; \frac{gL}{U_0^{\,2}}\right) \tag{1.22}$$

where L is the ship length and A is the wetted area of the hull. Eq.(1.22) states that two geometrically similar ships of different size experience the same C_T if the flow conditions for both, satisfy the same *Re* and *Fn*. If we consider a non-viscous flow, the influence of Reynolds number can be neglected and the only parameter that affects ship resistance is *Fn*. Therefore the residuary resistance can be written as:

$$C_R = \frac{R_R}{0.5\rho A U_0^{\,2}} = f\left(\frac{gL}{U_0^{\,2}}\right) \tag{1.23}$$

As a consequence, if the ship and the model have the same Froude number, *Fn*, then $C_{R,S}$=$C_{R,M}$.

If we denote with the subscripts S and M the ship and the model respectively, the following expressions hold:

$$\frac{R_{R,S}}{R_{R,M}} = \frac{(0.5\rho A U_0^{\,2})_S C_{R,S}}{(0.5\rho A U_0^{\,2})_M C_{R,M}} \tag{1.24}$$

$$\frac{U_{0S}^{\,2}}{gL_S} = \frac{U_{0M}^{\,2}}{gL_M} \tag{1.25}$$

and since $C_{R,S}$=$C_{R,M}$, substituting in Eq.(1.24):

$$\frac{R_{R,S}}{R_{R,M}} = \frac{A_S U_{0S}^{\,2}}{A_M U_{0M}^{\,2}} = \frac{(L_S)^2 L_S}{(L_M)^2 L_M} = \frac{L_S^3}{L_M^3} = \frac{\Delta_S}{\Delta_M} \tag{1.26}$$

where Δ_S and Δ_M are the immersed volumes of the ship and the model respectively.

This equation is known as Froude's *"Law of Comparisons"* according to which *"The residuary resistance of geometrically similar ships is in the ratio of the cube of their linear dimensions if their speeds are in the ratio of the square roots of their linear dimensions".*

In fact, if we indicate with λ the ship to model linear dimensions ratio:

$$\frac{L_S}{L_M} = \lambda \tag{1.27}$$

then, for Eq.(1.25):

$$\frac{U_{0S}}{U_{0M}} = \frac{(L_S)^{1/2}}{(L_M)^{1/2}} = \lambda^{1/2} \tag{1.28}$$

and:

$$\frac{R_S}{R_M} = \frac{(L_S)^3}{(L_M)^3} = \lambda^3 \tag{1.29}$$

It can be observed that if, for example, we consider a ship having dimensions L=100m and a model of 5 m (λ=20) the model speed corresponding to 20ms^{-1} for the ship is $U_M = \frac{U_S}{\sqrt{20}} = 4.47$ ms^{-1} which is a

convenient test condition because we can test models with limited dimensions at speed that are easily attainable in a basin.

If we consider a deep submerged body, where there is no surface effects but only viscous effects are relevant, only the Reynolds number has influence in Eq.(1.22):

$$C_f = \frac{R_f}{0.5\rho S U_0^{\,2}} = f\left(\frac{U_0 L}{\nu}\right) \tag{1.30}$$

Therefore, two geometrically similar ships, under deep submerged conditions, have the same resistance coefficient if they have the same Reynolds number. If both model and ship advance in water with the same density and temperature, ν has the same value, hence:

$$U_{0S} L_S = U_{0M} L_M \tag{1.31}$$

If we consider again the same example of a 100*m* long ship advancing at $20ms^{-1}$, a 5*m* long model would require a speed of $400ms^{-1}$, that is quite different from the value of $4.47ms^{-1}$ obtained according to similarity based on Froude number. Therefore the total resistance similitude cannot be obtained on both Reynolds and Froude numbers, except in the case of $\lambda=1$ that is the model has the same dimension of the ship.

The Froude method allows the problem solution based on the separation of the total resistance in two components and assuming that C_f is function of Reynolds number only, while C_R is function of Froude number only:

$$C_T = C_R + C_f \approx f_1\left(\frac{U_0^{\,2}}{gL}\right) + f_2\left(\frac{U_0 L}{\nu}\right) \tag{1.32}$$

Tests, therefore, are conducted according to the Froude similarity The method states that tests are carried out on models which are in linear dimensions ratio λ with the ship and at a speed ratio given by Eq.(1.28). The total resistance, $R_{T,M}$, is measured while frictional resistance, $R_{f,M}$ is estimated by the equivalent plank frictional formulations, (§1.2.1) computed for the model Reynolds number. Then $C_{R,M}$ is calculated subtracting from the total resistance the frictional resistance (Eq.1.32).

According to Froude similarity, $C_{R,S}$=$C_{R,M}$., so that:

$$C_{R,M} = C_{T,M} - C_{f,M} = C_{R,S} \tag{1.33}$$

Similarly to the model case, the ship frictional resistance can be estimated at the ship Reynolds number, from the equivalent plank frictional formulation.

Therefore the total resistance for the ship will be calculated as the sum of residuary resistance and frictional resistance.

$$C_{T,S} = C_{R,S} + C_{f,S} \tag{1.34}$$

Some considerations are necessary.

I. In using the *ITTC'57 line* to extrapolate the frictional resistance coefficient, the assumption is made that the flow along the hull model has to be turbulent. The correlation is in fact valid for turbulent flows as previously noted. As the model is usually small, the turbulent flow has to develop as close as possible to the bow, therefore, usually, in model testing some turbulence stimulators are used at the bow of the model.

II. In Fig.(1.10) an allowance C_A is introduced to take into account the hull roughness, air resistance and appendage resistance. Model tests, in fact are made on bare hulls (i.e. without appendages) for scaling problems and are based on smooth models so that the roughness effects are not considered. Air resistance effects can be usually neglected because:

$$R_A = 0.5\rho_A C_D A_{SS} U_0^{\ 2} \tag{1.35}$$

where A_{SS} is the area of the superstructure projected in the transverse plane of the vessel, ρ_A is air density that is only 1.25Kgm^{-3} whereas water density is 1027 Kgm^{-3}, and the drag coefficient C_D assumes values between 0.5 and 0.7.

1.4 Effects of ship geometry on resistance

The main geometrical properties of ships and their effects on ship resistance will be discussed.

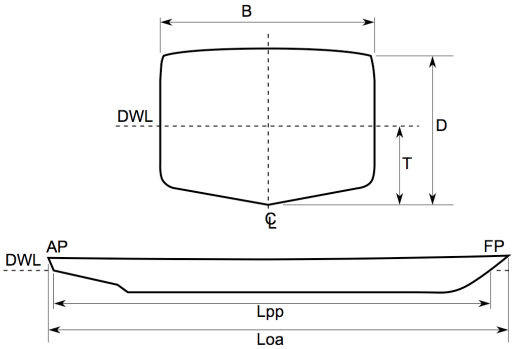

Fig.1.11 Ship geometry. AP: After perpendicular; B: beam; D: Depth; DWL: Design Water Line; FP: Fore Perpendicular; L_{OA}: Length Overall; L_{PP}: Length between perpendiculars; T: draft.

The block coefficient (C_B) is defined as:

$$C_B = \frac{\nabla}{L_{PP} B D} \tag{1.36}$$

where ∇ is the ship displacement, that is the displaced volume of water, L_{PP} is the length between fore perpendicular (FP) and the aft perpendicular (AP), B is the beam and D is the draft. The fore perpendicular is a vertical line through the intersection of the waterline and the fore side of the hull, while the aft perpendicular is the vertical line through the intersection of waterline and the stern of the hull.

Molland et al.(1996)[22], made a systematic study on the influence of geometry on calm water ship resistance, sinkage and trim, and results showed that the most significant parameter that affects ship resistance is the displacement ratio $L/\nabla^{1/3}$. As this ratio increases, the resistance decreases, while the effects of beam to draft ratio B/D are not relevant.

In the following figure (Fig.1.12), the residual resistance coefficient (C_R) is plotted as a function of Froude number for a monohull and for a catamaran. For the catamaran case, the C_R is plotted for different values of the parameter (2p/L) that is referred to the distance between demihulls

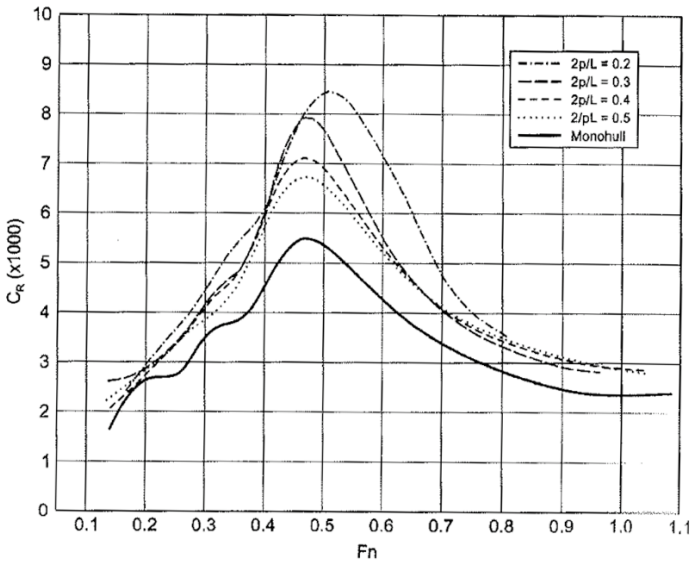

Fig. 1.12 Residual resistance for monohulls and catamarans as a function of Froude number, Fn. Residual resistance is defined as the total resistance with exclusion of frictional resistance. The effects of hulls interaction are plotted as function of the parameter 2p/L with p the distance between demihulls and L the ship length.

The curve has a shape typical of semi-displacement vessels. It can be seen that the resistance of catamarans is higher than the monohulls but it approaches the C_R of monohulls as the distance 2p/L increases.

In the following figure (Fig.1.13) the different components of total resistance are plotted. It can be seen that viscous and wave-making components are of equal importance. However at the lower and the higher Froude numbers, viscous resistance dominates. In fact, for low values of *Fn*, the main component is the frictional resistance represented by the dashed line that takes into account the form factor, *k*. As *Fn* increases the residuary resistance increases while the frictional component is reduced. Finally, at the higher Froude numbers the viscous effects become relevant again, while the contribute of residuary resistance to total resistance is reduced.

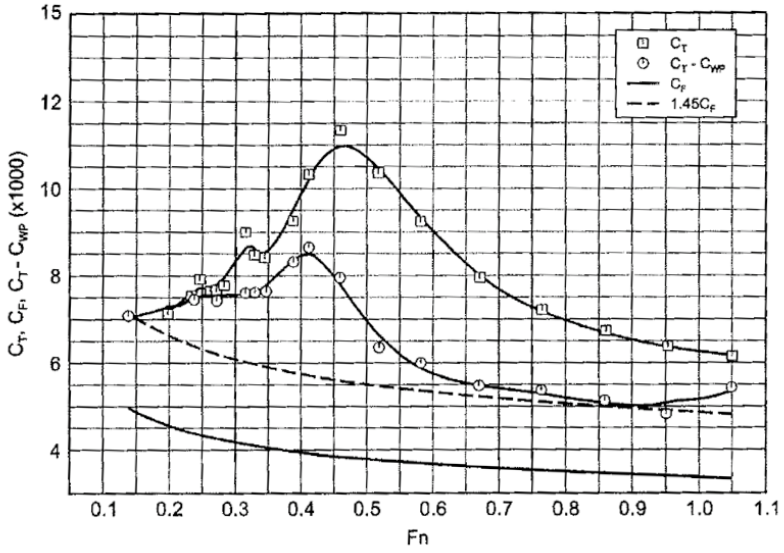

Fig. 1.13 Resistance components as a function of Froude number Fn. C_T is the total resistance, C_F is the frictional component and C_T-C_{WP} the residual component. 1.45C_F takes into account the form factor k. For the lowest and highest Fn the viscous effects are more relevant.

In Fig.1.14 typical curves of trim angle and sinkage are plotted as functions of Froude number and they are strictly related to the ship resistance. In fact, a ship advancing in calm water is subjected to motions due to the hydrostatic and hydrodynamic actions of the wave system. Buoyancy of the ship is due to the hydrostatic actions that are dominant for low speeds. For higher speeds, the hydrodynamic actions due to the generation of the wave system, cause a variation in pressure distribution on the hull surface respect to the static condition. Therefore, the ship moves towards a new equilibrium condition. Sinkage corresponds to the motion of the center of gravity of the ship in the vertical direction, trim is the rotation angle generated by the difference in pressure distribution between the bow and the stern. Positive trim means bow up, while sink is positive when the ship moves downward. It can be seen (Fig.1.14a,b) that trim angle and sinkage increase rapidly for *Fn* higher than 0.3-0.4 in correspondence of which their effects on ship resistance are relevant.

The resistance curves and the corresponding ship motions will be derived for the DELFT Catamaran and the correlation between them will be better investigated in the next chapters.

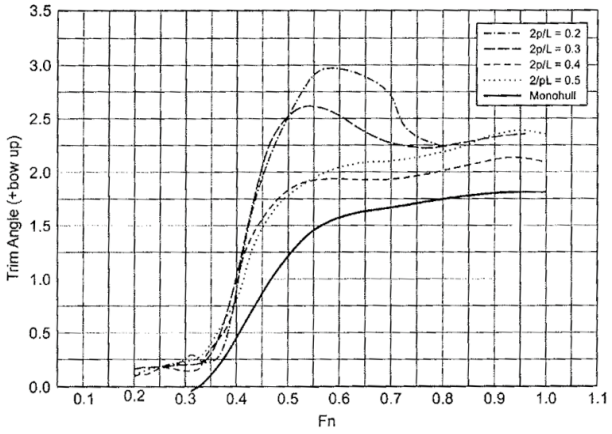

a)

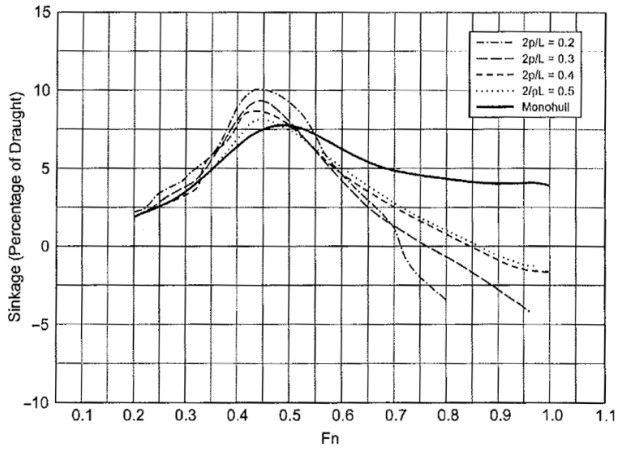

b)

Fig.1.14 a) Trim as a function of Froude number **b)**Sinkage as a function of Froude number. The effects of hull interaction are included with the parameter 2p/L. The highest values of ship motions are registered for Fn highest than 0.45 where the peak of resistance is observed.

Chapter 2

The Role of CFD in Ship Hydrodynamics and Use of the URANS Code CFDSHIP-Iowa

2.1 Introduction

Much of the understanding in ship hydrodynamics is related to model testing. Usually a parent model is created and series of tests are conducted with systematic variations in the hull form to obtain optimization of the hull shape. This practice, consisting on repeated building and testing on models of candidate designs, is quite expensive and time consuming. With the coming and increasing development of computer technology, CFD codes predicting ship behavior were developed and nowadays offer a valid support to ship design. The CFD technology is not enough mature to become an alternative to the traditional build & test technique. However, increasing predictive capabilities of Reynolds-Averaged Navier-Stokes CFD codes, are going to revolution the design process and, combined with optimization tools, are leading to the simulation based design (SBD). This purpose can be achieved only by a combination of CFD and model testing. Experimental techniques, therefore, are evolving to provide more accurate data that are used as benchmark for verification and validation of CFD codes. This led to various high quality experiments that have been performed in the last decade.

The most advanced techniques use optical measurement instruments. Laser Doppler Velocimetry (LDV) provided a deep insight into complex flow fields, allowing the measurement of velocity vector at prescribed points of complex flow field with high accuracy and information on the mean and fluctuating velocity is obtained. LDV has some limitations. In fact, it is a single point measurement technique and requires long periods of operation to get a whole velocity field. Besides, it is difficult to reconstruct the spatial characteristics of large structures found in complex flows. Recently, another laser technique that found wide application in naval field is the Particle Image Velocimetry (PIV). This technique overcomes the limits related to the single-point techniques and

allows whole field measurements and a reduction of testing time.

Usually, specific cases are tested by the ship community and experimental data are available. As example, in the 1990 CFD Workshop on ship viscous flows [30], the HSVA tanker was considered as test case and boundary layer and LDV data were taken in a wind tunnel on this hull form at various axial locations. In the 1994 CFD Workshop [31], data for Series 60 were used for codes validation. Data included resistance, wave profiles, surface pressures, and mean velocity. In the Workshop held in Gothenburg in 2000 [17] the KVLCC2 tanker, and the KCS Container Ship were tested. The KVLCC2 had a bulb at the bow and at the stern and the important feature to focus on, was the strong bilge vortex with a distinctive hook pattern of the axial velocity component at the propeller plane. For the KCS, data on resistance, wave profiles, mean flow and surface pressure were made available. Another tested model was the bare hull of the DTMB 5415. The data-set for this model included: resistance, sinkage and trim, wave profile, near and far field wave elevation, mean flow and turbulence data obtained with LDV.
In resistance and propulsion fields, a wide variety of experimental data for CFD validation exist and to estimate the quality of the experimental results, a standard procedure for uncertainty assessment has been developed by AIAA (American Institute of Aeronautics and Astronautics) and recommended by 1999 ITTC (International Towing Tank Conference). On the contrary, very little Experimental Fluid Dynamics (EFD) data exist that can be used as benchmark data for CFD validation of seakeeping codes. Besides, most data-sets lack specific information for replication of experimental tests or for the proper set-up of seakeeping simulations. Most of the data available are referred to model S-175 ITTC (O'Dea [25], Fonseca and Soares [7]) for different steepnesses and wavelengths of the incoming waves, but final uncertainties are not presented. Guy et al. [12] tested the DTMB 5512 focusing on the forward speed diffraction problem, that is, a motionless ship in regular waves. Stern et al.(2007) presented a detailed EFD data set for the DTMB 5512 in which particular regard was given to test design and operating parameters in order to define the initial conditions for the heave and pitch boundary value problem. A detailed uncertainty assessment according to the most recent standards of the 24th ITTC seakeeping report [14] was also included.

2.2 State of the art

The early attempts in predicting ship flows by Computational Fluid Dynamics were based upon potential flow methods. In conjunction with proper boundary conditions to model the free surface, these methods were able to predict quite well the wave resistance and have been important tools in the solution of seakeeping problems. Much research in defining a proper boundary condition for free surface is due to work made by Raven [33] and Janson [16].

These methods were enough mature to be a valid tool in ship design and are still used to predict the wave- making resistance (*Panel methods*) or in the design of propellers (*Boundary Elements Methods*) for their robustness and low time of calculation. However the application of these methods is quite limited. As example, for surface ships, where viscous resistance is the dominant component of resistance, the potential flow methods fail. Therefore, viscous based calculation methods are needed for prediction of the flow in the thin boundary layer around the hull and in the wake region.

In a Workshop held in Gothenburgh in 1980, different viscous based methods were applied to the HSVA tanker and, even though they gave good results in prediction of the boundary layer along the hull shape, they failed completely in the wake region and were not able to predict the bilge vortex at the stern. Therefore, this led to the idea of using more rigorous approaches based on Reynolds-Average Navier-Stokes (RANS) equations. The early applications of RANS methods have been devoted to the problem of steady resistance and propulsion for their relative simplicity. Results were presented in a second workshop held in 1990 [30], where improvements in the prediction of the flow field at the stern of the HSVA tanker were showed but no methods for modeling the free surface were introduced. In the 1994 Workshop in Tokyo [31], the bilge vortex on the HSVA was predicted quite well using non-isotropic turbulence models and another test case, the Series 60, was used to demonstrate that also the free surface could be predicted with RANS. In particular, the free surface was well predicted near the hull but accuracy deteriorated away from it.

Recently, a high accuracy in resistance predictions has been demonstrated in the results presented in the Gothenburgh 2000 Workshop on CFD in Ship Hydrodynamics [17]. On the contrary, the application of RANS methods to seakeeping and maneuvering is less mature, due to the complexity of simulating unsteady flows. Typical solution techniques were based on the assumptions of small amplitude motions and potential flows. Moreover, the fully non-linear governing equations of ship motions were simplified in two sets of uncoupled linear differential equations, one for vertical plane motions and one for horizontal plane motions. Predictions of ship motions in the vertical plane were more accurate than for horizontal plane, but solutions for heave and pitch also failed when the conditions for linear assumptions were no more valid as for high steep waves. Thus, recently, much effort has been done to apply and extend the use of RANS methods in seakeeping and maneuvering problems, since effects due to viscosity, vorticity creation in the boundary layer, vortex shedding, and turbulence are naturally included. Hence, RANS codes have been applied to different test cases for the first time in the 2005 Workshop in Tokyo [32]. Simulations for predicted and prescribed roll motion for the surface combatant DTMB 5512, using RANS codes, have been performed by Wilson et al. [47] with the inclusion of the verification and validation study to quantify numerical and modeling errors. A detailed analysis

of vertical plane motions, by the use of a RANS code, is found in Weymouth et al.[46], where the forward-speed diffraction problem, forward radiation and predicted motion response for the modified Wigley hull in regular head seas have been modeled, and comparison with results from strip theory has been presented.

However, in the mentioned works the motions were limited to small amplitudes mainly for the limitations present in the technique used to model the free surface. In fact, a surface-tracking method has been used and with this approach, an excessive grid deformation can make the numerical method to fail. Carrica et al. [2], presented unsteady RANS simulations of the ship forward speed diffraction problem for the DTMB 5512, for which detailed experimental data are available, and a different approach in modeling free surface was introduced.

2.3 Reynolds Average Navier-Stokes Equations

In Computational Fluid Dynamics, the direct solution of the exact Navier-Stokes equations is very expensive in terms of computational resources, especially for high Reynolds-number turbulent flows in complex geometries as ships flows. To overcome this difficulty, different alternative approaches are used and the most commonly adopted in practical applications is the time averaging of the Navier-Stokes equations (RANS). The time averaging of mass and momentum equations allows the solution of the mean flow variables. Therefore the small scales of turbulent fluctuations are not solved directly but are properly modeled introducing the turbulence models.

In RANS method, the variables of interest are decomposed into the mean and fluctuating components. As example, velocity vector can be expressed as:

$$U_i = u_i + u'_i \tag{2.1}$$

where u_i is the mean velocity component and u'_i is the fluctuating one $(i = 1,2,3)$. Similarly, for pressure and for a generic scalar quantity Φ, the following expression can be used:

$$\Phi = \varphi + \varphi' \tag{2.2}$$

The RANS equations are then obtained by substituting expressions (2.1) and (2.2) in the instantaneous mass and momentum equations and by computing time average.

With this approach the equations are expressed as follows:

$$\frac{\partial \rho}{\partial t} + \frac{\partial (\rho u_i)}{\partial x_i} = 0 \tag{2.3}$$

$$\frac{\partial (\rho u_i)}{\partial t} + \frac{\partial}{\partial x_j}(\rho u_i u_j) = -\frac{\partial p}{\partial x_i} + \frac{\partial}{\partial x_j}\left[\mu\left(\frac{\partial u_i}{\partial x_j} + \frac{\partial u_j}{\partial x_i} - \frac{2}{3}\delta_{ij}\frac{\partial u_l}{\partial x_l}\right)\right] + \frac{\partial}{\partial x_j}\left(-\rho\overline{u'_i u'_j}\right) \tag{2.4}$$

Eq.(2.3) and Eq.(2.4) have the same form as the instantaneous Navier-Stokes equations, but in this case, velocities and other solution variables correspond to time averaged values. The turbulence effects are included in the additional term $-\rho\overline{u'_i u'_j}$ that represents the Reynolds stresses and must be modeled with the inclusion of other equations for problem closure.

Different turbulence models have been proposed, based on Boussinesq hypothesis to relate the Reynolds stresses to the mean velocity gradients according to the following formulation:

$$-\rho\overline{u'_i u'_j} = \mu_t\left(\frac{\partial u_i}{\partial x_j} + \frac{\partial u_j}{\partial x_i}\right) - \frac{2}{3}\left(\rho k + \mu_t \frac{\partial u_i}{\partial x_i}\right)\delta_{ij} \tag{2.5}$$

where μ_t is the turbulent viscosity and k is the turbulent kinetic energy. The Spalart-Allmaras model, as example, needs only one extra transport equation for turbulent viscosity, while the k-ε and k-ω models need two extra transport equations where μ_t is calculated as function respectively of k and ε or k and ω.

In ship hydrodynamics, different turbulence models have been tested. For a decade, the most used model has been the algebraic model of Baldwin-Lomax, that gave as good results as more sophisticated methods with the advantage of an easier implementation. However, as the model could not predict the flow physics associated with complex non-isotropic flows, present trend is devoted to use two-equation models as the k-ε model in all its different forms and also the k-ω or the Spalart-Allmaras one-equation model. These methods are adequate to predict boundary layer flows, but for more complex flows with secondary separation they may be unsatisfactory. This has been shown in the Workshop on CFD held in Gothenburgh (2000)[17] in which the focus was on the strong bilge vortex characterized by a distinctive hook shape generated at the propeller plane of the KVLCC2 model. In this case the best results were given by the Reynolds Stress Model even though none of the turbulence models could capture the hook shape. It is difficult to draw conclusions on what is the best method. What arises from literature is that simper zero, one and two-equation models seem to predict much of the flow field with high accuracy, as in the case of boundary layer. For more sophisticated flows, however, higher-order non-linear models seem to be necessary.

To properly solve the equations of motion, boundary conditions are needed.

On the ship hull, for viscous flows, a no-slip condition is applied. Another physical boundary, typical of ship flows, is the free surface. Different techniques have been introduced to model the free surface and difficulties arise due to the fact that it is an interface between two phases and that it is a moving surface.

Surface-tracking methods have been widely used in predicting the free surface. In practice, the free surface is considered as a material boundary and a dynamic boundary condition is applied at the water surface for the Navier-Stokes equations. The difficulties in using this approach derive from the fact that, as the free surface is a boundary of the solution domain, a grid has to be created on the free surface. Therefore, once the free surface starts to change, the grid must be adjusted to accommodate the new free surface. If the distortions of the free surface become too large, the grid is too highly skewed for a stable running of the RANS code. These limitations restrict the use of surface tracking methods to small amplitude motions. This method has been applied to free surface ship flows including steady resistance computations, forward speed diffraction, roll decay, heaving and pitching motions in head seas. In each case, when the surface grid is too deformed, the computation breaks down. One of the main conclusions of the Gothenburgh Workshop (2000), was that further research should be devoted to surface-capturing methods to overcome the limitations of the surface-tracking methods.

Surface-capturing techniques do not suffer the limitations of the surface tracking methods, discussed so far, because the free surface is treated as an iso-surface of a three-dimensional function which can take any arbitrary shape. Surface capturing methods include the level-set method, the density function method and the VOF method. Many studies have been conducted using surface capturing methods: Sato et al. [36] analyzed the Wigley hull and the Series 60, Orihara and Miyata [26] computed heave and pitch motions for a container ship in head waves with very promising results, Carrica et al. [1] applied a level-set method to a surface combatant and large amplitude motions were also predicted. In this work the single-phase level-set method will be analyzed as implemented in the code CFDShip-Iowa.

2.4 CFDShip-IOWA

The RANS code used in the present work is *CFDShip-Iowa*, that has been developed over the past 20 years under *ONR* (Office of Naval Research) support at *IIHR* (Iowa Institute of Hydraulic Research), Iowa, USA [27]. Originally designed to support both thesis and project research, it has been successfully transitioned to US Navy, University laboratories and industries. It is a general-purpose, multi-block, parallel-computing code developed for ship hydrodynamics. It is intended for steady and unsteady resistance and propulsion simulations, including free surface modeling, and allows prediction

of body motions enabling seakeeping and maneuvering simulations. The code solves the unsteady Reynolds-Averaged Navier-Stokes equations (RANS) in a absolute inertial earth-fixed reference frame *(X,Y,Z)* for an arbitrary moving but non-deforming control volume and solution domain (Fig.2.1). By using this approach, implementation of boundary conditions is simpler compared to solving the momentum equations in a ship-fixed non-inertial reference frame and saves computational cost by reducing the solution domain size. By integrating the elemental forces, the forces and moments acting on the ship are calculated and projected in a non-inertial ship-fixed reference frame *(x,y,z)* with its origin *o* fixed in the center of gravity of the ship (Fig.2.1). By the application of the rigid body equations, the translational and angular velocities of the ship are computed using a predictor/corrector approach (6DOF module). Velocities are then transformed back in the absolute earth-fixed coordinates and integrated respect to time, giving, therefore, the new positions and grid velocities. The free surface is captured using a single-phase level-set method and turbulence is modeled by a blended k-ε/k-ω model without wall functions. The equations are discretized using a finite-difference approach. For convective terms and diffusion terms, second-order upwind schemes and second-order central differences are used, respectively. A PISO algorithm is used to enforce mass conservation, resulting in a Poisson equation for pressure. The equations are non-dimensionalized with ship speed U_0, water density ρ, viscosity μ and ship length L_0 and then transformed in non-orthogonal curvilinear coordinates (ε,η,ζ).

CFDShip-Iowa allows overset multiblock grids and in particular the SUGGAR code (Noack 2005) is used to obtain the overset domain connectivity between the set of overlapping grids. Finally, an MPI-based decomposition approach is used, where each decomposed block is mapped to one processor.

In the present paragraph, the mathematical model will be described in more detail and the numerical technique and solution strategy will be illustrated.

2.4.1 Governing differential equations

The general purpose solver CFDShip-Iowa, solves the Unsteady Reynolds Averaged Navier-Stokes equations in the liquid phase of a free surface flow.

The governing differential equations are derived and solved in the absolute inertial earth-fixed coordinate system *(X,Y,Z)* for an arbitrary moving but non-deforming control-volume around the hull and for a solution domain respectively, as displayed in Fig.2.1.

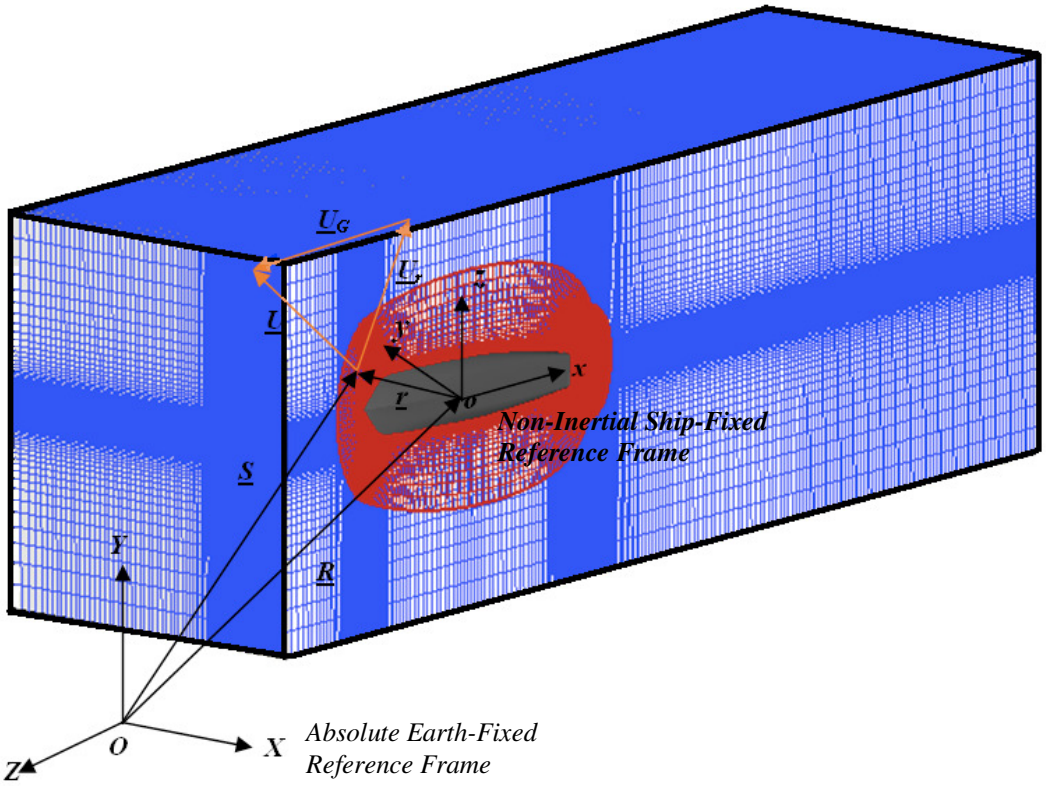

Fig.2.1 Definition of the absolute inertial earth-fixed coordinates *(X,Y,Z)* and non-inertial ship-fixed coordinates *(x,y,z)* with its origin *o* in the ship centre of gravity. The grid around the hull (red) is the moving but non-deforming control volume, while the box (blue) corresponds to the solution domain.

A non-inertial ship-fixed reference frame *(x,y,z),* whose origin *o* is located at the centre of gravity (COG) of the ship, is related to the fixed reference frame by the vector $\underline{R}$. Therefore, if $\underline{r}$ is the instantaneous position vector of any point in *(x,y,z)*, $\underline{S} = \underline{R} + \underline{r}$ is the position vector of the same point in the absolute reference frame. If $\underline{U}_G$ is the velocity of the non-deforming control volume, the fluid relative velocity is calculated as:

$$\underline{U}_r = \underline{U} - \underline{U}_G \tag{2.6}$$

where $\underline{U}$ is the fluid absolute velocity in *(X,Y,Z)*.

Conservation of mass is given by:

$$\nabla \cdot \underline{U}_r = 0 \tag{2.7}$$

The control volume is not deforming, hence $\nabla \cdot \underline{U}_G = 0$. Therefore, substitution of Eq.(2.6) in Eq.(2.7), gives:

$$\nabla \cdot \underline{U} = 0 \tag{2.8}$$

The momentum equations, in the same reference frame are non-dimensionalized with ship length, L_0, reference velocity U_0, water density ρ and viscosity μ, and are given by:

$$\frac{\partial \underline{U}}{\partial t} + (\underline{U} - \underline{U}_G) \cdot \nabla \underline{U} = -\nabla p + \frac{1}{\mathrm{Re}} \nabla^2 \underline{U} \tag{2.9}$$

where p is given by:

$$p = \frac{p_{abs}}{\rho U_0^2} + \frac{z}{Fn^2} \tag{2.10}$$

z is the coordinate in the vertical direction and Fn is the Froude number. The same equation can be derived in the ship-fixed reference frame and in this case $U_G=0$ .Therefore, Eq.(2.9) can be re-written as:

$$\frac{\partial \underline{U}_r}{\partial t} + \underline{U}_r \cdot \nabla \underline{U}_r = -\underline{a}_r - \nabla p + \frac{1}{\mathrm{Re}} \nabla^2 \underline{U}_r \tag{2.11}$$

that includes an additional body force term (a_r), that takes into account the non-inertial effects and that is given by:

$$\underline{a}_r = \ddot{\underline{R}} + 2\underline{\Omega}_V \times \underline{U}_r + \underline{\Omega}_V \times \left(\underline{\Omega}_V \times \underline{r}\right) + \dot{\underline{\Omega}}_V \times \underline{r} \tag{2.12}$$

where $\underline{\Omega}_V$ is the angular velocity of the ship in *(X,Y,Z)*. This transformation from the *(X,Y,Z)* to the *(x,y,z)* shows the difference between the equations expressed in an absolute reference frame and a non-inertial ship reference frame. After Reynolds averaging, Eq.(2.9) can be expressed in scalar form as:

$$\frac{\partial u_i}{\partial t} + (u_j - U_{Gj}) \frac{\partial u_i}{\partial x_j} = -\frac{\partial p}{\partial x_i} + \frac{1}{\mathrm{Re}} \frac{\partial^2 U_i}{\partial x_j \partial x_i} - \frac{\partial}{\partial x_j} \overline{u'_i \, u'_j} \tag{2.13}$$

For the problem closure, the Reynolds stresses are determined by using an appropriate turbulence model.

2.4.2 Turbulence modeling

To compute turbulence viscosity, the blended k-ε/k-ω turbulence model has been used. It is a combination of k-ω and k-ε models that keeps the advantages of both models. In particular, the k-ω model is used in the viscous sub-layer because does not involve damping functions allowing a simple Dirichlet

boundary condition to be specified at solid wall, and in the log-layer for its capability in predicting adverse pressure gradient flows. Then it is better than other models with regard to numerical stability.

In the wake region of the boundary layer and in the free shear layers, the *k-*ω model must be abandoned in favor of the *k-*ε. The *k-*ω, in fact, presents some deficiencies related to the high sensitivity to the quite arbitrary free-stream, ω_f, specified for ω outside the boundary layer. On the contrary, the *k-*ε does not exhibit this deficiency and seems to be a fair compromise in predicting shear flows. To achieve the desired features in the different regions, a blending function F_1 is defined that is designed to be one in the viscous sub-layer and log-layer, activating the *k-*ω model and then gradually switches to zero in the outer wake region and free shear layers, activating the *k-*ε model.

The original *k-*ω is based on the following equations:

$$\frac{\mathrm{D}\rho \mathrm{k}}{\mathrm{Dt}} = \tau_{ij}\frac{\partial u_i}{\partial x_j} - \beta^*\rho\omega\kappa + \frac{\partial}{\partial x_j}\left[(\mu + \sigma_{k1}\mu_t)\frac{\partial k}{\partial x_j}\right] \tag{2.14}$$

$$\frac{\mathrm{D}\rho\omega}{\mathrm{Dt}} = \frac{\gamma_1}{\nu_t}\tau_{ij}\frac{\partial u_i}{\partial x_j} - \beta_1\rho\omega^2 + \frac{\partial}{\partial x_j}\left[(\mu + \sigma_{\omega 1}\mu_t)\frac{\partial \omega}{\partial x_j}\right] \tag{2.15}$$

where $\nu_t = \frac{k}{\omega}$, $\beta^*, \beta_1, \kappa, \sigma_{\omega 1}$ and σ_{k1} are the model constants. The *k-*ε model is transformed into a *k-*ω formulation, assuming the following expression:

$$\frac{\mathrm{D}\rho \mathrm{k}}{\mathrm{Dt}} = \tau_{ij}\frac{\partial u_i}{\partial x_j} - \beta^*\rho\omega\kappa + \frac{\partial}{\partial x_j}\left[(\mu + \sigma_{k2}\mu_t)\frac{\partial k}{\partial x_j}\right] \tag{2.16}$$

$$\frac{\mathrm{D}\rho\omega}{\mathrm{Dt}} = \frac{\gamma_2}{\nu_t}\tau_{ij}\frac{\partial u_i}{\partial x_j} - \beta_2\rho\omega^2 + \frac{\partial}{\partial x_j}\left[(\mu + \sigma_{\omega 2}\mu_t)\frac{\partial \omega}{\partial x_j}\right] + 2\rho\sigma_{\omega 2}\frac{1}{\omega}\frac{\partial k}{\partial x_j}\frac{\partial \omega}{\partial x_j} \tag{2.17}$$

with $\beta_2, \sigma_{\omega 2}$ and σ_{k2} the model constants. With the upper transformation, Eq (2.14) and (2.15), are multiplied by F_1 and Eq.(2.16) and (2.17) are multiplied by (1-F1). By adding the corresponding equations of both models, the equations for the new model are obtained as follows:

$$\frac{\mathrm{D}\rho \mathrm{k}}{\mathrm{Dt}} = \tau_{ij}\frac{\partial u_i}{\partial x_j} - \beta^*\rho\omega\kappa + \frac{\partial}{\partial x_j}\left[(\mu + \sigma_k\mu_t)\frac{\partial k}{\partial x_j}\right] \tag{2.18}$$

$$\frac{\mathrm{D}\rho\omega}{\mathrm{Dt}} = \frac{\gamma}{\nu_t}\tau_{ij}\frac{\partial u_i}{\partial x_j} - \beta\rho\omega^2 + \frac{\partial}{\partial x_j}\left[(\mu + \sigma_{\omega 2}\mu_t)\frac{\partial \omega}{\partial x_j}\right] + 2\rho(1-F_1)\sigma_{\omega 2}\frac{1}{\omega}\frac{\partial k}{\partial x_j}\frac{\partial \omega}{\partial x_j} \tag{2.19}$$

If ϕ_1 are the constants in the original k-ω and ϕ_2 are the constants in the k-ε, in the new model the constants are obtained as:

$$\phi = F_1\phi_1 + (1 - F_1)\phi_2 \tag{2.20}$$

It can be observed that if F_1=0 then the equations and the constants are the same as Eq (2.16) and (2.17) relative to the k-ε model. When F_1=1, the equations and constants corresponding to the k-ω model are obtained.

The blending function is defined as:

$$F_1 = \tanh\left(\arg_1^4\right) \tag{2.21}$$

where

$$\arg_1 = \min\left[\max\left(\frac{\sqrt{k}}{0.09\omega y};\frac{500\nu}{y^2\omega}\right);\frac{4\rho\sigma_{\omega 2}k}{CD_{k\omega}y^2}\right] \tag{2.22}$$

and y is the distance from the wall. It can be seen that arg_1 goes to zero far enough away from the solid surface for the presence of $1/y$ and $1/y^2$ in the three terms of Eq.(2.22). Finally the Dirichlet function is defined as:

$$\omega = \frac{60\nu}{\beta_1\left(\Delta y_1^2\right)} \quad \text{at } y = 0 \tag{2.23}$$

being Δy_1 the distance to the next point away from the wall.

2.4.3 Free surface modeling

Among the surface-capturing techniques, the level-set methods are becoming very popular in predicting moving interfaces and can predict the evolution of complex flows including waves with large slopes, wave breaking, deforming bubbles and droplets, break up and coalescence, etc [3]. The free surface of ship flows is only one particular case of a more general problem involving the evolution of the interface between two or more fluids.

In the classical level-set approach, equations for both fluids are solved. However, there are some fluid/fluid problems in which the interface can be considered as a free boundary and hence the computation can be limited to the more viscous and dense fluid (single-phase level-set method). The solution of the equations involving water phase only, presents more advantages in terms of

robustness in computation than in terms of computational time over the classical level-set approach involving both phases. In this case, in fact, only one fluid with constant properties is solved. Therefore, the classical pressure and velocity oscillations present at the interface between two fluids with high density ratios, are circumvented. Another advantage is that pressure is not solved in air and velocity and turbulence quantities follow a linear convection equation, resulting in a faster computation. However, this method needs the introduction of a boundary condition for pressure at the interface. As the computational grid is fixed in space and time, the detection of the free surface is necessary and this has a cost in terms of computation time.

Two conditions have to be satisfied in using the single-phase level-set method. The first one arises from the consideration that the continuity equation is solved only in water phase and not in the air phase. Therefore, the method is not suitable for problems in which the air phase gets pressurized as in the case of formation of bubbles in water or when air is trapped in the liquid phase. The other condition is that the stresses caused by the air phase on the liquid must be negligible since no computation is made in the air phase. In addition to these limitations, the method has no restrictions on the surface topology, allowing large amplitude and steep waves.

The location of the free surface is given by the zero level-set of the function ϕ, which is a distance to the interface function, positive in liquid and negative in air. Since the free surface is a material interface, the equation for level-set function is given by:

$$\frac{\partial \phi}{\partial t} + \underline{U} \cdot \nabla \phi = 0 \tag{2.24}$$

As the equations of motions are solved in water phase only, a proper jump condition must be explicitly enforced at the free surface. The jump condition, in any direction tangential to the free surface, is expressed as:

$$\nabla \underline{U} \cdot \underline{n} = 0 \tag{2.25}$$

In the direction normal to the interface, the jump condition is :

$$p_{\text{int}} = \frac{z}{Fn^2} \tag{2.26}$$

where p_{int} is the dimensionless piezometric pressure at the water-air interface, z is the coordinate in the vertical direction and Fn is the Froude number. As previously seen, as the grid is fixed in the surface-capturing techniques, the free surface is not located at the grid points. An interpolation scheme is needed

to enforce the derived jump conditions at the interface. Therefore, for grid points in air Eq.(2.26) is enforced, while for grid points in water that have at least one neighbor in air (n_a), the interfacial pressure, p_{int}, is obtained by the following expression:

$$p_{\text{int}} = \frac{(1-\eta)z_p + \eta z_{n_a}}{Fn^2} \tag{2.27}$$

where η (Fig. 2.2) is the relative distance between the grid point in water, p, and the interface (*int*) and is defined as:

$$\eta = \frac{\phi_p}{\phi_p - \phi_{n_a}} \tag{2.28}$$

The pressure at the neighbor in air, p_{na}, is then calculated as:

$$p_{na} = (p_{\text{int}} - p_h)\frac{dist(\underline{r}_{n_a}, \text{int})}{dist(\underline{r}_p, \text{int}) + dist(\underline{r}_p, \underline{r}_h)} + p_{\text{int}} \tag{2.29}$$

where the point h is halfway between the local point p and the opposite neighbor in water to n_a (Fig.2.2), shown as n_w:

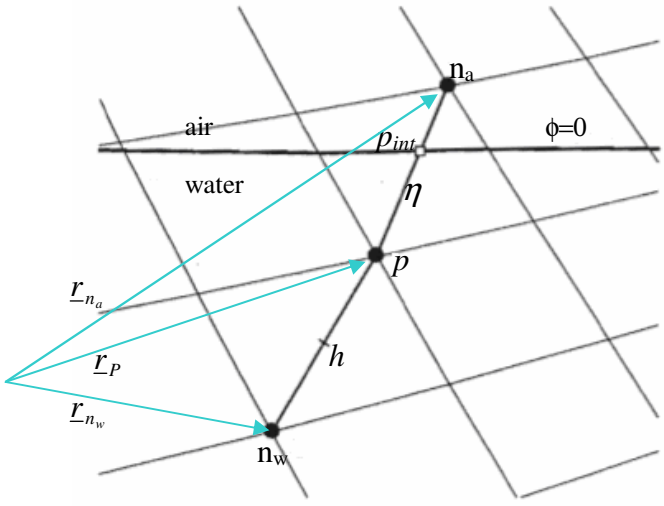

Fig.2.2 Computation of the free surface location and calculation of the neighbour pressure to enforce pressure boundary condition at the interface. ϕ=0 denotes the free surface, η is the distance between grid point p in water and the free surface, n_a is the neighbor point in air. Pressure at the interface is calculated as $p_{int}=((1-\eta)z_p+\eta z_{na})/Fn^2$.

2.4.4 Rigid body equations and 6DOF module

The forces and moments acting on the ship are initially computed in the inertial earth-fixed reference frame *(X,Y,Z)*, where the fluid flow equations are solved. The pressure forces acting on the hull surface are calculated by integrating the hydrostatic and piezometric pressures calculated by the Navier-Stokes equations:

$$\underline{F}_{e,P} = -\int_{ship}\left(p - \frac{z}{Fn^2}\right)d\underline{a} \tag{2.30}$$

where $\underline{a}$ is the outward pointing area vector and e denotes the earth reference frame. The frictional forces are computed by:

$$\underline{F}_{e,f} = \frac{1}{2\,\mathrm{Re}}\int_{ship}\left(\nabla\underline{U} + \nabla\underline{U}^T\right)d\underline{a} \tag{2.31}$$

Thus the total force is:

$$\underline{F}_e = \underline{F}_{e,p} + \underline{F}_{e,f} \tag{2.32}$$

The total moments are calculated by integrating the elemental forces with the distance from the center of gravity:

$$\underline{M}_e = \int_{ship}\underline{r}_{CG} \times \left\{\left[\left(\frac{\nabla\underline{U} + \nabla\underline{U}^T}{2\,\mathrm{Re}}\right) - \left(p - \frac{z}{Fr^2}\right)\underline{I}\right]\cdot da\right\} \tag{2.33}$$

$\underline{F}_e$ and $\underline{M}_e$ are then projected in the non-inertial ship-fixed coordinate system *(x,y,z)* by using:

$$\underline{F}_s = \underline{J}_1(\underline{F}_e) = (F_x, F_{y,}F_z) \tag{2.34}$$

$$\underline{M}_s = \underline{J}_1(\underline{M}_e) = (M_x, M_y, M_z) \tag{2.35}$$

where the $\underline{J}_1$ matrix transforms any vector in *(X,Y,Z)* to a vector in *(x,y,z)*. Usually results are presented in terms of non-dimensional forces and moments coefficients expressed as follows:

$$C_x = \frac{X}{0.5\rho U_0^2 A_W} \tag{2.36}$$

$$M_x = \frac{M}{0.5\rho U_0^2 L A_W} \tag{2.37}$$

where C_X and M_X are the force and moment coefficient in the x direction and A_w is the wetted area in static conditions.

The evolution of the location of the ship is computed solving the rigid body equations in the non-inertial ship-fixed reference frame *(x,y,z)*.

$\underline{U}_b = (u_b, v_b, w_b)$ is the velocity vector that describes the translation of the ship, and its components in the *x, y* and *z* direction are respectively the surge, sway and heave of the ship in *(x,y,z)*. $\underline{\Omega}_b = (\Omega_x, \Omega_y, \Omega_z)$ is the angular velocity of the ship in *(x,y,z)* and its components are the rate of change respectively of roll, pitch and yaw angles that describe the ship rotation, $\eta=(\phi,\theta,\psi)$. The coordinate system is chosen to be aligned with the principal axes of inertia and has its origin in the center of gravity of the ship. With these assumptions, the rigid body equations can be written as:

$$\left[m\left(\dot{u}_b - v_b\Omega_z + w_b\Omega_y\right)\right] = F_x \tag{2.38}$$

$$\left[m\left(\dot{v}_b - w_b\Omega_x + u_b\Omega_z\right)\right] = F_y$$

$$\left[m\left(\dot{w}_b - u_b\Omega_y + v_b\Omega_x\right)\right] = F_z$$

$$\left[I_x\dot{\Omega}_x + \left(I_z - I_y\right)\Omega_y\Omega_z\right] = M_x$$

$$\left[I_y\dot{\Omega}_y + \left(I_x - I_z\right)\Omega_x\Omega_z\right] = M_y$$

$$\left[I_z\dot{\Omega}_z + \left(I_y - I_x\right)\Omega_x\Omega_y\right] = M_z$$

In the equations, m is the mass of the ship, I_x, I_y and I_z are the momentum of inertia of the ship relative to *x, y* and *z* respectively and the terms on the right side are the total forces and moments acting on the ship in the *i* direction and include the buoyancy, gravity and propeller thrust force. Integration of Eq.(2.38) gives $\underline{U}_b$ and $\underline{\Omega}_b$ that are transformed back to $\underline{U}_V$ and $\underline{\Omega}_V$ in the earth-fixed reference frame using:

$$\underline{U}_V = \underline{J}_1^{-1}(\underline{U}_b) \tag{2.39}$$

$$\underline{\Omega}_V = \underline{J}_1^{-1}(\underline{\Omega}_b) \tag{2.40}$$

where $\underline{U}_V=(u,v,w)$ are the ship velocity components in (X,Y,Z). Therefore, the new positions of the ship are calculated by integrating $\underline{U}_V$ and $\underline{\Omega}_V$:

$$\underline{R} = \underline{R}_{initial} + \int_0^T \underline{U}_V dt \tag{2.41}$$

$$\underline{\eta} = \underline{\eta}_{initial} + \int_0^T \underline{\Omega}_V dt \tag{2.42}$$

2.4.5 The code SUGGAR

The computation of ship motions is made possible by the use of a dynamic overset-grid approach. The overset-grid methodology allows the use of a set of overlapping grids to discretize the domain. This methodology is useful not only to simplify the grid generation requirements for complex geometries but is also an enabling technology for the simulation of bodies in relative motion. In particular, the computational domain is composed of static and moving grids. The static grids are fixed to the earth-fixed reference frame (X,Y,Z) and are designed to properly resolve the air/water interface and the incident waves. The static grids also extend far away from the ship so that the far-field boundary conditions are imposed only on them. On the contrary, the moving grids are attached to moving boundaries (i.e. ships, rudders, etc.) on the inertial reference frame and they are fully immersed in the static grids (Fig.2.1 and 2.3).

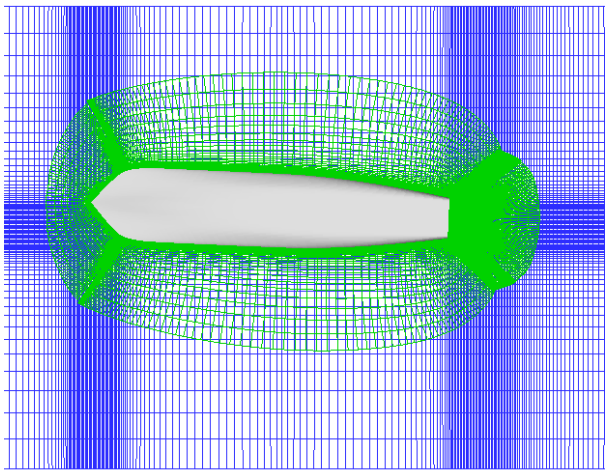

Fig.2.3 Example of overlapping grids around a body. The blue grid is the background static grid. The green grid is the body-fitted grid, attached to the moving body and fully immersed in the static grid.

To couple the solution of the various grids, interpolation at appropriate points is used. In particular, any points that lie outside the domain of interest, for example inside of a body or behind a symmetry plane, are blanked out from calculations and are termed "hole points". Points that surround the hole points become new inter-grid boundary points, which are called fringe or receptor points, and require boundary values that are provided by interpolating from a donor grid that overlaps the region. Therefore, the overset grid assembly process provides the domain connectivity information, which is the definition of which points are receptor points along with their corresponding donor members and which are hole points. In the dynamic approach, every time a grid is moved new interpolation coefficients need to be computed to link the moving grids with the static grids and between each other (Fig.2.4)

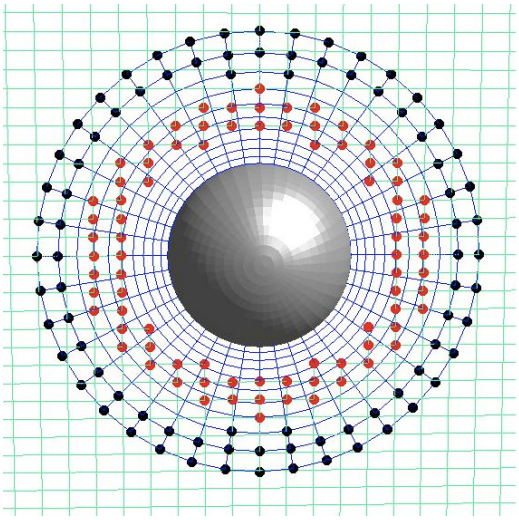

Fig.2.4 Overlapping grids around a sphere. Blue grid lines: o-grid around sphere; Green grid lines: box grid; Red symbols: box-grid points receiving data from sphere; Black symbols: sphere-grid points receiving data from box.

The SUGGAR code (Structured, Unstructured and Generalized overset Grid Assembler) [24] is used herein to obtain the overset domain connectivity between the overlapping grids, as it is capable of providing overset domain connectivity for node centered solvers as CFDShip-Iowa.

2.4.6 Numerical modeling and solution strategy

In order to accommodate the complex body geometries, generalized curvilinear coordinates are used and the governing differential equations in the physical domain *(X,Y,Z,t)* are transformed into the computational domain (ξ,η,ζ,τ). As example, the continuity and momentum equations become:

$$\frac{1}{J}\frac{\partial}{\partial \xi^j}(b_i^j u_i) = 0 \tag{2.43}$$

$$\frac{\partial u_i}{\partial \tau} + \frac{1}{J} b_j^k (u_j - U_{Gj}) \frac{\partial u_i}{\partial \xi^k} = -\frac{1}{J} b_i^k \frac{\partial p}{\partial \xi^k} + \frac{1}{J}\frac{\partial}{\partial \xi^j}\left(\frac{b_i^j b_i^k}{\partial \mathrm{Re}_{eff}} \frac{\partial u_i}{\partial \xi^k} \right) + \frac{b_j^k}{J}\frac{\partial \nu_t}{\partial \xi^k}\frac{b_i^l}{J}\frac{\partial u_j}{\partial \xi^l} + S_i \tag{2.44}$$

where J and b_i^j are the Jacobian and the metrics of the transformation. The continuum equations are then discretized by using finite differences. In particular, the second order upwind scheme is used to discretize the convective terms of momentum equations. For an arbitrary variable φ, these terms can be expressed as:

$$\frac{1}{J}\frac{\partial}{\partial \xi_k}\left[b_j^k \left(u_j - \frac{\partial x_j}{\partial \tau} \right) \varphi \right] = \frac{1}{J}\left[(C_d - C_u) + (C_e - C_w) + (C_n - C_s) \right] \tag{2.45}$$

where *d, u, e, w, n* and *s* indicate the down, up, east, west, north and south faces of the control volume and are located respectively at $i+1/2$, $i-1/2$, $j+1/2$, $j-1/2$, $k+1/2$ and $k-1/2$. The terms on the right-hand side are given by expressions of the following type (for example at the down face):

$$C_d = \tilde{U}_d \left[\alpha_d (a\varphi_{i+1} + b\varphi_i + c\varphi_{i-1}) + (1-\alpha_d)(d\varphi_i + e\varphi_{i+1} + f\varphi_{i+2} \right] \tag{2.46}$$

where $\tilde{U}_d$ and α_d are defined as:

$$\tilde{U}_d = \left[b_j^1 \left(u_j - \frac{\partial x_j}{\partial \tau} \right) \right]_{i+1/2} \tag{2.47}$$

$$\begin{cases} \alpha_d = 0 \quad if \quad \tilde{U}_d > 0 \\ \alpha_d = 1 \quad if \quad \tilde{U}_d < 0 \end{cases} \tag{2.48}$$

For C_u, C_e, C_w, C_n and C_s expressions similar to (2.46) hold. The coefficients for the second-order upwind scheme are: a=0, b=1.5, $c = -0.5$, d=0, e=1.5, $f = -0.5$.

Viscous terms and turbulence equations are discretized by using second-order central differences, while time derivatives are discretized by means of the following formulation:

$$\frac{\partial \varphi}{\partial \tau} = \frac{1}{\Delta \tau}\left(1.5\varphi^{n} - 2\varphi^{n-1} + 0.5\varphi^{n-2}\right) \tag{2.49}$$

Therefore the discretized form of Eq.(2.44), for any interior point is:

$$u_i = -\frac{\sum_{nb} a_{nb} u_{i,nb} - S_i}{a_{ijk}} - \frac{b_i^k}{J a_{ijk}} \frac{\partial p}{\partial \xi^k} \tag{2.50}$$

where a_{ijk} and a_{nb} are the pivot and neighbor coefficients from the discretization scheme. A pressure implicit split operator (PISO) algorithm is used to enforce continuity. The mass equation (2.43) can be enforced by means of the discretized form of the momentum equation (2.50) resulting in a Poisson equation for pressure that has the following form:

$$\frac{\partial}{\partial \xi^j}\left(\frac{b_i^j b_i^k}{J a_{ijk}} \frac{\partial p}{\partial \xi^k}\right) = \frac{\partial}{\partial \xi^j} \frac{b_i^j}{a_{ijk}} \left(\sum_{nb} a_{nb} u_{i,nb} - S_i\right) \tag{2.51}$$

Within the single-phase level-set method, this condition is enforced only in water.

The overall solution strategy is presented in Fig. (2.5):

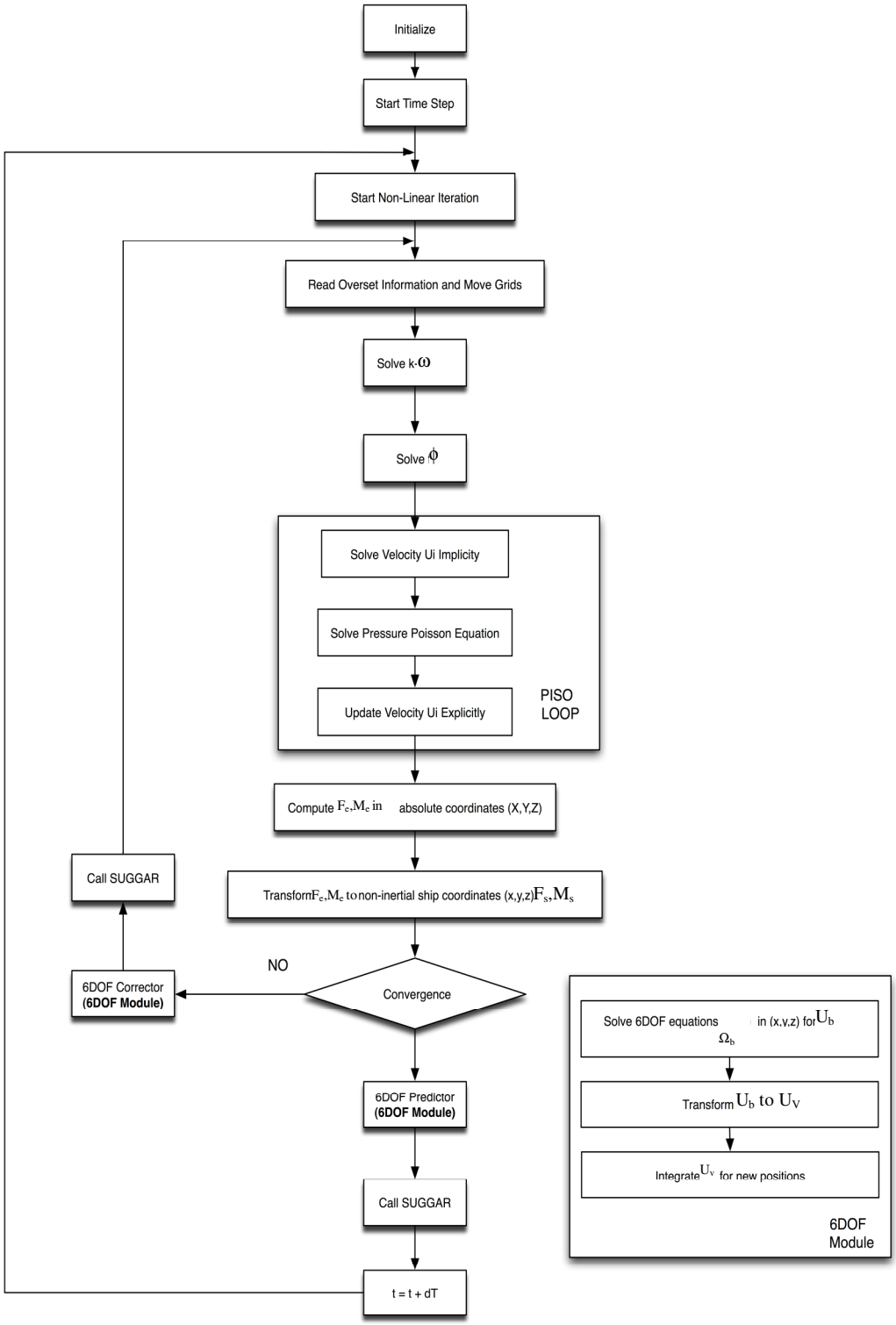

Fig. 2.5 Overall solution strategy implemented in the code CFDSHIP-Iowa

Once the variables are initialized, the code SUGGAR is called for the first time to obtain the initial overset interpolation information. A non-linear loop is used for the convergence of the flow field and motions within each time step. At the beginning of each non-linear iteration, the overset information is read from a binary file produced by SUGGAR, grids are moved according to the motions resulting from the 6DOF predictor/corrector steps and transformation metrics and grid velocities are computed. Then the flow-solver solution starts. First, the k-ω equations are solved, followed by the level-set function transport and re-initialization. With the new location of the free surface, the first step of the PISO loop starts, pressure gradient is calculated and velocity is implicitly solved, then the pressure is obtained solving the Poisson equation. Finally, pressure gradient is computed and velocity is calculated explicitly in the last step of the PISO iteration. Once the updated flow field is obtained, the forces and moments are calculated by using Eq.(2.32) and (2.33), velocities are transformed back in the fixed reference frame with the 6DOF module and the new position of the ship is calculated. Global residuals are then evaluated. If the residuals of all variables drop to 10^{-3} indicating convergence for that time-step, motions are predicted for the next time-step using a first order Euler difference given by the following expression for any degree of freedom φ:

$$\dot{\varphi}^n = \dot{\varphi}^{n-1} + \Delta t \ddot{\varphi}^{n-1} \tag{2.52}$$

$$\varphi^n = \varphi^{n-1} + \Delta t \dot{\varphi}^{n-1} \tag{2.53}$$

The code SUGGAR is called to compute the interpolation given the new location of the moving grids. If the non-linear iteration is not convergent for the time-step, then the motion vectors are corrected using a third-order approximation for time derivatives:

$$\dot{\varphi}^n = \dot{\varphi}^{n-1} + \Delta t\left(5\ddot{\varphi}^n + 8\ddot{\varphi}^{n-1} - \ddot{\varphi}^{n-2}\right) \tag{2.54}$$

$$\varphi^n = \varphi^{n-1} + \Delta t\left(5\dot{\varphi}^n + 8\dot{\varphi}^{n-1} - \dot{\varphi}^{n-2}\right) \tag{2.55}$$

The code SUGGAR is then called and a new non-linear iteration is started. Two-five non-linear iterations are usually required for convergence of the flow field equations within each time step. Convergence for pressure equation is reached when the residual imbalance of the Poisson equation drops six orders of magnitude while convergence of all other variables is reached when residuals drop to 10^{-5}.

Chapter 3

Simulation Conditions for predicting the Seakeeping behavior of the DELFT Catamaran in Regular Head Waves

3.1 Introduction

This work reports the investigation on the behavior of a high speed multi-hull vessel advancing in regular waves which was carried out by means of the RANS code CFD-Ship IOWA, Version 4. The geometry under consideration is the Delft catamaran model 372, designed and tested at Delft University of Technology (1998), for which experimental results are available.

In the present chapter modeling conditions and design parameters will be described in detail.

The application of RANS codes to model seakeeping problems is very recent. Typical seakeeping solution techniques were based on the linear strip theory, first presented by Salvesen et al. [35,37]. In strip theory, it is assumed that the wave induced motion amplitudes are proportional to wave amplitude. As a consequence, the ship motions in irregular waves can be obtained simply by adding the response to regular waves of different amplitudes, phases, wavelength and propagation directions. Another consequence is that the fully non-linear governing equations of ship motions are simplified in two sets of uncoupled linear differential equations, one for vertical plane and one for horizontal plane motions. Results of previous studies show that prediction of motion in the vertical plane is more accurate than in the horizontal plane, but solutions for heave and pitch also fail when the hypotheses of linear behavior are no more applicable as in the case of high steep waves, where the assumptions of potential flow and small amplitudes of the incoming waves are not valid. Thus, recently much effort was done to apply and to extend the use of RANS methods in seakeeping problems, since effects due to viscosity, creation of vorticity in the boundary layer, vortex shedding, and turbulence are implicitly included.

Usually ship motions are calculated in a right-handed ship-fixed inertial reference frame *(x,y,z)*, with positive *z* vertically upward through the centre of gravity of the ship and the origin in the undisturbed free surface. The degrees of freedom of a ship advancing in water are described in Fig. 3.1:

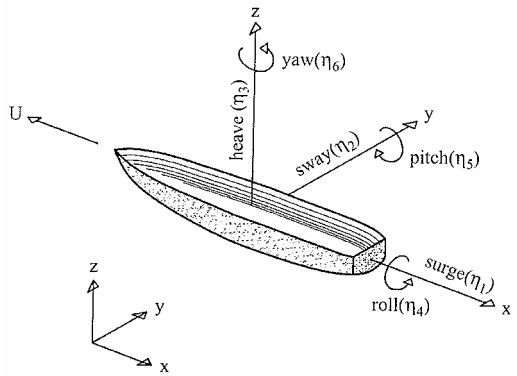

Fig.3.1 Definition of the coordinate system and of the rigid body motion modes. U is the forward speed of the ship. The coordinate system moves with the forward speed of the vessel but does not oscillate . The origin, *o*, is on the undisturbed free surface and the *z* axis passes through the centre of gravity**.**

For a ship advancing in regular head waves, heave and pitch are the only wave-induced motions, other motions being negligible. Recently, Irvine et al.[15] and Simonsen et al.[39], focused on heave and pitch motions for mono-hulls advancing in waves and investigated the maximum response and resonance conditions, but at the moment no studies exist on the response of multi-hull vessels. This work reports an attempt to extend to twin-hulls the results previously obtained for mono-hulls. In particular, in the present work, heave and pitch motions were predicted for different ship speeds and wavelength ranges, and the effects of resonance and exciting forces due to the incoming wave on maximum response of the catamaran were investigated. The catamaran was studied for Fn=0.45, Fn=0.6 and F=0.75 which is a realistic operating range for existing catamaran vessels. For each speed, a range of wavelengths going from λ/L_{pp}=0.9 to λ/L_{pp}=2 was considered. Time histories, running mean and FFT analysis will be presented and for a specific operating condition, verification and validation study was also conducted.

The effects of incoming wave steepness on the response of the ship were also studied to evaluate the linearity of heave and pitch responses, and the results for three values of wave steepness (Ak=0.025, Ak=0.05 and Ak=0.1) were compared.

Finally, the effects of incoming waves on ship resistance were evaluated. In fact, the interaction between the incident waves and the ship gives origin to a new component of resistance, the added resistance, that is defined as the difference between the total resistance in waves and the resistance in calm

water. Therefore, to determine the added resistance in waves, simulations were performed in calm water too, for a speed range varying from Fn=0.3 to Fn=0.75 and resistance, sinkage and trim were also evaluated.

3.2 Model Geometry and Test Conditions

Experiments with the 372 catamaran model were carried out [44,45] in the Delft Ship Hydrodynamic Laboratory of the Delft University of Technology, in a towing tank with dimensions LxBxD=145mx4.2mx2.6m.The lines plan is given in Fig. 3.2 and the main characteristics are given in Table 3.1:

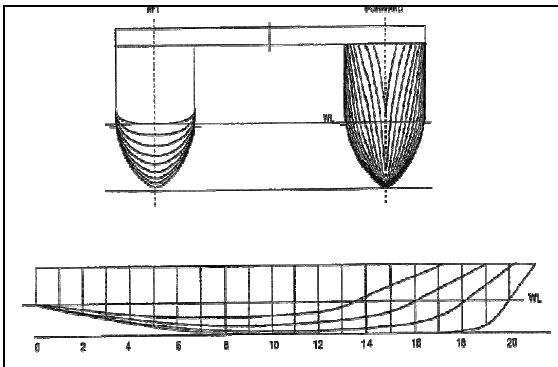

Fig. 3.2 Lines Plan of Delft catamaran

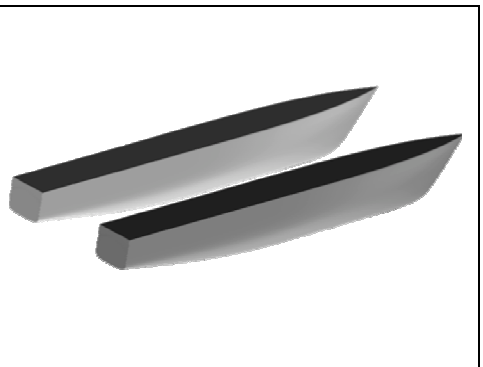

Fig. 3.3 Delft Catamaran geometry

Table 3.1. Main design parameters of the DELFT catamaran geometry.

Main Particulars	Units	Value
Lenght overall, L_{OA}	m	3.11
Lenght between perpendiculars, L	m	3
Beam overall, B	m	0.94
Beam demihull, b	m	0.24
Distance between center of hulls, H	m	0.7
Draught, T	m	0.15
Displacement, Δ	Kg	87.07
Draught AP, T_{AP}	m	0.15
Draught FP, T_{FP}	m	0.15
Vertical Center of Gravity, KG	m	0.34
Longitudinal Center of Gravity, LCG	m	1.41

The experimental program included both still-water resistance and heave and pitch motion tests. A schematic of the experimental apparatus used for both test conditions is illustrated in Fig. 3.4:

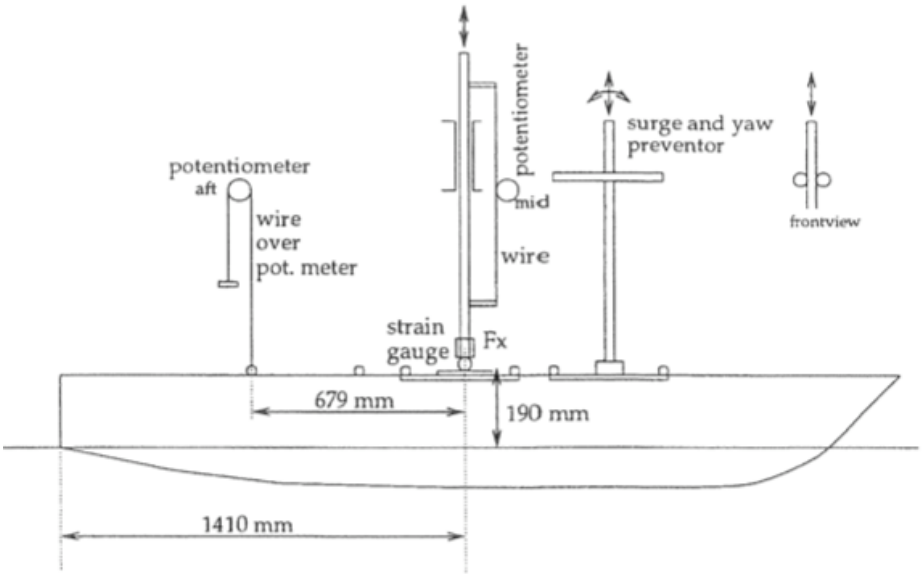

Fig.3.4 Experimental set-up for wave resistance, trim and sinkage measurements and for heave and pitch motion tests.

The still-water resistance tests were carried out to obtain the resistance, sinkage and trim of the model over a speed range $Fn = 0.18\text{-}0.75$. The sinkage of the model was measured at the center of gravity using a potentiometer and a wire connected to the model. An extra measure of sinkage at a second point positioned at 679mm behind the centre of gravity allowed the calculation of trim angle from the two vertical displacements. Values of resistance were useful in the present work to evaluate added resistance in waves.

Heave and pitch motion tests were carried out in the same towing tank where regular head waves were generated. The un-propelled model was towed at uniform constant speed and was restrained from all motions but heave and pitch. The motions were measured with the same experimental apparatus as in Fig.(3.4). Vertical displacements were recorded at the centre of gravity and at the second point 679mm behind it, and heave and pitch motions were calculated. In particular, experiments were carried out at four different forward speed values (Fn=0.3, 0.45, 0.6 and 0.75) and for each speed under several wave frequency conditions according to table 3.2:

Table 3.2. Test matrix for heave and pitch motions

Fn	Steepness	λ/L_{pp}	Enc. Frequency (Hz)
0.45	0.030	1.001	1.53
0.45	0.030	1.201	1.33
0.45	0.027	1.396	1.19
0.45	0.025	1.595	1.08
0.45	0.020	1.991	0.92
0.6	0.030	1.393	1.44
0.6	0.026	1.49	1.319
0.6	0.025	1.6	1.25
0.6	0.021	1.795	1.14
0.6	0.021	1.977	0.9
0.75	0.025	1.596	1.42
0.75	0.022	1.806	1.287
0.75	0.015	1.983	1.196
0.75	0.015	2.012	1.183

The steepness of the incoming wave is defined as $Ak = 2\pi A/\lambda$, where A is the wave amplitude, $k = 2\pi/\lambda$ is the wave number and λ is the wave length. The encounter frequency is defined as:

$$f_e = \sqrt{\frac{g}{2\pi\lambda}} + \frac{U_0}{\lambda} \tag{3.1}$$

where U_0 is the ship speed.

Data were recorded [44,45] as time histories to facilitate the harmonic analysis of the incident wave and of the related heave and pitch motions. Experimental data were then approximated with Fourier series (FS) expansions as:

$$x_5(t) = x_{5_0} + x_{5_1}\cos\left(2\pi f_e t + \gamma_{x_{51}}\right) + x_{5_2}\cos\left(4\pi f_e t + \gamma_{x_{52}}\right) + x_{5_3}\cos\left(6\pi f_e t + \gamma_{x_{53}}\right) \tag{3.2}$$

$$x_3(t) = x_{3_0} + x_{3_1}\cos\left(2\pi f_e t + \gamma_{x_{31}}\right) + x_{3_2}\cos\left(4\pi f_e t + \gamma_{x_{32}}\right) + x_{3_3}\cos\left(6\pi f_e t + \gamma_{x_{33}}\right) \tag{3.3}$$

where x_{5_n} and x_{3_n} are the *n*-th order harmonic amplitudes of pitch and heave respectively, and γ_{x5n} and γ_{x3n} are the phases of the n-th harmonic for pitch and heave respectively. Amplitude response results of heave and pitch (output) as a function of the incoming wave (input), are usually presented in terms of the standard transfer functions (TF) defined as:

$$TF_{x5} = \frac{x_{51}}{kA} \tag{3.4}$$

$$TF_{x3} = \frac{x_{31}}{A} \tag{3.5}$$

where x_{51}, x_{31} and A are the first harmonic components of pitch, heave and incoming wave respectively.

Motions are referred to the longitudinal centre of gravity (LCG) of the ship.

3.3 Grids

In order to predict ship motions, numerical simulations were performed according to the conditions described in Table 3.2. For this purpose, a computational domain was realized by using an overlapping grids approach. The computational domain is made, therefore, of a background orthogonal grid and a body fitted grid (Fig.3.5 a), fully immersed in the background (Fig.3.5 b). The grids were generated by the hyperbolic grid-generator GRIDGEN(by POINTWISE) and the connectivity between the domains was obtained by the code SUGGAR(Par.2.4.5).

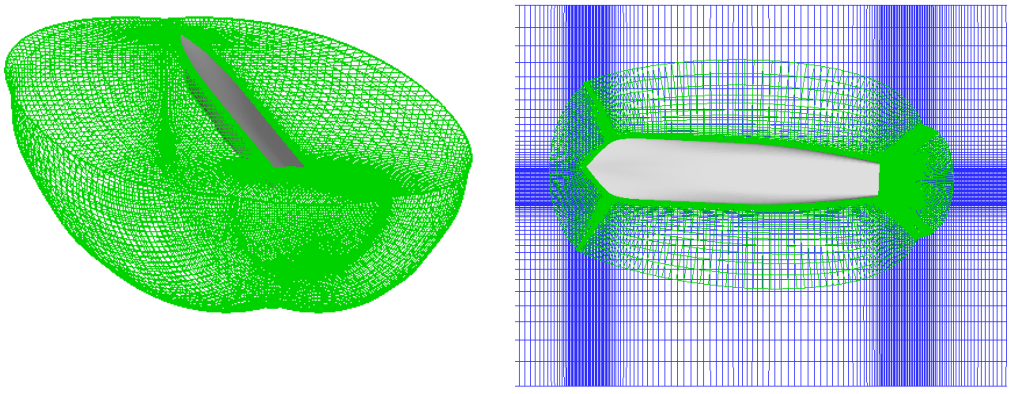

a) **b)**

Fig. 3.5. Computational Domain **a)** Body-fitted grid; **b)** Body-fitted grid (green) immersed in the background (blue). The body-fitted grid was mirrored respect to the z axis in order to create a deck on the hull.

The body-fitted grid was realized by extruding the hull surface mesh in the direction specified by the application of the proper boundary conditions to the hull sides. The first marching step was set to $y = 1 \cdot 10^{-5}$ so that $y^+ < 1$ for the highest Reynolds number case, so that the same grid can be used for all cases. Finally a growth rate of 1.1 was used for a total number of 65 marching steps.

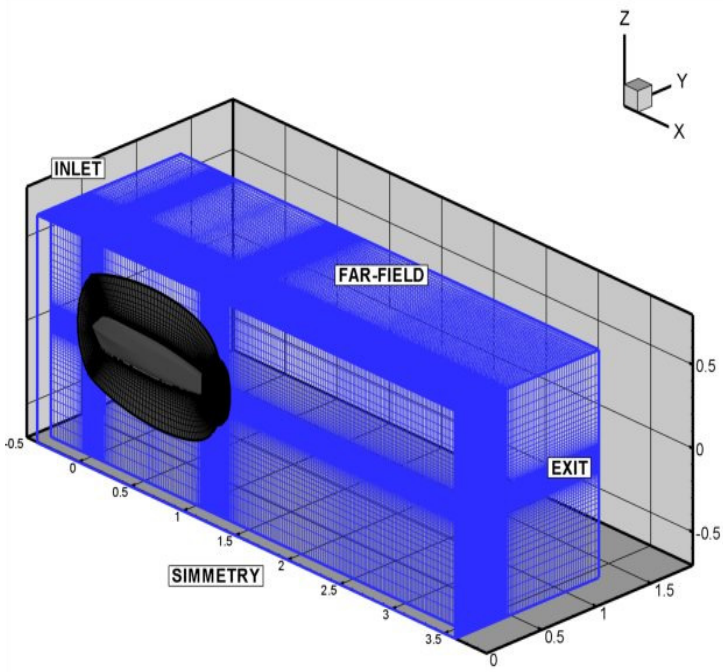

Fig. 3.6 Overall computational domain

The background grid extends in the range $-0.5 \leq x \leq 3.5$, $0 \leq y \leq 1.3$, $-0.65 \leq z \leq 0.65$, where x, y and z are non-dimensional coordinates (normalized by ship length, L_{PP}), the ship axis is aligned with x axis with the bow at x=0 and the stern at x=1 and the free surface, at rest, lies at z=0. The y axis corresponds to the symmetry axis between the two hulls. In the longitudinal direction the grid was realized to have at least 60 grid points for wavelength and this condition is satisfied for the range of wavelengths under consideration. In the vertical direction the grid was refined in correspondence of $-0.1 \leq z \leq 0.1$ allowing the calculation of larger and smaller amplitude waves. The grid was extended to cover the deck of the ship allowing calculations for high amplitude waves (Fig. 3.5 b).

To verify the mesh-independence condition of the solution, a medium and coarsen mesh were generated by coarsening the finer grid by $1/\sqrt{2}$ in each direction. The dimensions of the grids are summarized in Table 3.3:

Table 3.3. Summary of the grids used

	Fine	Medium	Coarse
Body Fitted 1	139x65x91	98x46x64	69x32x45
Body fitted 2	139x65x91	98x46x64	69x32x45
Background	309x139x88	218x98x62	154x69x44
Total	**5.424.058**	**1.901.592**	**666.264**

3.4 Initial and Boundary Conditions

A set of boundary conditions must be defined in order to carry out the computations. At inlet, a regular incoming wave $\zeta_I(x,t)$ of amplitude A and wavelength λ, is defined as:

$$\zeta_I(x,t) = A \cdot \cos[kx - 2\pi ft] \tag{3.6}$$

The wave velocity components in the directions x,y,z are U, V and W respectively:

$$U(x,y,z,t) = U_0 + \frac{A}{Fn}\sqrt{k}e^{kz}\cos[kx - 2\pi ft] \tag{3.7}$$

$$V(x,y,z,t) = 0 \tag{3.8}$$

$$W(x,y,z,t) = \frac{A}{Fn^2}\sqrt{k}e^{kz}\sin[kx - 2\pi ft] \tag{3.9}$$

Finally, the water pressure, p, is defined as:

$$p(x,y,z,t) = \frac{A}{Fn^2}e^{kz}\left\{\cos[kx - 2\pi ft] - \frac{1}{2}\frac{A}{k}e^{kz}\right\} \tag{3.10}$$

where $Fn = U/\sqrt{g \cdot L}$ is the Froude number, $k = 2\pi/\lambda$ is the wave number and $f = 1/\lambda + 1/\left(Fn\sqrt{2\pi\lambda}\right)$ is the non-dimensional encounter frequency.

The level-set function (§ 2.4.3) at the inlet is given by:

$$\phi(x_i,t) = \zeta(x_i,t) - z(x_i) \tag{3.11}$$

where x_i is the x-coordinate at the inlet.

Behind the ship and on the side of the computational domain, a zero-gradient boundary condition is applied for all the variables. On the top of the domain a zero-gradient pressure far-field boundary condition is imposed, while a zero pressure far-field boundary is used for the bottom. The problem solution allows the use of symmetry boundary condition for y=0 that corresponds to the center-plane between the two hulls. Finally on the ship a no-slip condition is imposed and at t=0, the ship is accelerated impulsively to full speed. The boundary conditions are summarized in Table (3.4):

Table 3.4. Summary of the boundary conditions

	ϕ	p	k	ω	U	V	W
Inlet (x=-0.5)	Eq(3.11)	Eq.(3.10)	$k_{fs}=10^{-7}$	$\omega_{fs}=9$	Eq.(3.7)	0	Eq.(3.9)
Exit (x=3.5)	$\frac{\partial\phi}{\partial n}=0$	$\frac{\partial p}{\partial n}=0$	$\frac{\partial k}{\partial n}=0$	$\frac{\partial\omega}{\partial n}=0$	$\frac{\partial^2 U}{\partial n^2}=0$	$\frac{\partial^2 V}{\partial n^2}=0$	$\frac{\partial^2 W}{\partial n^2}=0$
Far field (y=1.3)	$\frac{\partial\phi}{\partial n}=0$	$\frac{\partial p}{\partial n}=0$	$\frac{\partial k}{\partial n}=0$	$\frac{\partial\omega}{\partial n}=0$	$\frac{\partial U}{\partial n}=0$	$\frac{\partial V}{\partial n}=0$	$\frac{\partial W}{\partial n}=0$
Far field (z=0.65)	$\frac{\partial\phi}{\partial n}=1$	$\frac{\partial p}{\partial n}=0$	$\frac{\partial k}{\partial n}=0$	$\frac{\partial\omega}{\partial n}=0$	$U=1$	$V=0$	$W=0$
Simmetry (y=0)	$\frac{\partial\phi}{\partial n}=0$	$\frac{\partial p}{\partial n}=0$	$\frac{\partial k}{\partial n}=0$	$\frac{\partial\omega}{\partial n}=0$	$\frac{\partial U}{\partial n}=0$	$V=0$	$\frac{\partial W}{\partial n}=0$
Far field (z=zmax)	$\frac{\partial\phi}{\partial n}=-1$	**Not needed (air)**	$\frac{\partial k}{\partial n}=0$	$\frac{\partial\omega}{\partial n}=0$	$\frac{\partial U}{\partial n}=0$	$\frac{\partial V}{\partial n}=0$	$\frac{\partial W}{\partial n}=0$
No slip (ship wall)	$\frac{\partial\phi}{\partial n}=0$	**Pressure-Poisson Equation**	$k=0$	$\omega=\frac{60}{\mathrm{Re}\,\beta y^{+2}}$	$U=0$	$V=0$	$W=0$

3.5 Verification and Validation

To assess the quality of the computational results, a Verification and Validation study was conducted in the present work. Different approaches were proposed for estimating errors and uncertainties in CFD simulations but, for the time being, current methodology and procedure are not yet standardized. This work follows the methodology and procedures presented in Stern et al.[40] to determine simulation uncertainties and simulation errors.

Two sources of error are present in CFD simulations: modeling errors (δ_{SM}) and uncertainties (U_{SM}), due to assumptions and approximations in the mathematical representation of the physical problem, and numerical errors (δ_{SN}) and uncertainties (U_{SN}) due to the numerical solution of the mathematical equations. The simulation error, defined as the difference between the simulation results, S, and the truth, T, can be expressed as:

$$\delta_S = S - T = \delta_{SM} + \delta_{SN} \tag{3.12}$$

and the corresponding uncertainty equation is:

$$U_S^2 = U_{SM}^2 + U_{SN}^2 \tag{3.13}$$

Under certain conditions, the numerical error can be estimated as:

$$\delta_{SN} = \delta^*_{SN} + \varepsilon_{SN} \tag{3.14}$$

where δ^*_{SN} is an estimate of the sign and magnitude of δ_{SN} and ε_{SN} is the error in that estimate, hence the corrected simulation value is defined as:

$$S_C = S - \delta^*_{SN} \tag{3.15}$$

This yields the error equation:

$$\delta_{S_C} = S_C - T = \delta_{SM} + \varepsilon_{SN} \tag{3.16}$$

and the corresponding uncertainty equation:

$$U^2_{S_C} = U^2_{SM} + U^2_{S_C N} \tag{3.17}$$

where U_{S_C} is the uncertainty in the corrected simulation and $U_{S_C N}$ is the uncertainty in estimate for ε_{SN}.

Verification is defined as a process of assessing numerical uncertainty U_{SN} and of estimating the sign and magnitude of δ^*_{SN} of the simulation numerical error and the uncertainty in that error estimate. Numerical error is due to iteration number (δ_I), time step (δ_t), grid size (δ_G) and other parameters (δ_P). Therefore numerical error and uncertainty are expressed as:

$$\delta_{SN} = \delta_I + \delta_G + \delta_t + \delta_P = \delta_I + \sum_{j=1}^{J} \delta_j \tag{3.18}$$

$$U^2_{SN} = U^2_I + U^2_G + U^2_t + U^2_P = U^2_I + \sum_{j=1}^{J} U^2_j \tag{3.19}$$

A better approximation of the error and uncertainty can be obtained from the corrected approach:

$$\delta^*_{SN} = \delta^*_I + \delta^*_G + \delta^*_t + \delta^*_P = \delta^*_I + \sum_{j=1}^{J} \delta^*_j \tag{3.20}$$

In this case the corrected simulation value and corrected simulation numerical uncertainty are given by

$$S_C = S - \left(\delta_I^* + \sum_{j=1}^{J} \delta_j^* \right) \tag{3.21}$$

$$U_{S_C N}^2 = U_{I_C}^2 + \sum_{j=1}^{J} U_{j\,C}^2 \tag{3.22}$$

To calculate each term of Eq.(3.18) or Eq.(3.20), convergence studies must be conducted using multiple (m) solutions with systematic parameter refinement by varying the kth input parameter Δx_k while all other parameters are kept constant. Usually $m \geq 3$, since $m = 2$, i.e. two solutions, only indicates sensitivity but not convergence. Many common input parameters of this kind, on the previous considerations, are grid spacing or time step. Usually, the refinement ratio between solutions, defined as $r_k = \Delta x_{km} / \Delta x_{k_{m-1}}$ is assumed to be constant, but not required. Generally speaking, small values of r_k are undesirable since solution changes will be small and sensitivity to input parameters is difficult to identify compared to iterative errors. On the other side, with large values of r_k the finest step size could be too small if the coarsest step is designed to have a sufficient resolution. A good compromise is identified in using a refinement ratio $r_k = \sqrt{2}$.

For the k^{th} parameter and the m^{th} solution, Eq(3.21) can be written as:

$$S_{k_m} = S_C + \delta_{I_{km}}^* + \delta_{k_m}^* + \sum_{j=1; j \neq k}^{f} \delta_{j_m}^* \tag{3.23}$$

Iterative convergence must be assessed and is evaluated by the solution residuals. Three or four orders of magnitude drop in solution residual to a level of 10^{-4} is desirable. Methods for estimating iterative errors and uncertainty are described in [40], but in many cases these errors are considered negligible in comparison with other sources of error.

Hence for m^{th} solution we can write the following equation:

$$\hat{S}_{k_m} = S_{k_m} - \delta_{I_{km}}^* \tag{3.24}$$

Considering three solutions where $\hat{S}_{k1}$ corresponds to the finest solution, $\hat{S}_{k2}$ to the medium solution and $\hat{S}_{k3}$ to the coarse one for the k^{th} parameter, we can calculate the solution changes and their ratio as:

$$\varepsilon_{k_{21}} = \hat{S}_{k_2} - \hat{S}_{k_1} \tag{3.25}$$

$$\varepsilon_{k_{32}} = \hat{S}_{k_3} - \hat{S}_{k_2} \tag{3.26}$$

$$R_k = \frac{\varepsilon_{k_{21}}}{\varepsilon_{k_{32}}} \tag{3.27}$$

Three convergence conditions are possible:

$$0 < R_k < 1 \text{ Monotonic convergence}$$
$$R_k < 0^1 \text{ Oscillatory convergence}$$
$$R_k > 1 \text{ Divergence}$$

For monotonic convergence the generalized Richardson extrapolation (RE) is used to estimate U_k or δ_k^* and U_{kc}. In more detail, the following equations are used for δ_k^* and the order of accuracy p_k to estimate the leading order term of a finite sum that describes the error:

$$\delta_k^* = \delta_{RE_k}^* = \frac{\varepsilon_{k_{21}}}{r_k^{p_k} - 1} \tag{3.28}$$

$$p_k = \frac{\ln(\varepsilon_{k_{32}} / \varepsilon_{k_{21}})}{\ln(r_k)} \tag{3.29}$$

To account for the effects of higher order terms, a correction factor C_k is introduced:

$$\delta_k^* = C_k \delta_{RE_k}^* = C_k \left(\frac{\varepsilon_{k_{21}}}{r_k^{p_k} - 1} \right) \tag{3.30}$$

where C_k is defined as:

$$C_k = \frac{r_k^{p_k} - 1}{r_k^{p_{kest}} - 1} \tag{3.31}$$

and p_{kest} is an improved estimate of p_k. If solutions are in the asymptotic range ($C_k \to 1$), the correction as expressed in Eq.(3.31) is not needed and Eq.(3.30) reduces to Eq.(3.28). In this case δ_k^* and U_{k_c} are estimated, as the uncertainty in the error estimate is based on the amount of correction according to the following:

$$U_{k_c} = \left| (1 - C_k) \delta_{RE_{k1}}^* \right| \tag{3.32}$$

For solutions outside the asymptotic range (C_k<1 or C_k>1), only the magnitude of the error is estimated through the uncertainty U_k:

$$U_k = \left|C_k \delta^*_{RE_k}\right| + \left|(1 - C_k)\delta^*_{RE_k}\right| \tag{3.33}$$

A detailed description of the procedure, including also oscillatory convergence, can be found in [40].

Validation is the process for assessing modeling uncertainty U_{SM} by using benchmark experimental data and for estimating the sign and magnitude of δ_{SM}. Hence, errors and uncertainties in the experimental data must be considered.

The comparison error is defined as:

$$E = D - S = \delta_D - \delta_S \tag{3.34}$$

and is the sum of all the errors associated both with the experimental data and the simulations. We can define the validation uncertainty U_V as the combination of all uncertainties that is :

$$U_V^2 = U_D^2 + U_{SN}^2 + U_{SPD}^2 \tag{3.35}$$

where U_{SPD} is the uncertainty relative to previous data as fluid properties. If $|E|$ is less than the validation uncertainty U_V, the combination of all the errors in data and numerical simulations is smaller than the estimated validation uncertainty and validation has been achieved at the U_V level. If there is a programmatic validation requirement, there is another uncertainty that must be considered U_{reqd}, since validation is required at that uncertainty level or below. Different conditions are possible:

$$\begin{aligned}
&1.\ |E| < U_V < U_{reqd} \\
&2.\ |E| < U_{reqd} < U_V \\
&3.\ U_{reqd} < |E| < U_V \\
&4.\ U_V < |E| < U_{reqd} \\
&5.\ U_V < U_{reqd} < |E| \\
&6.\ U_{reqd} < U_V < |E|
\end{aligned} \tag{3.36}$$

In cases 1, 2 and 3 validation is achieved at the U_V level and in case 1 validation is achieved at a level below U_{reqd} so validation is successful from a programmatic standpoint, but attempting to estimate δ_{SMA} is not feasible from

an uncertainty point of view. In cases 4, 5 and 6 the comparison error is above the noise level ($U_V < |E|$) and using the sign and magnitude of E to estimate δ_{SMA} is feasible from an uncertainty standpoint.

Convergence studies for grid spacing and time step were undertaken in this work to assess numerical errors. The resonant physical conditions have been chosen as test case for the large ship motions and accelerations that result to be the worst-case test (Fn=0.75; λ/L_{pp}=1.806, Ak=0.025). For the grid study, 117 time steps ($\Delta t = 0.009$) per wave period were used to obtain solutions on the fine, medium and coarse grids as in Table (3.3).

For the time step study, the finest grid was used to obtain solutions for three time steps having refinement ratio of $\sqrt{2}$ and at least 80 time steps per wave period, according to Table 3.5:

Table 3.5 Summary of the V&V test conditions

Grid	Time step		
	Fine	Medium	Coarse
Fine	**(167 time steps/wave period)**	**(117 time steps/wave period)**	**(83 time steps/wave period)**
Medium		Medium	
Coarse		Medium	

The verification parameters include the first harmonic component of heave and pitch motions.

Chapter 4

Computational Results for the DELFT Catamaran

4.1 Introduction

The DELFT catamaran advancing in regular head waves is analyzed numerically with the Unsteady RANS Code CFDShip-Iowa V.4, according to the conditions described in Chapter 3.

The main focus of the present work is to investigate the maximum response conditions, in terms of ship motions, for the catamaran and the factors which affect maximum response. Previous studies for monohulls [15] show that pitch and heave motions can be explained in analogy to a mass-spring-damper system with forced motions according to the following equation:

$$m\ddot{x}_i(t) + b\dot{x}_i(t) + cx_i(t) = f(t) \tag{4.1}$$

where $x_i(t)$ is the response variable, for instance heave motion, m is the mass of the ship and the added mass in heave, b is the damping coefficient caused by wave radiation due to heave oscillations and other damping contributions, c is the spring coefficient and $f(t)$ is the excitating force. If $f(t)$ is zero, Eq.(4.1) describes the free oscillations and the natural pulsation can be calculated with the following expression:

$$\omega_n = \frac{1}{2m}\sqrt{4mc - b^2} \tag{4.2}$$

If $f(t)$ is a in continuous non transient wave loading, we can express it as $F_0 \cos \omega t$ and the general solution of Eq.(4.1) is the sum of the homogeneous solution, y_h, and the particular solution y_p, that oscillate at different frequencies until y_h is damped out and only the effects of y_p remain in the steady state

solution. By introducing the geometric ship parameters in the expressions of *m*, *b* and *c*, the natural pulsation for heave and pitch can be evaluated as:

$$\omega_3 = \sqrt{\frac{C_{33}}{m + A_{33}}} \tag{4.3}$$

$$\omega_5 = \sqrt{\frac{C_{55}}{I_{55} + A_{55}}} \tag{4.4}$$

where, A_{55} and A_{33} are respectively the pitch added momentum of inertia and heave added mass and $C_{33} = \rho g A_W$, $C_{55} = \rho g I_T$. The assumptions that $A_{55} \approx I_{55}$ and $A_{33} \approx m$ are commonly used and introducing the expressions of C_{33} and C_{55} as functions of hull geometric parameters, the ship natural frequency can be expressed as follows:

$$f_n = \sqrt{\frac{g C_{WP}}{8\pi^2 C_B T}} \tag{4.5}$$

in which C_{wp} is calculated as $C_{WP} = A_W / (B \cdot L_{PP})$, where A_w is the waterplane area of the hull, B is the beam of the ship and L_{PP} is the length between perpendiculars of the ship.

One of the main factors that affect ship response to incoming wave loads is resonance that occurs when the ship is excited with an encounter frequency equal or close to the ship natural frequency, f_n:

$$f_e = \sqrt{\frac{g}{2\pi\lambda}} + \frac{U_0}{\lambda} \tag{4.6}$$

where U_0 is the ship speed, g is the gravity acceleration and λ is the length of the incoming wave. According to literature, ship response to incoming wave loads is affected not by resonance only, but also by wavelenght and is maximum for $\lambda / L_{PP} \approx 1.33$ [15]. Based on the above considerations, Irvine et al.(2008) suggest that if both conditions (f_e=f_n and λ/L_{pp}=1.33) hold, then the ship speed where maximum response should occur, can be derived by combining Eq (4.6) and $\lambda / L_{PP} \approx 1.33$. This gives a simple formulation in terms of Froude number:

$$Fn_{\max,res} = 1.33\left(\sqrt{\frac{L_{PP}}{g}} f_n - \sqrt{\frac{3}{8\pi}}\right) \tag{4.7}$$

where f_n is the natural frequency for heave and pitch according to Eqs. (4.3)

and (4.4) and with the assumptions that $A_{55} \approx I_{55}$ and $A_{33} \approx m$.

The following paragraphs will report the investigation results on a number of questions.

First of all, paragraph 4.3 will discuss the ship motions and, in particular, whether the maximum response condition, which was derived for a monohull, can be extended to multihulls.

Secondly, paragraph 4.4 will discuss the ship response to the wave steepness and the validity of the linearity hypothesis. The linear theory, in fact, implies that the wave-induced motion amplitude is proportional to the incoming wave amplitude and a useful consequence is that motions in irregular waves, considered as sum of different amplitudes phases and directions waves, can be simply obtained by adding together the contributions of each wave. Whether the validity of the linear theory depends on wave steepness will be discussed.

Finally in paragraph 4.5 the results on ship resistance both in calm water and in the presence of waves will be presented. Results point out the presence of a new component of resistance in waves due to the interaction between incident waves and the ship.

4.2 DELFT Catamaran natural frequency

The expression developed for monohulls (Eq.4.5) is used and was extended to twin hulls in order to calculate the natural frequency of the DELFT catamaran, that is a fundamental parameter for evaluation of ship response to waves. To this purpose, data relative to twin hulls were introduced. For instance, A_w is referred to the area of both hulls, B is the beam overall and not the demihull beam, and C_B is the block coefficient relative to the catamaran and not to demihull. The natural frequency for heave and pitch motions resulted approximately $f_n=1.19$ *Hz*.

To examine the validity of Eq.(4.5) extension to multihull vessels, the natural frequency of the DELFT catamaran was calculated by simulating the condition of the ship advancing in calm water with no damping and by studying the transient state before the final steady sinkage and trim are reached (Fig.4.1). Three speeds were considered (Fn=0.45, 0.6, 0.75) in the calculations and simulation results are shown in Table4.1:

Table 4.1 Heave and pitch natural frequency as a function of ship speed (in terms of Froude number Fn).

Fn	Natural frequency (Hz) *Heave*	Natural frequency (Hz) *Pitch*
0.45	1.32	1.32
0.6	1.30	1.30
0.75	1.28	1.28

The results show that the effects of Froude number on natural frequency are negligible, in accordance with Eq. (4.5) and that the average value of f_n=1.3 Hz can be considered a fairly good estimate of the catamaran natural frequency, in quite good agreement with the calculated one (f_n=1.19 Hz). Fig.4.1a) presents the transient heave and pitch motions for Fn=0.6 and the corresponding FFT analysis (Fig.4.1b) shows that the peak of the first harmonic occurs at the same frequency for both motions.

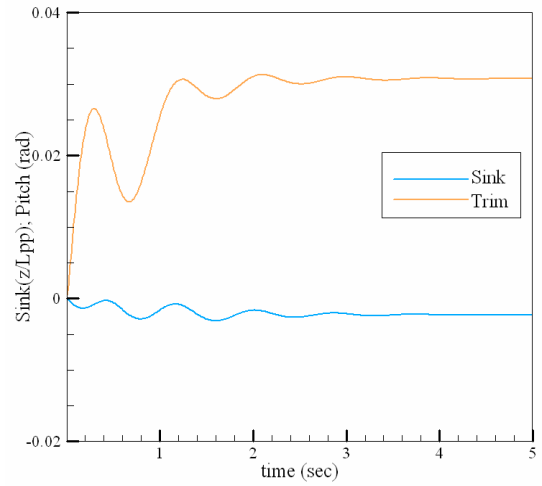

a)

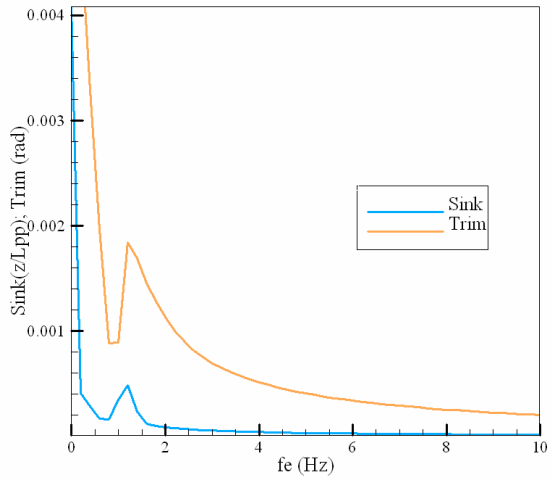

b)

Fig.4.1. Response in terms of sinkage and trim of the catamaran advancing at constant speed and free to oscillate **a)**Time history of ship motion amplitudes non-dimensionalized by ship length. The catamaran undergoes a transient state during which oscillates at its natural frequency and reaches the final steady sinkage and trim values. **b)** Transient heave and pitch responses FFT analysis as a function of encounter frequency. The peaks at fe=0 are the zero-order harmonic amplitudes motions, the next peaks correspond to first harmonic amplitudes of motions and both occur at fe=1.3Hz, which corresponds to the catamaran natural frequency.

4.3 Ship motions

The behavior a ship advancing at fixed speed in waves is usually evaluated in terms of ship motion in response to incoming wave's amplitude and length. The catamaran movement was simulated under the sea conditions which are described in Section 3.2 and summarized in table 3.2 and which correspond to realistic operative ranges for existing catamarans. As experimental data are available in terms of amplitudes and phases of heave and pitch motions, an FFT analysis of the simulated times histories was carried out.

A first result within the time domain is show in fig.4.2.

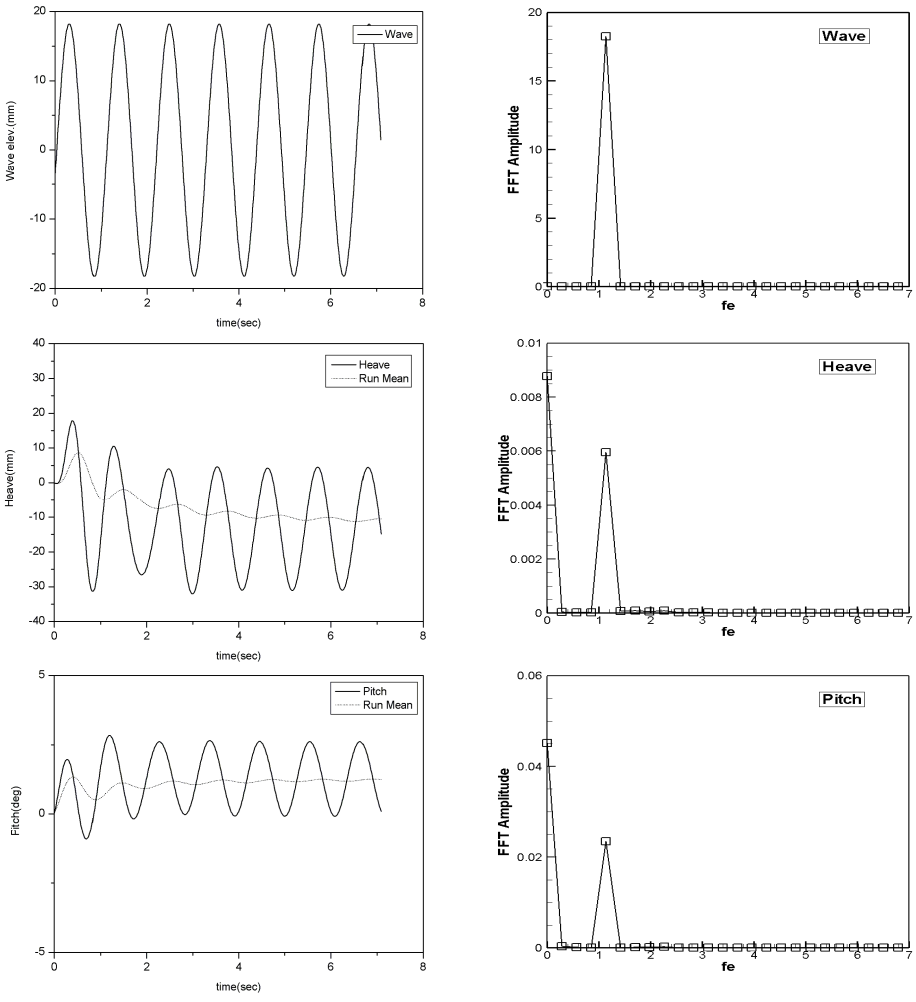

a) **b)**

Fig.4.2. Fn=0.45 λ/L_{pp}=1.991 **a)**Wave time history for wave and resulting heave and pitch responses. The heave and pitch running means are also shown **b)**FFT Analysis of ship responses that shows how responses are characterized by the zero harmonic at the first peak (fe=0) and first harmonic component at the following peak that occurs at the same frequency as the incoming wave. No other components of ship response are registered.

The vessel response is characterized only by the zero and first harmonic components of Eq.(3.2) and Eq.(3.3). In fact, the vessel position oscillates at the same frequency as the exciting wave load. Hence the motions are described by means of the transfer functions, also called response amplitude operators (RAO), which for heave and pitch are defined by Eq.(3.4) and Eq.(3.5), and by means of the corresponding phases. Therefore, the ship response was analyzed first of all in terms of first harmonic.

First harmonic simulation results and experimental data are compared in figures 4.3, 4.4 and 4.5 for different Froude numbers (Fn=0.45, 0.6 and 0.75).

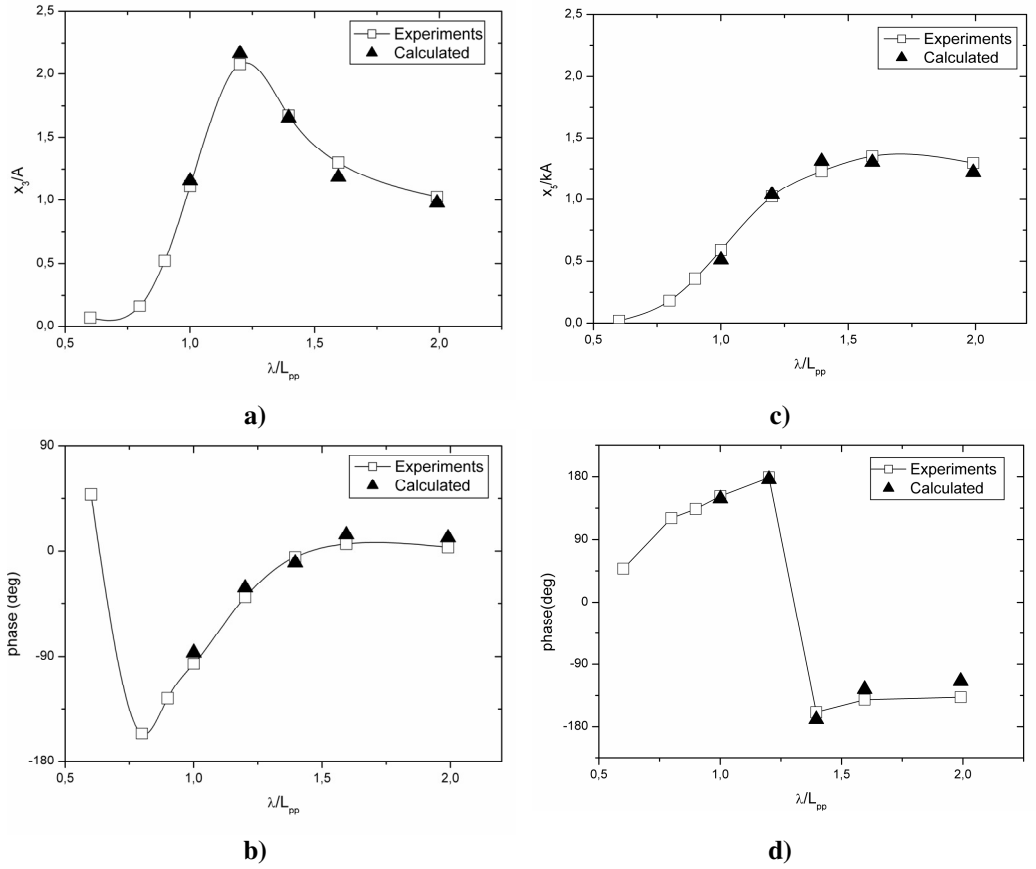

Fig.4.3. Heave and picth motions as a function of the incoming wave wavelength (λ/L_{PP}) for Fn=0.45. Results are presented in terms of first harmonic amplitudes and phases:**a)**Heave amplitude x_3 non-dimensionalized by wave amplitude A; **b)** Heave phase; **c)** Pitch Amplitude x_5 non-dimensionalized by kA, k wave number; **d)** Pitch phase (degrees).

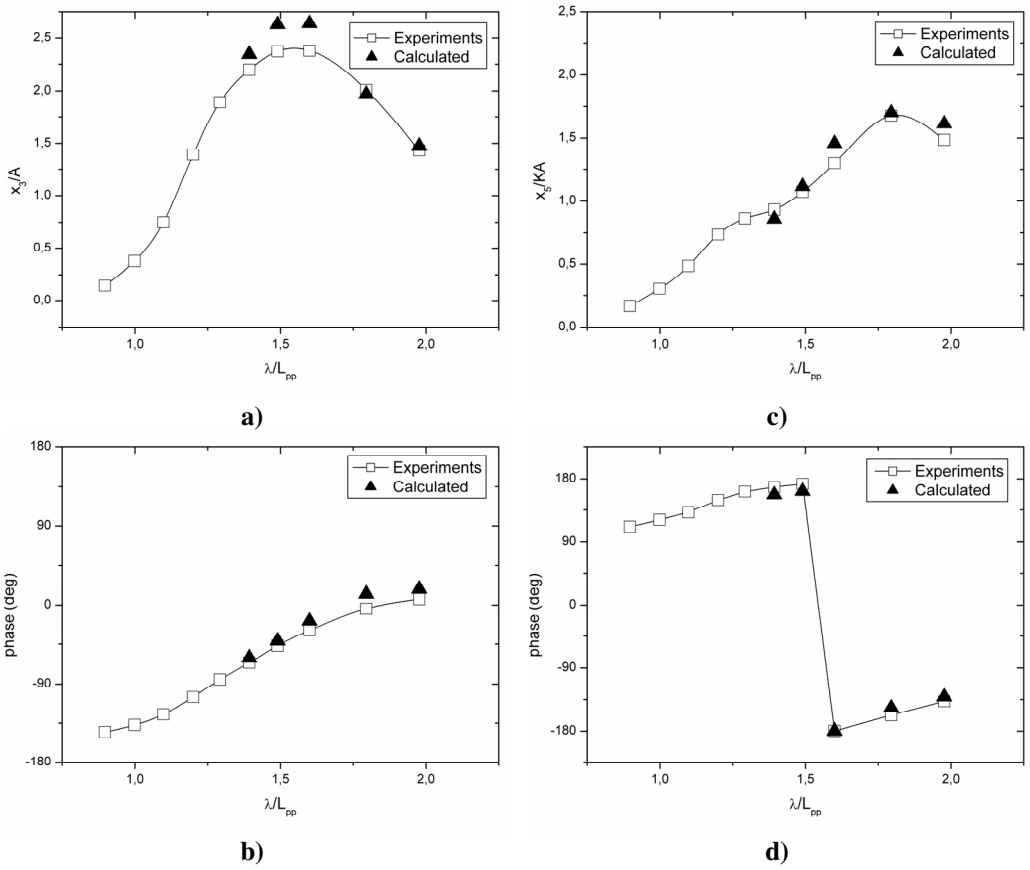

Fig.4.4. Heave and picth motions as a function of the incoming wave wavelength (λ/L_{PP}) for Fn=0.6. Results are presented in terms of first harmonic amplitudes and phases:**a)**Heave amplitude x_3 non-dimensionalized by wave amplitude A; **b)** Heave phase; **c)** Pitch Amplitude x_5 non-dimensionalized by kA, k wave number; **d)** Pitch phase (degrees).

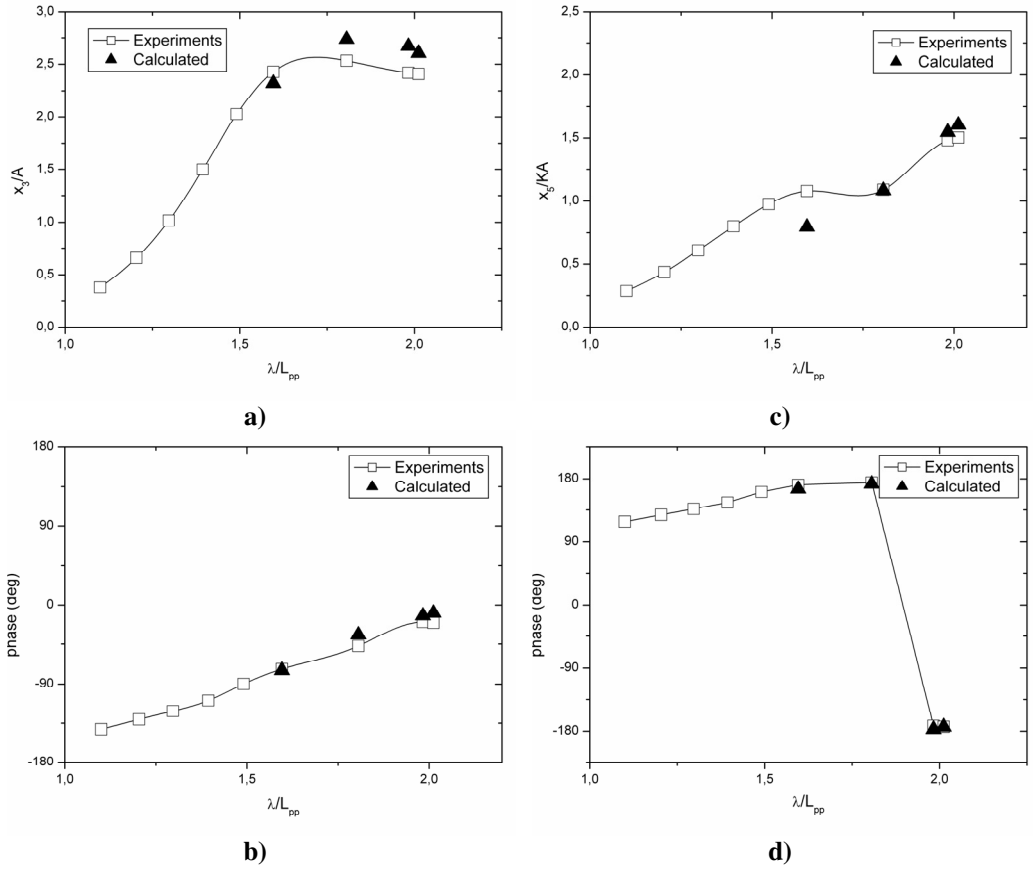

Fig.4.5. Heave and picth motions as a function of the incoming wave wavelength (λ/L_{PP}) for Fn=0.75. Results are presented in terms of first harmonic amplitudes and phases:**a)**Heave amplitude x_3 non-dimensionalized by wave amplitude A; **b)** Heave phase; **c)** Pitch Amplitude x_5 non-dimensionalized by kA, k wave number; **d)** Pitch phase (degrees).

The overall motions characteristics are properly predicted both in amplitude and phase, with a 1-10% disagreement. In more detail, the expected responses to short and long wavelengths are obtained. For instance, at Fn =0.45 the transfer functions TF_{x3} (Fig.4.3.a) and TF_{x5} (Fig.4.3.c) approach the unity as λ increases, while the heave phase (Fig.4.3.b) goes to zero, thus indicating that the heave motion becomes synchronized with the incoming waves. On the contrary, the pitch phase approaches -90 degrees (Fig.4.3.d) and hence maximum positive pitch is registered one quarter of an encounter period after the wave trough has passed amidship. For lower wavelengths λ, TF_{x3} and TF_{x5} decrease towards zero (Fig.4.3a and 4.3c), that is, the ship does not follow the head waves but tends to cut them and pass through them. Similar trends are predicted by the code at higher Froud numbers (Fn=0.6 and Fn=0.75), (Figs.4.3 and 4.4). At these higher velocities, however, there is a lack of experimental results at the higher wave lengths and not enough data are available to fully define the phase.

The first harmonic analysis was then used to investigate the conditions that determine the maximum ship response. The results for heave and pitch motions are plotted as functions of the encounter frequency (*fe*) and of the wave length (λ/L_{pp}) in Figures 4.6 and 4.7.

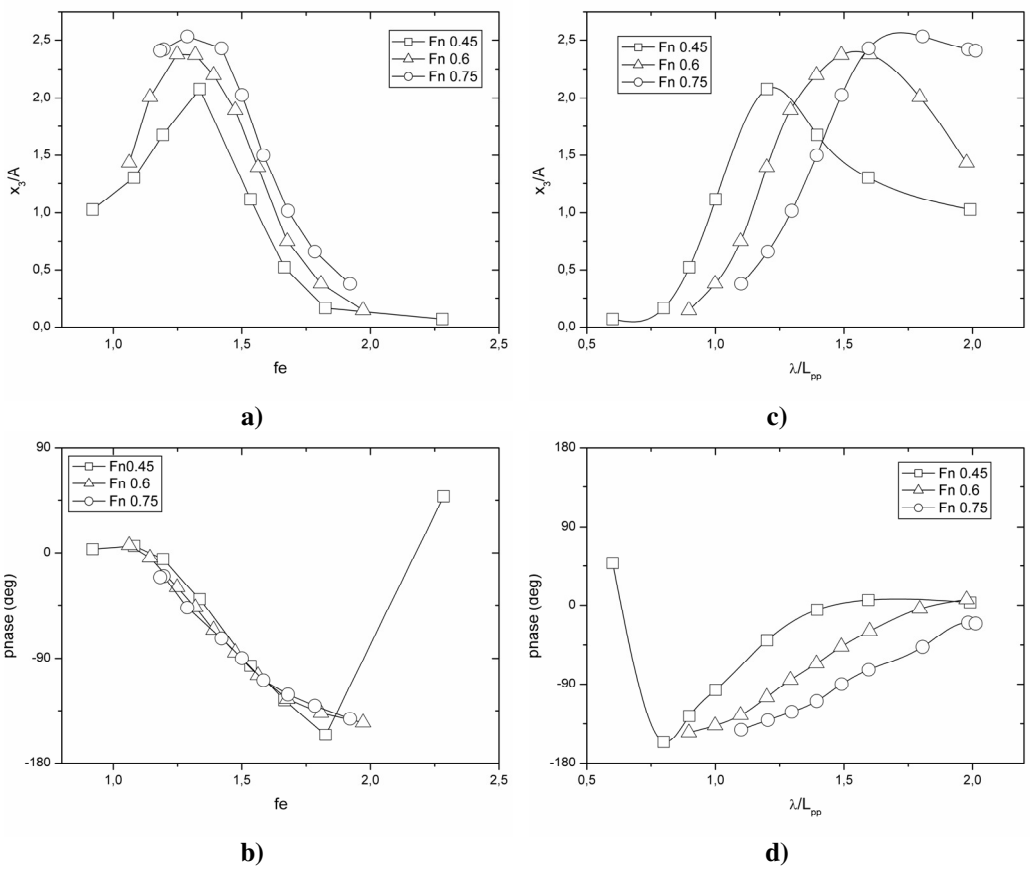

Fig.4.6. Heave motion experimental results for Fn=0.45,0.6 and 0.75: **a)** Amplitude x_3/A as function of fe (encounter frequency); **b)** Phase (degrees) as function of fe; **c)** Amplitude x_3/A as function of λ/L_{pp}; **d)** Phase (degrees) as function of λ/L_{pp}.

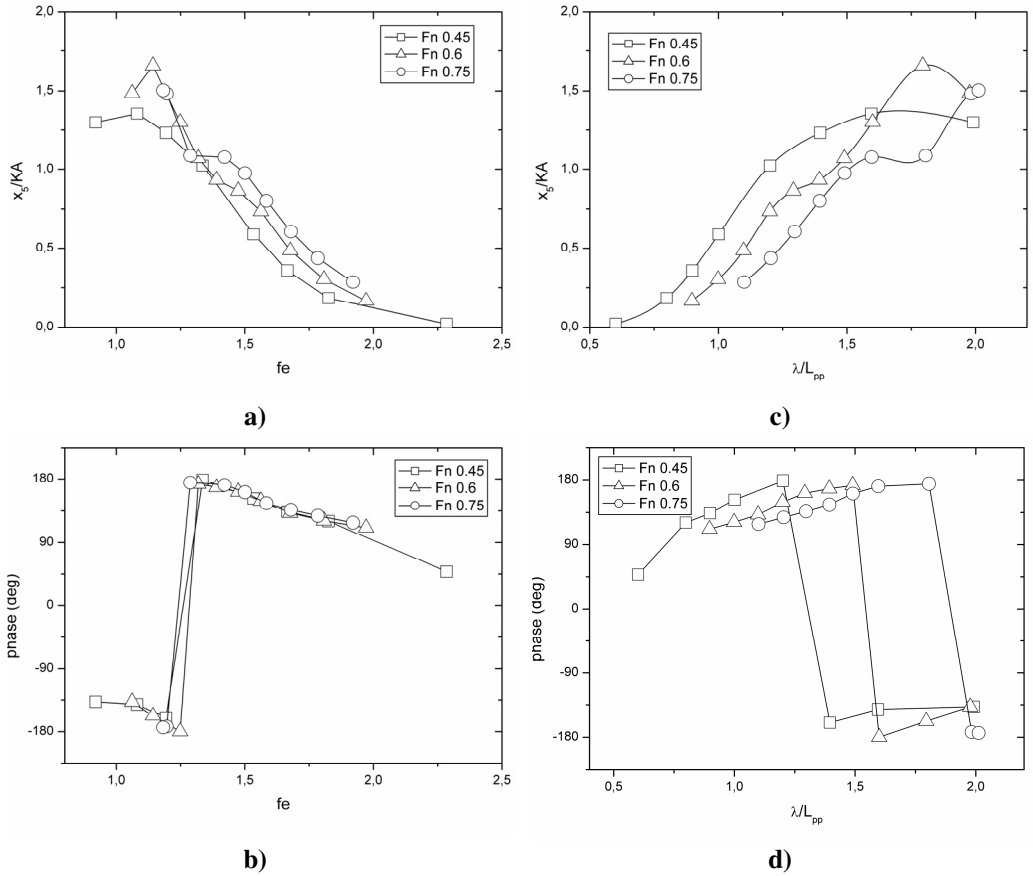

Fig.4.7. Pitch motion experimental results for for Fn=0.45,0.6 and 0.75: **a)** Amplitude x_5/kA as function of fe (encounter frequency); **b)** Phase (degrees) as function of fe; **c)** Amplitude x_5/kA as function of λ/L_{pp}; **d)** Phase (degrees) as function of λ/L_{pp}

Starting with heave motion (Fig.4.6.a) it can be observed that for all three speeds, the maximum response occurs at resonance (f_e=1.3 Hz), and that the response increases with speed so that global maximum occurs at Fn=0.75. Hence, it seems that only resonance frequency affects the maximum response and there is no or negligible effect of the exciting load of different wavelength. This can be better illustrated by plotting the same TF_{x3} as functions of wavelength as in Fig.4.6.c) where, for each speed, the maximum is not registered in correspondence of $\lambda/L_{PP} \approx 1.33$ as expected, but exactly for the wavelength which corresponds to the resonance frequency. This different behavior between catamaran and mono-hulls may be due to the range of Froude numbers under study, that are considerably higher than the values found in Irvine [15] where the maximum tested ship speed corresponded to Fn=0.41. However, this different behavior may be also due to ship geometry (twin-hull), which determines the interference effects between hulls. As for pitch motion, it can be observed in Fig. 4.7.a) that the maximum response for the three different speeds occurs for frequencies below the resonance value and the global maximum occurs at Fn=0.6 and f_e=1.14 Hz and not for the highest speed as for heave. Furthermore, looking at Fig.4.7c where the same parameter is plotted versus wavelength, the maximum response occurs at Fn=0.6 for $\lambda/L_{PP} \approx 1.8$, that is in accordance with the results found in Simonsen for pitch motion [39]. However, in the case of the pitch motion, the effects of the higher wavelength exciting loads on maximum response are more relevant than in the case of the heave motions. More work is however needed in order to better quantify these effects.

Figures from 4.3 to 4.7 have shown the vessel behavior in terms of maximum response. A more detailed description of the periodic wave pattern, which consists of the interaction between the incoming wave and the waves generated by the ship is given by Fig. 4.8. Simulated conditions are Fn=0.45 and λ/L_{pp}=1.001. The surface elevation is plotted at each quarter of a period in fig. 4.8(a-c-e-g). Corresponding ship motions are plotted in Fig.4.8(b-d-f-h), where z=0 is the reference level corresponding to the free surface in calm water. Results are displayed for demi-hull because a symmetry boundary condition has been applied at y=0. In Fig. 4.8(a-c-e-g) it can be observed that between the two hulls, wave crests and troughs are more pronounced because of the interference in the inner region of the wave patterns generated by both hulls. At t/T=0 the ship advances towards a wave crest and the bow starts to come out of the water as time approaches t/T=1/4. At this time it can be observed that the ship reaches the wave crest and the hull keeps going out from water with higher angle that reaches its maximum at t/T=1/2. Here the ship reaches the wave trough and starts to dive into water with a low rotation angle (t/T=3/4). At t/T=1 the periodic behavior is reached and the wave pattern and ship motions are similar to t/T=0.

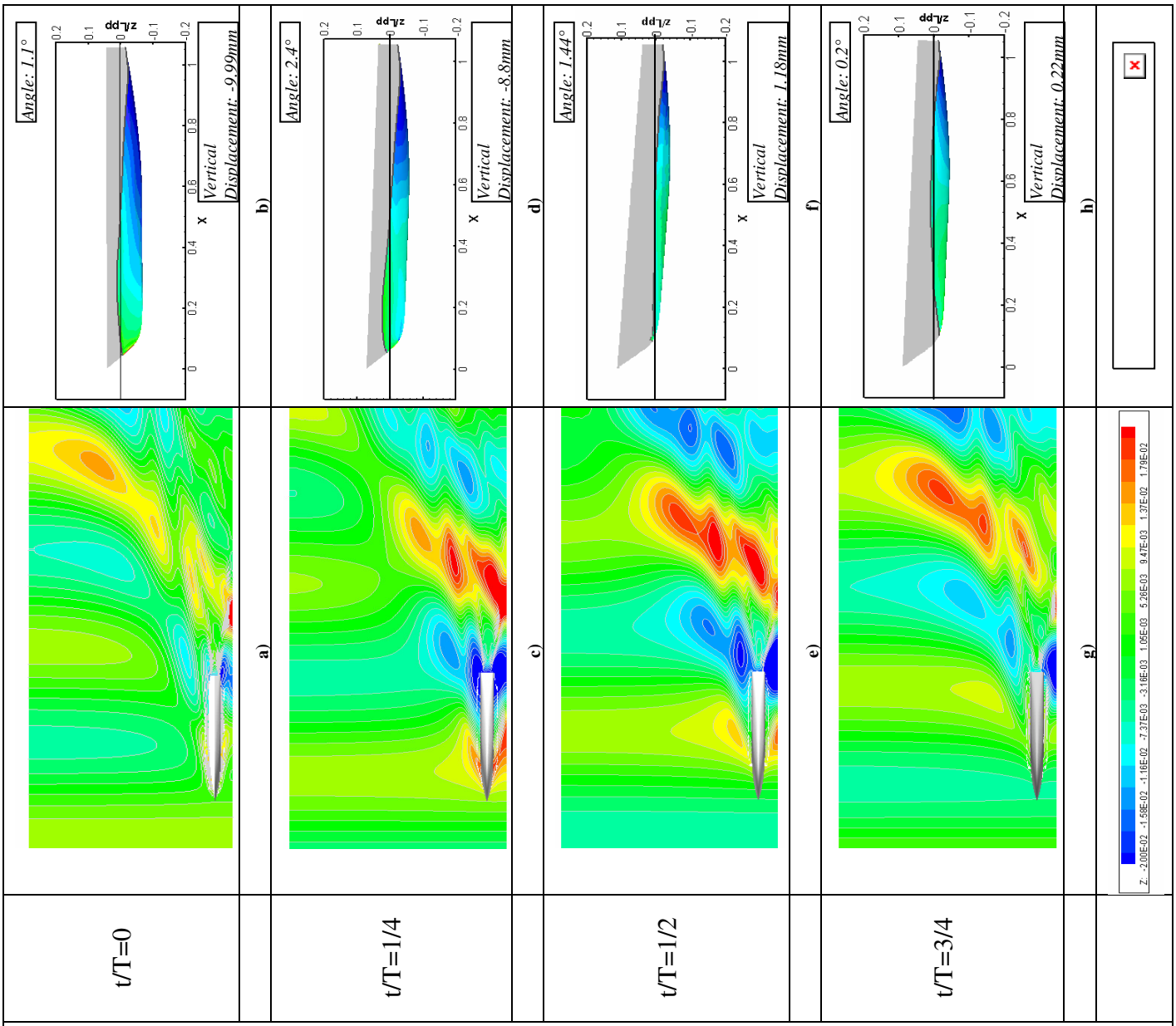

Fig.4.8 Fn=0.45 λ/Lpp=1.001 **Left:** Surface elevation non-dimensionalized with ship length at t/T=0,1/4,1/2,3/4. **Right**: Corresponding ship motions with pressure distribution on the wetted area. At t/T=0 a wave crest advances towards the bow(a) and the ship starts to move upward as time approaches t/T=1/4(d). Here the crest reaches the bow (c-d) and the ship rides highly with a maximum rotation angle at t/T=1/2(e-f). At this time a trough reaches the bow(g) and the ship moves downwards with less rotation angle at t/T=3/4(h). At t/T=1 the periodic behavior is reached.

In summary the catamaran exhibits the following behavior in response to the wave frequency:

I. For wavelengths sensibly higher than the vessel length (low wave frequency, f_e<1), heave tends to be synchronized with the head wave, while a phase lag is observed for pitch;
II. For wavelengths equal or moderately higher than the vessel length (1< f_e<1.5) a maximum is observed both for heave and pitch motions with amplitudes higher than the incoming wave, because of the effects of resonance;
III. For wavelengths significantly shorter than the vessel length (f_e>1.5) the motions tend towards zero; the ship do not follow the head waves but cuts them and pass through them.

4.4 Effects of wave steepness on ship response

The assumption of linear response of ship motions with wave amplitude is usually made in seakeeping studies. This approach is very useful because the more realistic motions in irregular waves can be represented by the superposition of the different facets of the wave-body interaction in regular waves. However, this assumption requires sufficiently small wave amplitudes to justify linearization. An important parameter that takes into account the effects of the wave amplitude on ship response is the wave steepness (Ak), where A is the wave amplitude and $k = 2\pi/\lambda$ is the wave number. Therefore, in order to evaluate the range of steepness in which a linear behavior of the catamaran can be assumed, simulations were carried out for different steep waves. In particular, the simulations were carried out for Fn=0.75, where maximum response occurs, at the steepness values of 0.025, 0.05 and 0.1 (Table 4.2).

Table 4.2. Test matrix for the evaluation of steepness effects on ship motions

Fn	Steepness	λ/L_{pp}
0.75	0.025	1.596-1.806-1.983-2.012
0.75	0.05	1.596-1.806-1.983-2.012
0.75	0.1	1.596-1.806-1.983-2.012

Results are shown in Fig.4.9 and Fig.4.10, where the first harmonics of heave and pitch motions are plotted as a function of the wavelength and as a function of the incoming wave amplitude, A, respectively:

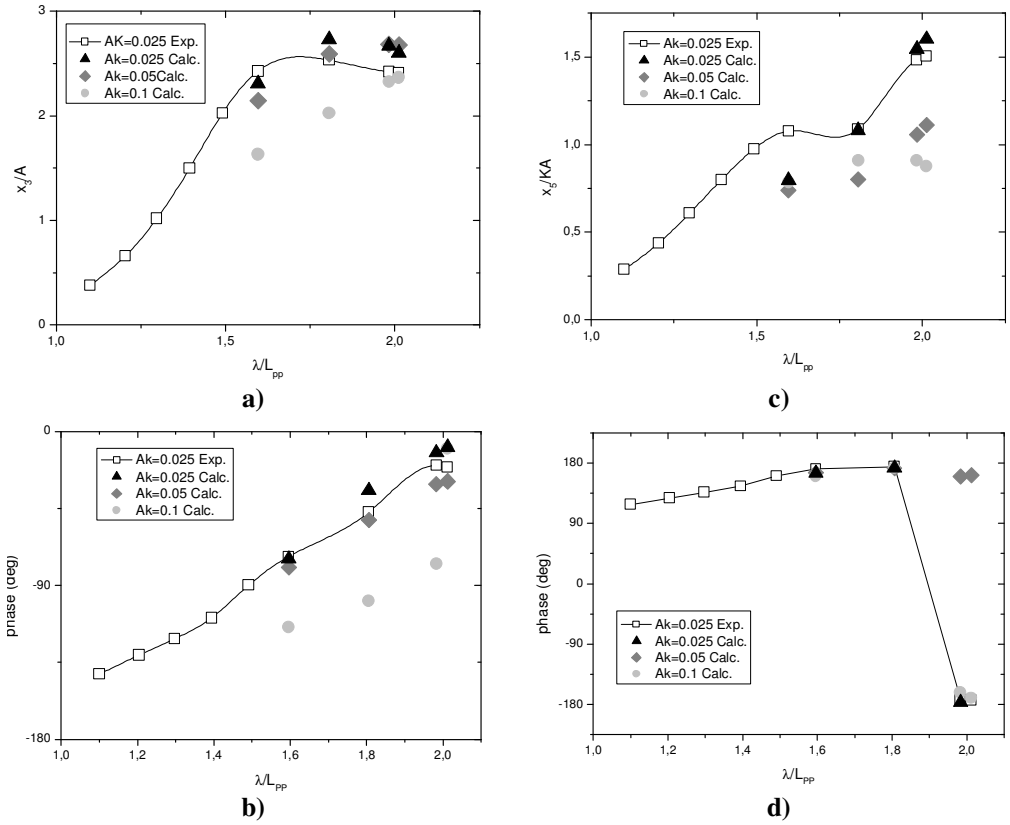

Fig.4.9. Computational results for estimating the effects of wave steepness on ship response for Fn=0.75. Three steepness values are considered: Ak=0.025,0.05,0.01 .Experimental data available only for Ak=0.025 are also plotted. **a)** Heave Amplitude x_3/A as function of λ/L_{pp}; **b**)Heave phase in degrees as function of λ/L_{pp}; **c**)Pitch Amplitude x_5/KA function of λ/L_{pp}; **d**)Pitch phase in degrees as function of λ/L_{pp}.

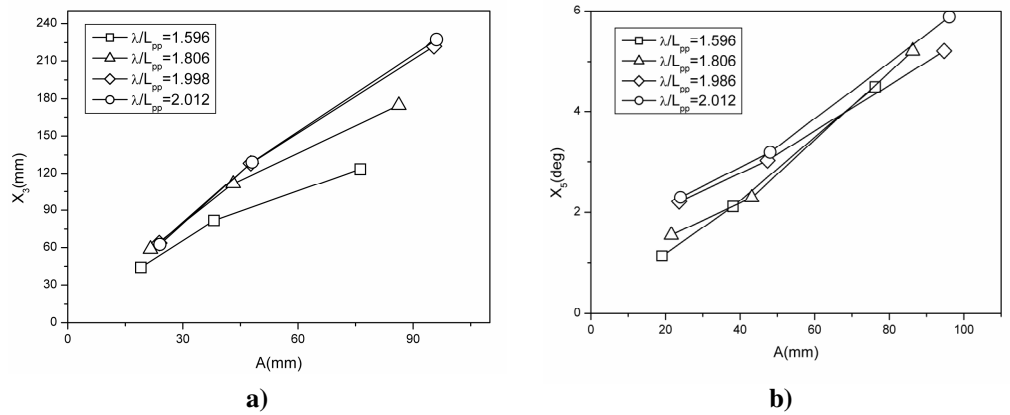

Fig.4.10 Effects of wave steepness on ship response **a)** Heave amplitude in (mm) as a function of the incoming wave amplitude (mm); **b)** Pitch amplitude in degrees as a function of the incoming wave amplitude.

Results show that for high wavelengths (λ/L_{pp}> 1.6) the heave motion amplitude is proportional to wave amplitude in the range of steepness under observation (including low and high amplitudes). At lower wavelengths, the ship response is linear only for small amplitudes of the incoming wave (Ak=0.025;0.05) and a non-linear response, consisting in a reduction in wave motions, is observed at the highest amplitude (Ak=0.1) (Fig.4.9 a and 4.10 a).
For pitch motion amplitudes, (Fig.4.9 c and 4.10 b), non-linearity seem to occur over the whole range of wavelengths and amplitudes under observation. However, pitch angles are quite small (2°-3°) and differences are not high enough to be appreciable.

4.5 Total resistance coefficient in waves

Evaluation of added resistance in waves is an important issue in seakeeping studies and is a consequence of the interaction between incident waves and the ship. The added resistance is due to the ship's ability to generate unsteady waves and is caused by the relative motion between the waves and the ship. A typical non-dimensional added resistance curve is illustrated in Fig. 4.11, where the added resistance R_{AW} is non-dimensional by the square wave amplitude, A^2. In fact, at first approximation R_{AW} is proportional to A^2 as a consequence of linearity of heave and pitch motions. It can be observed that when the ratio λ/L_{pp} between the wave length and the ship's length is small (λ/L_{pp}< 0.5), the ship movement due to the incident waves is negligible (see ship motions in Fig.(4.3,4.4,4.5)). However, as the hull reflects waves so that unsteady waves are generated, a finite added resistance is present. A peak is observed when λ/L_{pp} is in the vicinity of resonant conditions for heave and pitch, where the relative motions between the ship and waves are larger. Finally for the highest wavelengths, the relative motions between the ship and the water goes to zero and the ship does not generate unsteady waves. As a consequence the added resistance vanishes.

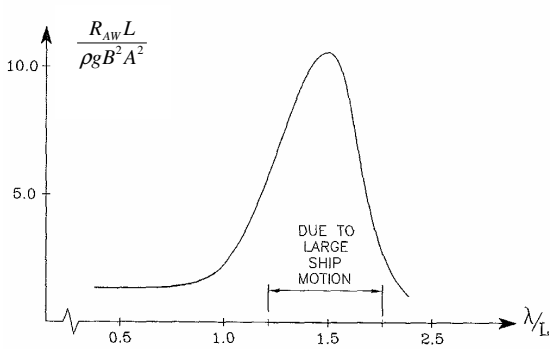

Fig.4.11 Typical wavelength dependency of non-dimensional added resistance, R_{AW} , of a ship advancing in regular waves. R_{AW} is non dimensional by square wave amplitude, A^2. B is the beam of the ship, L is the length of the ship. At low wavelengths a finite added resistance is present. In the vicinity of resonant wavelengths a peak is registered. At higher wavelengths added resistance vanishes.

An example of the importance of added resistance respect to other resistance components is illustrated in Fig. 4.12. Its evaluation is important not only at resonant conditions, where it is maximum, but also in the range of low wavelengths, as small sea states are the most frequently encountered by a ship. As an example, the added resistance for a 198m long container vessel in the North Athlantic routes where the target speed is 22 knots, produces a speed loss of about 1.7 knots, therefore quite relevant.

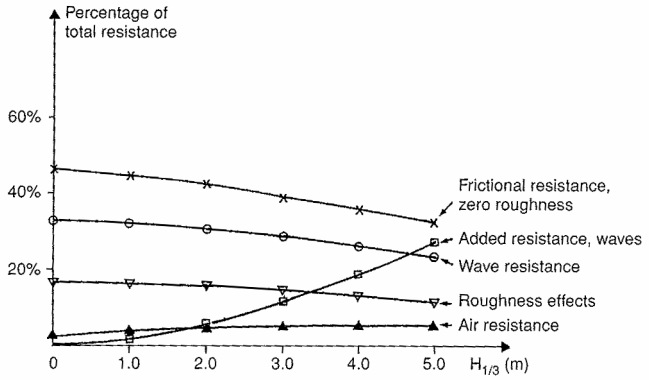

Fig.4.12 Relative importance of resistance components for a 70-m long catamaran, in head waves. $H_{1/3}$ is the significant wave height. Ship speed is 39.6 knots in calm water.

To calculate the added resistance for the case under study of the DELFT catamaran and its dependence on wavelength and wave amplitude, evaluation of the total resistance coefficient, C_T, is needed both in waves and in calm water. In this paragraph results of C_T for all the test conditions summarized in Table 3.2 are presented. Figure 4.13 shows the time history of the total resistance coefficient for Fn=0.45 and $\lambda/L_{PP} \approx 1.001$ over one period.

Its dependence on time reflects the variation in pressure distribution on the wetted hull surface, as described in Fig 4.8(b-d-f-h). The peak is observed in correspondence of 0 <t/T<1/4 where a high suction pressure is registered over the stern of the ship. As the crest passes through the ship, this suction zone decreases and passes the stern so that its effects on the hull surface decrease and reach a minimum at t/T=3/4.

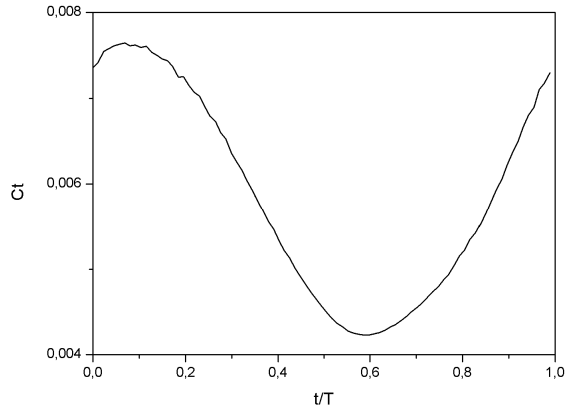

Fig.4.13 Total Resistance Coefficient as function of time over one period, T, for Fn=0.45 and λ/L_{pp}=1.001.

Total resistance coefficient for different Froude numbers were derived as averaged values over time and wavelength. The results are presented in Fig.4.14:

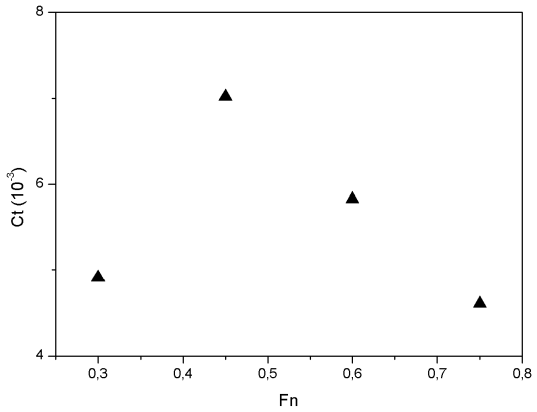

Fig.4.14 Total Resistance Coefficient in waves as function of Froude number Fn.

The points show the typical ship resistance curve. These results will be compared, in the following paragraphs, to the resistance values obtained in calm water in order to evaluate the added resistance.

4.6 Calm water tests

Experimental results are available for resistance, sinkage and trim for the catamaran advancing in calm water in a speed range Fn=0.18-0.75. The same conventions as heave and pitch motions are used in this case for sinkage and trim, hence trim is positive bow up, while sinkage is negative when the ship moves down the free surface at rest. Simulations were carried out and the results are compared with available experimental results in Fig.4.15.

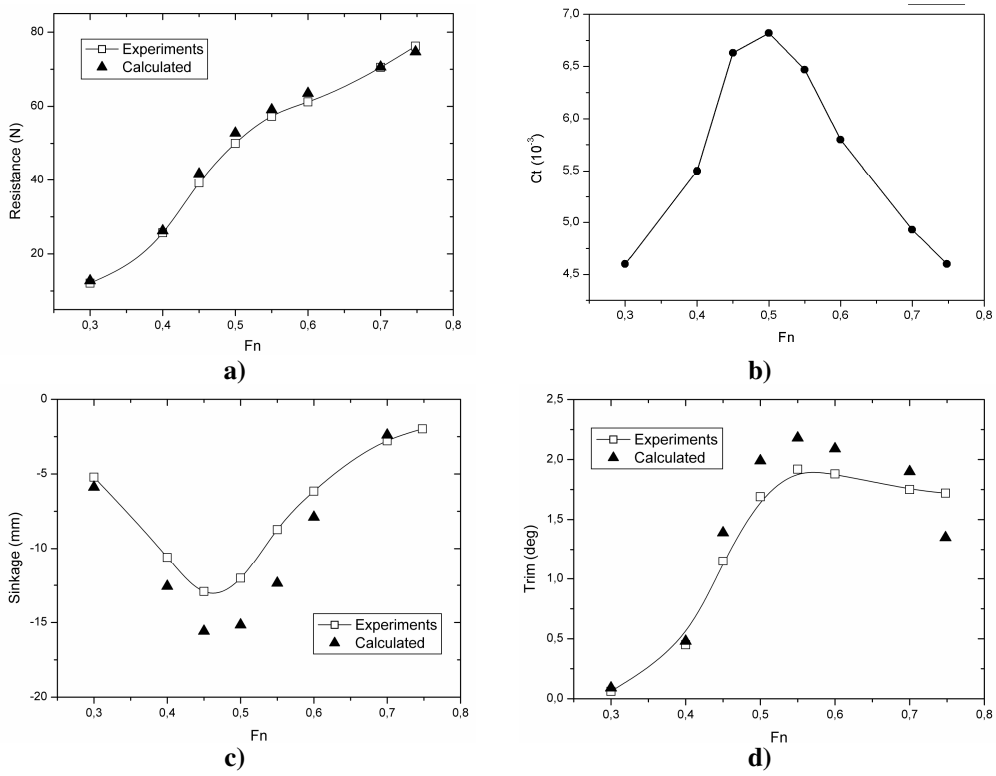

Fig.4.15 Catamaran advancing in calm water: comparison between experimental data and calculated values as functions of Froude number, Fn. **a)** Resistance (N)**;b)** Total resistance coefficient**,** C_T**; c)** Sinkage (mm); **d)**Trim angle (deg). Total resistance coefficient is maximum for Fn=0.55 and the peaks for sinkage and trim occur at the same value of Fn.

The explanation of the trends for resistance, sinkage and trim are more clear with the help of Fig.(4.16), that shows the surface pressure and wave elevation for three Froude numbers (0.3, 0.55, 0.7) which correspond to the regions before the C_T peak, near the peak and past the peak, respectively. Due to the symmetry of the problem, only results for one hull are illustrated and the interference effects between the wave systems generated by both hulls are evident in the inner region with more pronounced crests and troughs. High suction pressures due to wave trough interference at the stern can be observed for Fn =0.55 and cause the resistance peak. For Fn=0.3 the suction pressure is lower and for Fn=0.7 the wave trough interference goes beyond the stern and

the effects on the hull surface are limited. Trim angle, that is caused by the difference in pressure distribution between the bow and the stern, follows a similar trend as C_T. In fact for Fn=0.55, the pressure difference between bow and stern is more relevant than in the other two cases. Also sinkage depends on this pressure distribution. In fact, sinkage values negative value in the whole range of speeds under study. This is due to the net negative hydrodynamic forces which act on the hull wetted surface and are generated by the wave troughs and by their suction effects on the center of gravity below the free surface. The sinkage maximum can be observed for Fn=0.55 where the highest suction pressure acts on the whole stern area. In the other two cases both area and pressure values are more limited.

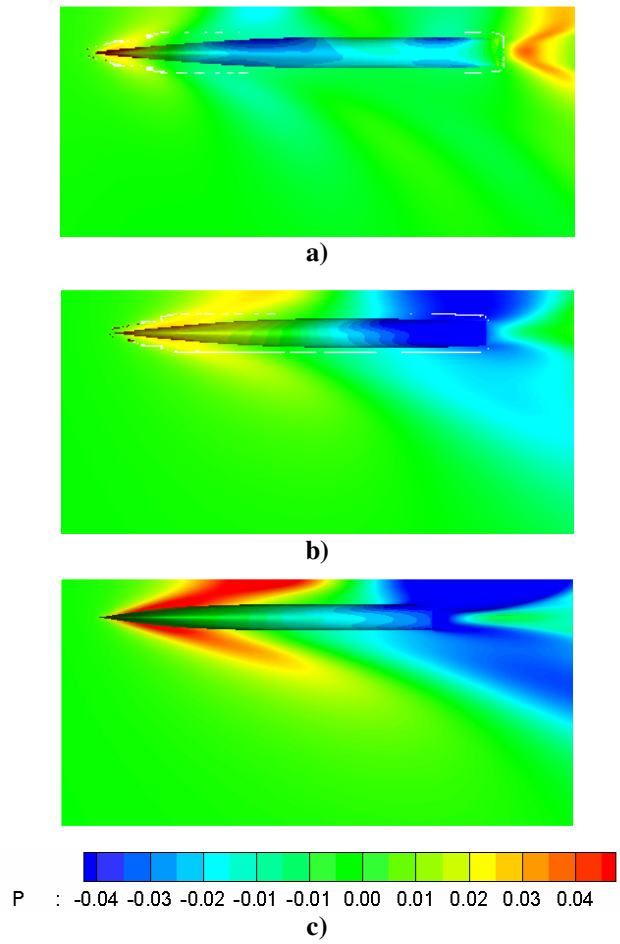

Fig.4.16 Wave elevation and pressure distribution on the hull surface for the catamaran advancing in calm water: **a)** Fn=0.3; **b)**Fn=0.55; **c)**Fn=0.7. Legend is referred to pressures on the hull surface. In the inner region between hulls more pronounced crests and troughs are registered due to the interference effects between both hulls. For Fn=0.55, where C_T reaches the peak, high suction pressure are observed over the entire stern, for Fn=0.3 suction pressures are lower, for Fn=0.7 the wave trough goes beyond the stern. In both cases a and c, the hull portion interested to high suction pressures is reduced and as direct consequence a reduction in ship resistance is observed.

4.7 Added resistance in waves

Added resistance is strictly related to the length of the incoming wave and to its amplitude, but its dependence on ship speed is also relevant and is shown in Fig.4.11. Added resistance can be evaluated as the difference between the resistance in waves and in calm water. A comparison between the total resistance coefficient, C_T, calculated in calm water for a range of ship speeds Fn=0.3-0.75, and in waves for Fn=0.3;0.45;0.6, and 0.75 shows that the added resistance in waves is significant for low ship speeds (Fn≤0.5) while it is negligible for higher Fn values (Fig.4.17).

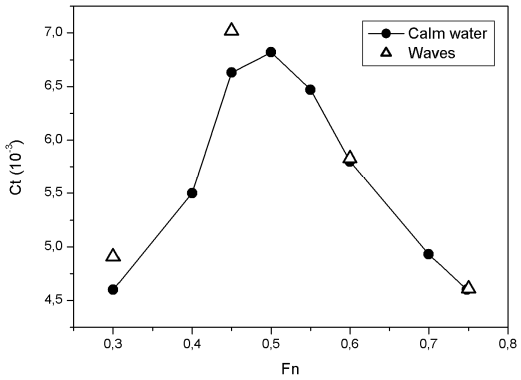

Fig.4.17 Comparison between calculated C_T values in calm water and in waves as function of Fn; ΔC_T is significant at low speed values (Fn≤ 0.5) while it is negligible for high Fn values.

This behavior can be explained on the basis of the difference in ship motions between the calm water case and the waves case (Fig.4.18). In fact, the zero-order harmonic components of heave and pitch motions in waves, show higher values than the sinkage and trim values in calm water at the same speed (Table 4.3). In waves, therefore, the ship moves deeper in water and with a higher rotation angle than in calm water. This causes the added resistance component. Moreover, the difference between heave 0^{th} harmonic and sinkage is higher for lower speeds while it decreases as speed increases. This is in accordance with the trend of the added resistance.

Table 4.3 Calculated zero-order harmonic components of heave and pitch motions in waves and corresponding sink and trim in calm water for different Froude numbers.

Fn	$x_{3,0}$ (mm)	$x_{5,0}$ (deg)	Sink	Trim
0.3	-9.7	0.176	-5.88	0.091
0.45	-23.12	2.98	-15.58	1.39
0.6	-12.076	3.67	-7.89	2.09
0.75	-5.39	3.28	-2.59	1.35

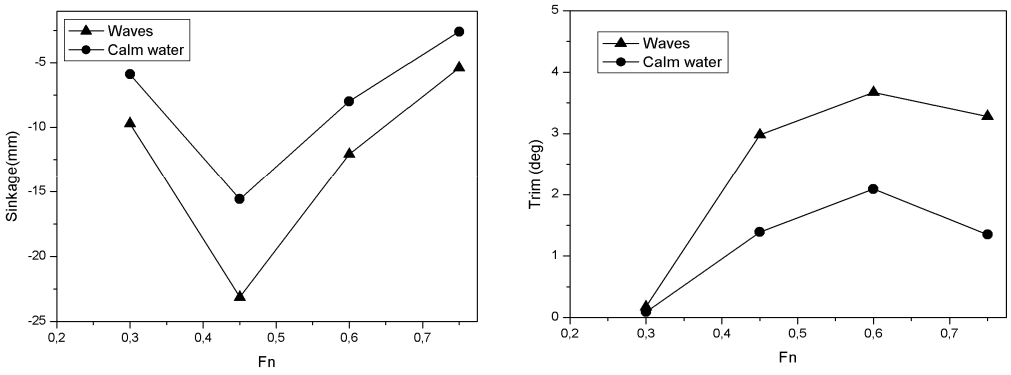

a) **b)**

Fig.4.18 a) Comparison between calculated zero-order harmonic component of heave motion in waves and calculated sinkage in calm water as functions of Fn; **b)** Comparison between calculated zero-order harmonic component of pitch motion in waves and calculated trim in calm water as functions of Fn

The assumption that added resistance is a quadratic function of wave amplitude is common in seakeeping studies and it is based on the linearity hypothesis of heave and pitch motions. This dependence is usually put in evidence by evaluating the added resistance is in terms of the added resistance operator defined as $\delta C_T/A^2$, where δC_T is the increase in drag coefficient over its calm-water value and A is the wave amplitude. In order to evaluate the validity of this assumption for the catamaran in its usual working conditions (high speeds), the C_T operator was calculated for the highest speed value (Fn=0.75) at three different wavelengths (λ/Lpp=1.596,1.806 and 2.012) and three steepness values (Ak=0.025, 0.05 and 0.1). Results are plotted in Fig.(4.19):

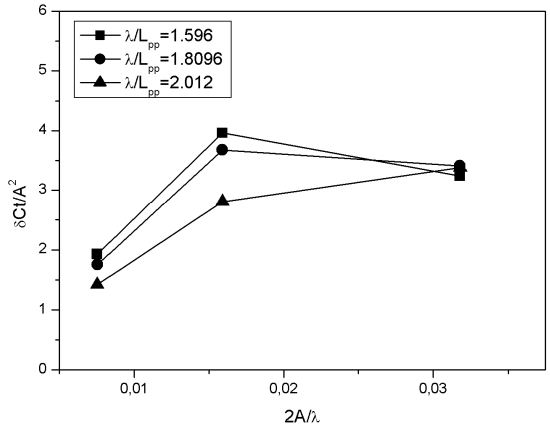

Fig.4.19 Calculated C_T operator ($\delta C_T/A^2$) as function of steepness ($2A/\lambda$) for different wavelengths. The dependence of δC_T on A is more than quadratic for higher and lower wavelengths

It can be observed that for highest wavelength value (λ/L_{pp}=2.012), the dependence of δC_T on A is more than quadratic, however this dependence on wave steepness is weak. As wavelength decreases, the gap from quadratic dependence of δC_T on A is more severe and this reflects the response of ship motions that is linear with wave steepness only for high wavelengths. From the above considerations it can be concluded that the usual assumption that added resistance is a quadratic function of wave amplitude can be accepted only for high wavelengths but it is not satisfied at the lower wavelengths as a consequence of the non-linear response of ship motions.

4.8 Verification and Validation for the DELFT catamaran

To quantify numerical errors and uncertainties in CFD simulations, convergence studies, following the methodology presented by Stern et al.[40] and briefly discussed in paragraph 3.5, were conducted for grid spacing and time step with time step and grid size given in tables 4.4 and 4.5. The time steps were chosen in order to be at least 80 per wave period and a refinement ratio of $r_t = \sqrt{2}$ was used.

Table 4.4. Time steps in V&V study with refinement ratio r_t=$2^{(1/2)}$

	Coarse	Medium	Fine
ΔT	0.0127	0.009	0.00636
Time steps/Wave Period	83	117	167

A refinement ratio of $r_G = \sqrt{2}$ was also used for grid convergence study:

Table 4.5. Summary of grids used in V&V study with refinement ratio r_G=$2^{(1/2)}$

	Fine	Medium	Coarse
Body Fitted 1	139x65x91	98x46x64	69x32x45
Body fitted 2	139x65x91	98x46x64	69x32x45
Background	309x139x88	218x98x62	154x69x44

For the grid study, 117 time steps per wave period were use on the fine, medium and coarse grid. For the time step study the finest grid was used to obtain solutions with 83, 117 and 167 time steps per wave period. The test conditions are summarized in Table 4.6:

Table 4.6 Summary of the V&V test conditions

Grid \ *Time step*	**Fine**	**Medium**	**Coarse**
Fine	**X**	**X**	**X**
Medium		**X**	
Coarse		**X**	

The resonant physical conditions were chosen because large ship motions result in highest numerical sensitivity, making this the worst test case. The verification parameters of the first harmonic of heave, x_{3_1}, and pitch, x_{5_1} were chosen, as they are the only available experimental data.

Verification procedure provides an estimation of the numerical error given by the sum of the iterative error and of the grid and time step spacing errors (Eq.4.8,4.9). Iterative convergence was assessed by examining iterative history of ship forces. It resulted that residuals drop four order of magnitude from the first to the last iteration and reached a final value of 10^{-6} so that they are negligible in comparison to the grid and time step errors.

$$\delta_{SN} = \delta_I + \delta_G + \delta_T \tag{4.8}$$

$$U_{SN}^2 = U_I^2 + U_G^2 + U_T^2 \tag{4.9}$$

Results for time step convergence study are summarized in Tables 4.7 and 4.8:

Table 4.7. **Time step convergence study**: results for first harmonic amplitudes of heave and pitch motions

	Calculation Results for Coarse, Medium and Fine time steps			*Solution Changes between Calculated Solutions*		*Experimental Data*
	Coarse (3)	Medium (2)	Fine (1)	$\varepsilon_{t,32}*10^3$	$\varepsilon_{t,21}*10^3$	D
x_{3_1}	0.01688	0.01728	0.01749	0.402	0.215	0.01599
x_{5_1}	0.02351	0.02376	0.02387	0.252	0.109	0.0239

Table4.8. Time convergence verification of first harmonic amplitude of heave and pitch motions

	R_t	P_t	C_t	$U_t(\times 10^{-3})$	δ_t^*	U_{tC}
x_{3_1}	0.5348	1.806	0.8697	0.24719	0.000215	$3.22 \cdot 10^{-5}$
x_{5_1}	0.434	2.408	1.3044	0.1094	0.000109	$2.55 \cdot 10^{-5}$

ε_{32} and ε_{21} are defined in Eq (3.25) and Eq.(3.26) and indicate the difference between the coarse and medium solutions and medium and fine solutions respectively. The ratio R_t (Eq.3.27) indicates the level of convergence of the solution. It can be observed that both for x_{3_1} and x_{5_1}, $R_t < 1$, hence monotonic convergence between solutions is assessed and the generalized Richardson extrapolation (RE) can be used in estimating U_t, δ_t^* and U_{tc} according to Eq. (3.33), (3.30) and (3.32). In more detail, $\delta_{t_1}^* = \delta_{RE_t}^* = \frac{\varepsilon_{t_{21}}}{r_t^{p_t} - 1}$ is calculated by using the order of accuracy p_t given by $p_t = \frac{\ln(\varepsilon_{t_{32}} / \varepsilon_{t_{21}})}{\ln(r_t)}$. By introducing the correction factor, $C_t = \frac{r_t^{p_t} - 1}{r_t^{p_{test}} - 1}$ where $p_{t,est}=2$, δ_t^* is calculated as:

$$\delta_t^* = C_k \delta_{RE_t}^* = C_t \left(\frac{\varepsilon_{t_{21}}}{r_t^{pt} - 1} \right) \tag{4.10}$$

$$U_t = \left| C_t \delta_{RE_t}^* \right| + \left| (1 - C_t) \delta_{RE_t}^* \right| \tag{4.11}$$

and

$$U_{k_c} = \left| (1 - C_k) \delta_{RE_{k1}}^* \right| \tag{3.32}$$

The same approach was applied for the grid convergence study, and results are presented in tables 4.9 and 4.10:

Table.4.9 Grid convergence study: results for first harmonic amplitudes of heave and pitch motions

	Calculation Results for Coarse, Medium and Fine grids			*Solution Changes between Calculated Solutions*		*Experimental Data*
	Coarse (3)	Medium (2)	Fine (1)	$\varepsilon_{G,32}*10^3$	$\varepsilon_{G,21}*10^3$	D
x_{3_1}	0.0168	0.01722	0.01749	0.42	0.275	0.01599
x_{5_1}	0.020058	0.0225	0.02387	0.244	0.808	0.0239

Table 4.10.Grid convergence verification of first harmonic amplitude of heave and pitch motions

	R_G	P_G	C_G	$U_G (\times 10^{-3})$	δ_G^*	U_{GC}
x_{3_1}	0.655	1.22	0.52	0.523	0.000275	0.000247
x_{5_1}	0.33	3.19	2.022	0.399	0.000808	0.000408

As the uncertainty in experimental data is not given, fairly low value of U_D=*2.5%* of the data was assumed. The validation uncertainty U_V was then calculated, since it is defined as $U_V^2 = U_D^2 + U_t^2 + U_G^2$. The comparison error, *E*, defined as the difference between data and the simulation value of the finer simulation ($E = D - S_1$) was calculated both for x_{3_1} and x_{5_1}. All the values, reported as percentage on the experimental data, are summarized in Table 4.11:

Table 4.11.Validation of first harmonic amplitude of heave and pitch motions

	U_G	U_t	U_D	U_V	E
x_{3_1}	3.27%	1.54%	2.5%	4.39%	9.38%
x_{5_1}	1.66%	0.45%	2.5%	3.04%	0.12%

For pitch motion, the comparison error is less than the validation uncertainty U_V, hence it is validated at the U_V level of 3%. On the contrary, heave motion was not validated, as the comparison error is 9.38%, greater than the noise level imposed by U_V at 4.4%. Better results were obtained by using the corrected approach [40]. The corrected comparison error, E_C, is defined as the difference between the data and the corrected simulation value (S_C) ($S_C = S - \delta_{SN}^*$) where δ_{SN}^* was calculated both for time step study and grid study, and reported in tables 4.8 and 4.10 respectively. An error of 6.3% was calculated. In this case the validation was achieved at an uncertainty level of 6.3% that can be considered satisfactory and it is in accordance with uncertainty levels found in previous studies, where simpler working condition were involved.

Chapter 5

Circulating Water Channel for Experimental Tests on Ship Models

5.1 Introduction

The Ph.D. activity developed and presented in this work includes the design of an experimental apparatus for ships model testing. The idea came out from the project sponsored by the *European Community* to realize *Transportation Quality Centers* in South Italy, by setting up laboratories in which tests for optimization of public transportation and heavy goods transportation both on roads or sea could be made. The *Department of Mechanical Engineering* set up a laboratory for ships hydrodynamics focusing on sea transportation for three main reasons:

I. considering that most of the sea viability is concentrated in South Italy for connection with islands, fast sea transportation is an extremely interesting research field for this area;
II. due the wide coastal area, many little shipyards are present and work in this area and can have interests in collaborations with laboratories for design and testing of ship models;
III. finally, CFD technology gives the most useful results if used in conjunction with model testing in ship design. Experimental Fluid Dynamics (EFD) remains, in fact, a fundamental tool that is evolving in technology giving high quality results that are important not only in the process of ship design but are also used as benchmark data in CFD codes validation.

The description of the experimental apparatus follows in the next paragraphs.

5.2Background

Model testing according to Froude similarity, as widely discussed in Chapter 1, usually is attempted in towing tanks which have a wide range of dimensions. As example the towing tank available at INSEAN (Italian Ship Model Basin, Rome) is 470m long, 13.5m large and 6.5 m deep and is considered one of the biggest tanks in the world. The towing tank available at IIHR (Iowa Institute of Hydraulic Research, USA) is 100m long, 3m deep and 3m large. The dimensions are strictly related to the speeds reached by the model during tests, in which the model towed by a carriage needs enough space to reach and maintain the required constant speed and then to brake and stop. The depths have to be high enough to avoid the shallow water effects due to the bottom of the tank, that can alter the wave formation and alter the ship resistance, while the widths have to take into account the boundary layer effects of the side walls and the interaction with ship waves.

The actual towing tanks are equipped with advanced instrumentations that allow more detailed analysis of the flow field around the model and in the wake region in order to study the flow around the propeller and to gain a better understanding of ship hydrodynamics. In the last 20 years the use of advanced optical measurements techniques like Laser Doppler Velocimetry (LDV) has provided deep insight into the flow fields, allowing the measurements of the mean and fluctuating velocity fields with high accuracy also in complex flows. Some limitations of the LDV technique are related to its single point measurement nature. Hence, it can hardly give an idea of the spatial characteristics of large coherent structures generated in complex flows and it needs long periods of operation for characterizing a whole velocity field, thus increasing the testing costs. The Particle Image Velocimetry (PIV) technique, recently introduced in measurements of ship flows, overcomes the limits of the single points techniques, being a whole field measurement technique. It allows the reduction in testing times and gives more detailed information also for complex structures measuring the three velocity components (Stereo PIV).

The towing tanks are generally equipped with other facilities for the measurement of ship resistance, for measurement of wave height and wave profile on the hull surface, it's also possible to install wave makers for seakeeping tests.

The spaces available in the *Laboratory* of the *Dept. of Mechanical Engineering* to set-up the experimental apparatus for model tests do not allow the building of a towing tank. Hence the solution of a circulating water channel of limited dimensions was adopted. Circulating water channels constitute a valid tool for model testing and are present in literature [6,18], although less frequently than the towing tanks. PIV measurements of flow around a model of the KRISO3600 were conducted [18], on a channel having a test section of $1.0^{W}x1.0^{H}x4.5^{L}$, and other experiments were conducted at INSEAN in a circulating water channel [6].

A circulating water channel was then designed and developed. The main elements of the channel are (Fig.5.1):

- Plexiglas channel having dimensions: $L \times B \times H = 4.5 \times 0.8 \times 0.15(m)$;
- Upstream channel tank volume $V_{US} = 1.1m^3$;
- Downstream channel tank volume $V_{DS} = 2.86m^3$;
- Centrifugal Pump (Power=11KW;1000rpm);
- Pipes diameter $\phi = 200mm$;
- Flow rate measurement system;
- PIV measurement system.

The channel details, the PIV measurement system and the test conditions will be described in more detail in the following sections.

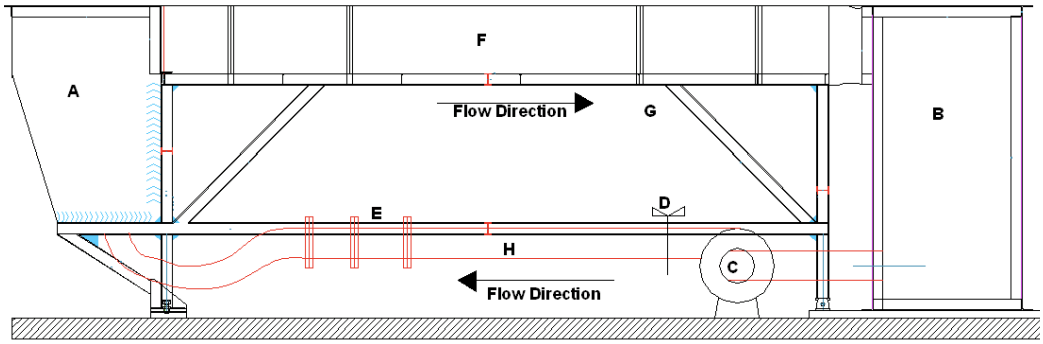

Fig.5.1 Sketch of the circulating water channel; A)Upstream tank; B)Downstream tank C)Centrifugal pump; D)Gate valve; E)Flow rate measurement system; F) Plexiglas channel; G) Steel frame; H)Pipes.

5.3 Channel description

The channel dimensions were chosen on the basis of the desired test conditions and according to space limitations. The maximum length of the channel was fixed in L=4.5m considering that, for space restrictions, the whole structure should be no more than 7m long and that additional space was needed for the feed and drain tanks, which are positioned respectively upstream and downstream of the channel. A section of BxH=0.8x0.15 (m) was chosen for the channel in order to avoid the boundary layer effects, the wave reflections from the side walls and the interaction between the hull and the bottom of the channel, which could create shallow water effects. The following characteristics (Table 5.1) for model geometry were considered, by using as references the values of the DELFT catamaran geometry, that are typical of slender bodies:

Table 5.1. Dimensions of model geometry

Main Particulars	Units	Value
Length between perpendiculars, L	m	0.5
Beam to length ratio, B/L		0.08
Draught to length ratio, T/L		0.05
Beam	m	0.04
Draught	m	0.025

A model L=0.5m long, has a beam of B=0.04m and a draught of T=0.025m.

Under test conditions at a Froude number Fn=0.6, the corresponding speed of the water circulating in the channel was calculated according to the Froude number definition, where L is the model length:

$$Fn = V \Big/ \sqrt{g \cdot L} \tag{5.1}$$

A V=1.32 m/s (2.5 knots) resulted, which corresponds to a volumetric flow rate of 574 m^3/h.

Adoption of longer models is possible, but limitation to model flows at lower Froude numbers would result. In fact, the higher Froude numbers would require mass flow rates higher than 574 m^3/h and hence huge tanks for water storage. As example, for a speed of V=1.32 m/s, a model having L=0.7 would experience a Fn=0.5 and a model with L=0.8 would experience Fn=0.46, which however are in the range of speeds usually tested in towing tanks (Fn=0.1-0.5). Reductions in model dimensions on the other side, would require too low draught values and the wave elevations would be too small and too difficult to detect. For a model of 0.5m the allowable flow conditions in the channel are summarized in the following table:

Table 5.2. Flow speed in the channel (BxH=0.8x0.15) for a model having L=0.5m.

Froude Number	V(m/s)	Q(m^3/h)
0.2	0.443	191.3
0.3	0.664	287
0.4	0.886	382.7
0.5	1.107	478.3
0.6	1.32	574

Higher speed values in the channel are obtained by adopting a proper pitch angle, calculated on the basis of the Manning formula :

$$U = k_S R_i^{2/3} i^{1/2} \tag{5.2}$$

where U is the average speed in the transverse section, k_s is the roughness coefficient that for Plexiglas is $k_s = 111 m^{1/3}/s$, R_i is the hydraulic radius and i is the channel inclination. In this case by giving an inclination of 0.1% , the water speed reaches the value U=1.6 m/s while with an inclination of 0.15% a speed of U=1.7 m/s can be reached. This represents a speed limit since, inclination of channel with constant mass flow rate, produces a reduction in water depth that, with higher speed values, would be not negligible.
The following table (Table 5.3) summarizes the test condition ranges:

Table 5.3 Allowed Test Conditions in the channel

Model Size Range:	0.5-0.8(m)
Working Section Maximum Velocity:	V=1.32 m/s (i=0) V=1.7 m/s (i=0.15%)
Tests Performed:	Resistance, Ship motions, flow field
Instrumentation:	PIV and flow rate measurement system are the only available at the moment, but inclusion of load cells and devices for ship motions are scheduled.

The whole plant was set-up with pipes having diameter of $\phi = 200mm$, to allow the maximum mass flow rates in the channel and considering that prescribed speeds in pipes do not have to exceed the value of 4 m/s. A gate-valve was installed for flow-rate regulation and a flow-rate measurement system was installed to ensure that the prescribed test conditions are reached in the channel. Water circulation is supplied by a centrifugal pump having power P=11KW and rotating at 1000rpm. Fig.(5.2) includes the working points of the whole system for different positions of the gate valve:

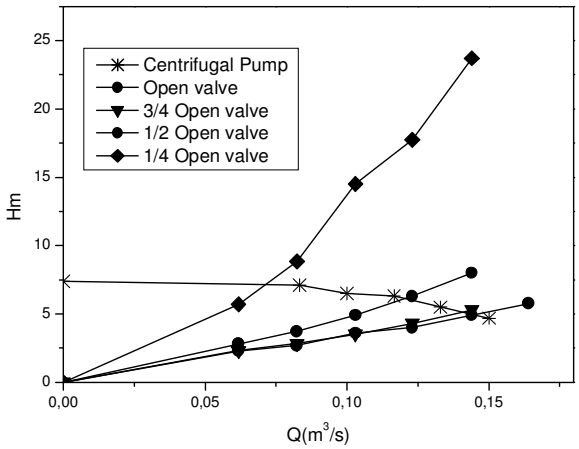

Fig. 5.2 Q-H curves for the pump and the plant at different positions of the gate valve. Q is the flow rate in m^3/s, H_m is the height in *m*.

5.4 The PIV system

Recent literature shows the advantages of this technique to the naval field [6,15,18]. In towing tank applications the flow characteristics over the stern and in the near-wake region were investigated for different ship models [15,18]. PIV has found wide application in studies on propeller flows and on the interaction with wake flows. The high quantity and quality of data obtained using PIV technique constitute a fundamental tool for collecting reliable experimental benchmark data for CFD codes validations.

Particle Image Velocimetry (PIV) is a whole-flow field technique which provides instantaneous velocity vectors measurements is cross-section of a flow. The main characteristics that make it a wide used measurement system can be summarized in the following points:

- It is a non intrusive technique;
- Instantaneous velocity vector maps are obtained in a wide area of the flow-field;
- Results are similar to CFD and velocity maps, statistics, spatial correlations and other relevant data are available.

The main features of a typical PIV System are summarized in Fig.(5.3):

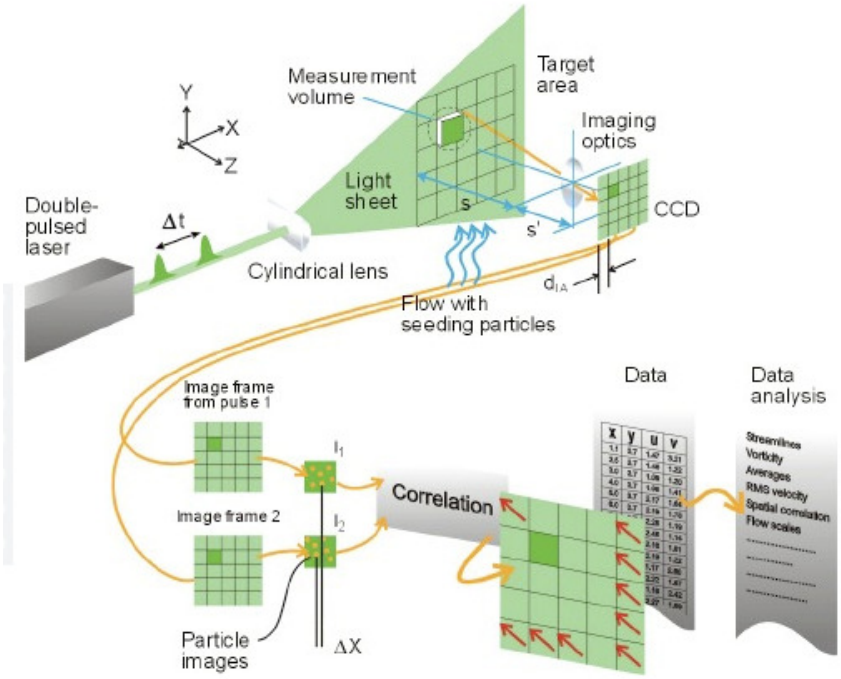

Fig.5.3 PIV working principle

The flow is seeded with small particles that follow the flow. A laser light is pulsed twice with a short time delay *dt* and creates a light sheet. Both light sheets are recorded by one double-frame high resolution CCD camera

During the interval time *dt*, between both laser pulses, the seeding particles move by a displacement *ds* and, by the different positions of the particles in both images, it is possible to calculate *ds* and hence the velocity vector given by *ds/dt*. This can be achieved considering that the recorded images are divided into small interrogation windows (Fig.5.4) having typical sizes from 64x64 to 8x8 pixels. For each interrogation window the displacement is calculated by an FFT based cross-correlation of two corresponding interrogation windows and the position of the highest peak in the correlation plane indicates the mean displacement *ds*. Finally the velocity vectors are obtained for each interrogation window and the complete instantaneous velocity vector map is obtained. This technique gives two velocity vector components, but this system offers the possibility to obtain the third out of plane component of velocity by using two cameras instead of one.

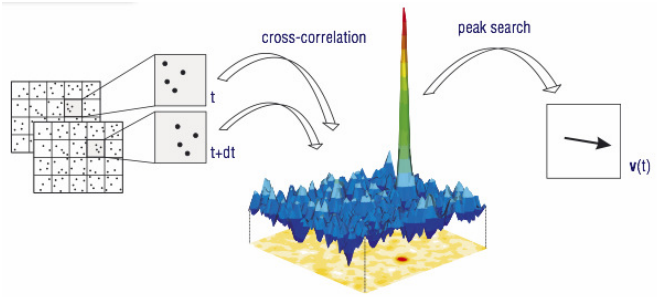

Fig. 5.4 Velocity vector reconstruction: Recorded images at *t* and *t+dt* are divided in little interrogation windows. By an FFT cross correlation between two corresponding interrogation windows, the average displacement of the particles corresponds to the position of the highest peak in the correlation plane.

The developed water channel was equipped with a *Dantec Dynamics* PIV system. The Nd:Yag laser maximum energy output is larger than 200 mJ per pulse and the maximum pulse repetition rate is 15 Hz, the pulse width is of about 6-9 ns and its power is less than 2.5 KW. The CCD camera has a resolution of 1600x1200 pixels and can capture images at a frame rate of 30 f.p.s(frames per second) and a depth of 10 bits per pixel. A delay generator is used to synchronize the laser and the CCD camera and it controls the time delay dt between two laser pulses. Finally the software *Dynamic Studio* by *Dantec Dynamics* is used for acquiring, storing, and analyzing the image based data, hence no extra data acquisition tools are needed.

5.5 Model tests

Figures 5.5, 5.6, and 5.7 present some views of the channel:

a)The flow is from right to left in the channel. The system components are: Upstream and downstream tanks, the channel in Plexiglas, the pipes and the pump

b) PIV system: Laser Source, laser sheet generator, PC, CCD camera.

Fig. 5.5 Overview of the whole plant

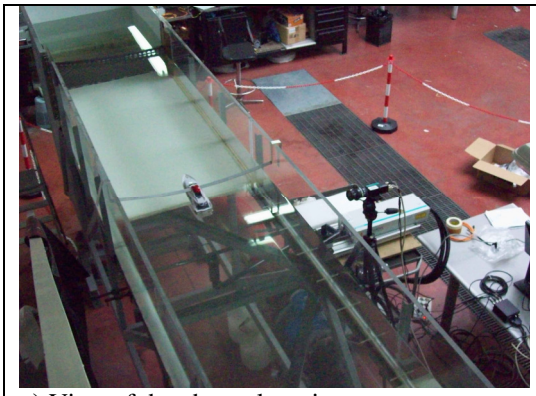

a) View of the channel section.

b) View of the model fixed in the channel

Fig.5.6 The channel

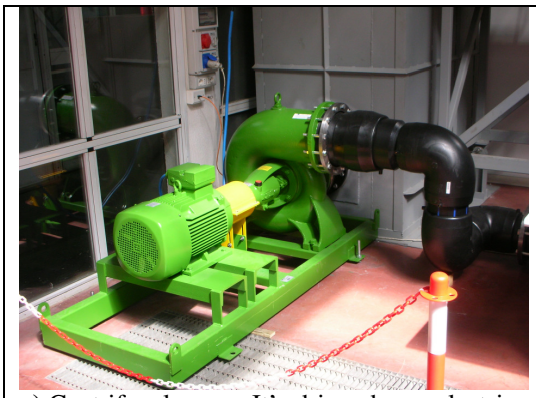

a) Centrifugal pump. It's driven by an electric motor (P=11 KW) with two poles at 1000rpm.

b) Pipes F=200mm and gate valve.

Fig.5.7 Particulars of the plant

The whole plant was tested and all the components proved to work according to the design conditions. In particular, a model of length=0.8m with a transom stern was tested and the flow characteristics at the stern were analyzed. The water speed in the channel reached its maximum (wide open gate valve) V=1.3 m/s corresponding to Fn=0.46. In Fig.(5.8) some steps of the PIV measurement are shown.

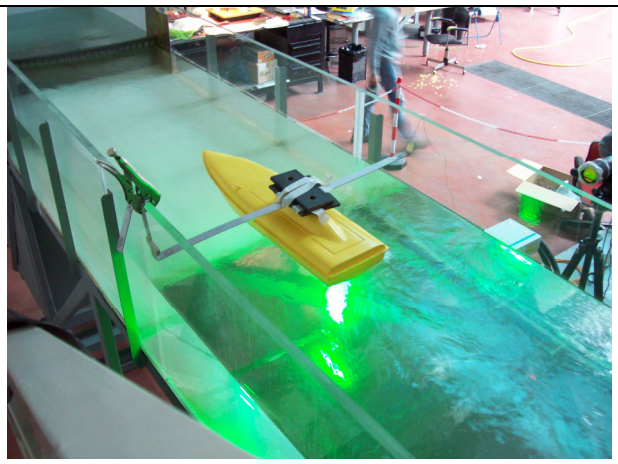

a)

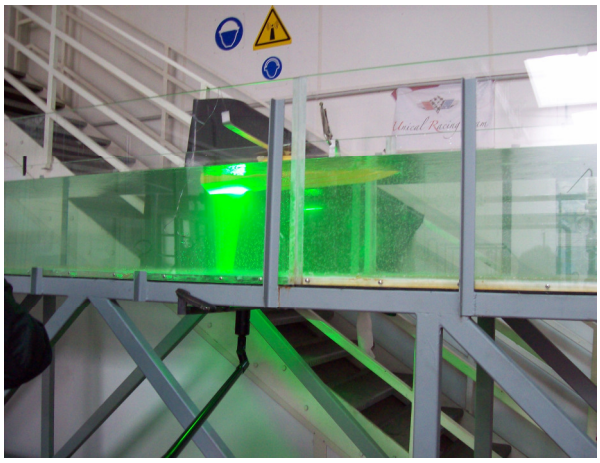

b)

Fig.5.8 PIV measurements for a ship model having a transom stern

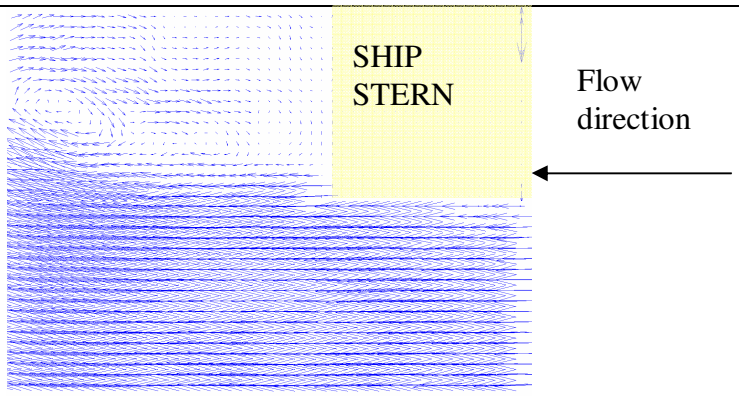

a)

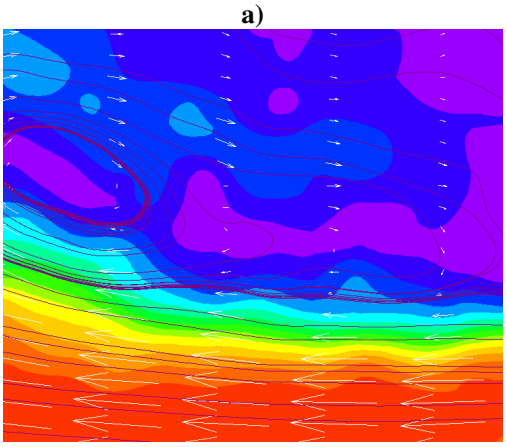

b)

Fig.5.9 Measured flow-field behind the stern. **a)** Velocity vectors **b)** Velocity contours and streamlines. A vortex behind the stern is captured.

During the tests it was observed that the flow in the channel is quite regular and that the vortex behind the stern was captured. In particular, in Fig.(5.9) the results of the PIV measurements are displayed. In Fig.(5.9a) the velocity vectors in the vertical plane, behind the stern are shown, while in Fig(5.9b) velocity contours are displayed with streamlines

The experimental set-up was completed just before the writing of the present thesis, therefore the above measurements have illustrative purpose and do not have yet scientific relevance. More accurate and rigorous tests will be carried out during next weeks on the model scale of the DELFT catamaran.

Conclusions

The main aspect of the Ph.D. program was the application of CFD codes to complex problems concerning ship hydrodynamics. In addition, the design of an experimental apparatus to test ship models was addressed.

In particular, the seakeeping behavior of a catamaran advancing in regular waves was investigated numerically by the Unsteady RANS code CFDShip-Iowa V.4. The following conclusions can be drawn:

I. The URANS code used to predict the ship motions in the vertical plane is a valid tool in the simulation of unsteady problems involving complex flow conditions (high ship speeds, high sea states). Ship motions were predicted with a comparison error $|E|$ of 1-10% between experimental and calculated values. Validation was achieved at uncertainty (U_V) level of 6% which is consistent with the values found in previous studies, where simpler conditions were involved;

II. The formulation usually adopted to determine the natural frequency of a mono-hull ship, which was derived from linear theory, can be extended to multi-hull vessels. In fact, the natural frequency calculated for the catamaran by using the above formulation and by simulations are in agreement (*1.2 Hz* vs *1.3 Hz*);

III. The parameters which affect the maximum response conditions, i.e. the maximum ship motions, for mono-hulls and for catamaran are different. Therefore conclusions obtained for mono-hulls cannot be totally extended to multi-hull vessels. In particular, for the catamaran, the main factor which determines the maximum response of the vessel is resonance. When the catamaran advances in a wave system characterized by a frequency close to resonance, the ship vertical motion amplitude is 2.5 times the wave amplitude, resulting in the worst case working condition;

IV. The best working conditions for the catamaran are achieved at sea state conditions which involve low wavelengths. Under this circumstance, despite the presence of high amplitude incoming

waves, the ship motions are quite limited. This is due to a non-linear response of ship motions to the incoming low wavelengths waves, where the higher the wave amplitude, the more damped the ship motion amplitude.

V. The hypothesis of linear dependence of ship motion amplitude on wave amplitude, assessed by the linear theory, is valid only for low steep waves ($Ak \leq 0.05$) and is strictly dependent on wavelengths. Under these conditions a quadratic dependence of added resistance in waves with wave amplitude is demonstrated according to the assumptions made in the linear theory;

VI. Finally, the catamaran best performances are observed at the highest speed values. In fact, the resistance at the highest Fn has a quite low value($4.6 \cdot 10^{-3}$). Moreover, at the highest speed values, the difference between the resistance in calm water and the resistance in waves is negligible, resulting in a negligible added resistance component (0.2% for low amplitude waves, 15% for high amplitude waves).

In addition to the main CFD activity, an experimental apparatus to test small-scale ship models was designed and tested. It is made of a circulating water channel that allows the measurements of the flow field and ship resistance in model scale. It was equipped with a PIV (Particle Image Velocimetry) system to investigate the flow field at prescribed sections. The channel set-up was completed just before the writing of the present thesis, therefore some experiments were carried out on a ship model for illustrative purposes. The main purpose in the next future is to carry out accurate and rigorous tests on the model scale of the DELF catamaran, in order to set-up a standard procedure for model testing and to validate the results.

Appendix

A.1 Calm Water Tests

Table A.1 EFD Data for calm water tests
Resistance, Sinkage*, Trim*, and Ct

Fn	*R(N)*	*Sinkage(mm)*	*Trim (deg)*	$C_T\ (x10^{-3})$
0.3	12.77	-5.88	0.091	4.85
0.4	26.23	-12.57	0.48	5.53
0.45	41.75	-15.58	1.39	7.03
0.5	52.79	-15.16	1.99	7.27
0.55	59.08	-12.36	2.18	6.74
0.6	63.5	-7.89	2.09	6.06
0.7	70.6	-2.39	1.9	4.89
0.748	74.71	2.59	1.35	4.504

Table A.2 CFD Results for calm water tests
Resistance, Sinkage*, Trim*, and C_T

Fn	*R(N)*	*Sinkage(mm)*	*Trim (deg)*	$C_T\ (x10^{-3})$
0.3	12.12	-5.22	0.062	4.6
0.4	25.7	-10.6	0.45	5.0
0.45	39.15	-12.92	1.15	6.63
0.5	50	-12.02	1.69	6.82
0.55	57.3	-8.73	1.92	6.47
0.6	61.2	-6.15	1.88	5.8
0.7	70.5	-2.78	1.75	4.93
0.748	76.22	-1.98	1.72	4.6

*: Trim is positive bow up; Sinkage is positive upwards from the free surface at rest.

A.2 Ship motions for the catamaran advancing in regular head waves

Table A.3 EFD Data for ship advancing in waves- **Fn=0.45**

λ/L_{pp}	*Wave Amplitude, A, (mm)*	*Steepness*	*Heave RAO* $\left(x_{3_1}/A\right)$	*Heave phase (deg)*	*Pitch RAO* $\left(x_{5_1}/kA\right)$	*Pitch phase(deg)*
1.001	18.559	0.038	1.114	-96.491	0.59	152.149
1.201	17.813	0.031	2.077	-39.698	1.023	178.879
1.396	18.039	0.027	1.675	-5.386	1.231	-159.423
1.595	17.409	0.023	1.3	6.051	1.354	-141.228
1.991	18.236	0.019	1.207	3.162	1.298	-137.595

Table A.4 CFD Results for ship advancing in waves- **Fn=0.45**

λ/L_{pp}	*Wave Amplitude, A, (mm)*	*Steepness*	*Heave RAO* $\left(x_{3_1}/A\right)$	*Heave phase (deg)*	*Pitch RAO* $\left(x_{5_1}/kA\right)$	*Pitch phase(deg)*
1.001	18.559	0.038	1.156	-86.8	0.511	148.51
1.201	17.813	0.031	2.16	-31.55	1.0377	176.25
1.396	18.039	0.027	1.675	-10.3	1.313	-169.423
1.595	17.409	0.023	1.185	14.1	1.3042	-126.06
1.991	18.236	0.019	0.987	11.42	1.223	-114.38

Table A.5 CFD Results for 0^{th} harmonic Amplitude- **Fn=0.45**

λ/L_{pp}	*Wave Amplitude, A, (mm)*	*Steepness*	*Heave* $\left(x_{3,0}/A\right)$	*Pitch* $\left(x_{5,0}/kA\right)$
1.001	18.559	0.038	$8.579\ 10^{-3}$	$4.473\ 10^{-2}$
1.201	17.813	0.031	$8.018\ 10^{-3}$	$4.7\ 10^{-2}$
1.396	18.039	0.027	$8.238\ 10^{-3}$	$4.655\ 10^{-2}$
1.595	17.409	0.023	$8.549\ 10^{-3}$	$4.55\ 10^{-2}$
1.991	18.236	0.019	$8.77\ 10^{-3}$	$4.513\ 10^{-2}$

Table A.6 EFD Data for ship advancing in waves- **Fn=0.6**

λ/L_{pp}	*Wave Amplitude, A, (mm)*	*Steepness*	*Heave RAO* $\left(x_{3_1}/A\right)$	*Heave phase (deg)*	*Pitch RAO* $\left(x_{5_1}/kA\right)$	*Pitch phase(deg)*
1.393	18.801	0.028	2.197	-66.036	0.932	168
1.49	19.151	0.0269	2.37	-46.97	1.071	172.6
1.6	19.148	0.025	2.376	-29.403	1.299	-179.87
1.795	18.312	0.021	2.007	-4.306	1.657	-157.38
1.997	19.816	0.021	1.432	6.583	1.485	-137.6

Table A.7 CFD Results for ship advancing in waves- **Fn=0.6**

λ/L_{pp}	*Wave Amplitude, A, (mm)*	*Steepness*	*Heave RAO* $\left(x_{3_1}/A\right)$	*Heave phase (deg)*	*Pitch RAO* $\left(x_{5_1}/kA\right)$	*Pitch phase(deg)*
1.393	18.801	0.028	2.343	-60.68	0.86	157
1.49	19.151	0.0269	2.628	-41.43	1.11	162
1.6	19.148	0.025	2.638	-18.52	1.458	-179.8
1.795	18.312	0.021	1.967	12.4	1.7	-147.02
1.997	19.816	0.021	1.47	17.96	1.612	-131

Table A.8 CFD Results for 0^{th} harmonic Amplitude- **Fn=0.6**

λ/L_{pp}	*Wave Amplitude, A, (mm)*	*Steepness*	*Heave* $\left(x_{3,0}/A\right)$	*Pitch* $\left(x_{5,0}/kA\right)$
1.393	18.801	0.028	$4.089\ 10^{-3}$	$6.36\ 10^{-2}$
1.49	19.151	0.0269	$3.86\ 10^{-3}$	$6.5\ 10^{-2}$
1.6	19.148	0.025	$3.84\ 10^{-3}$	$6.57\ 10^{-2}$
1.795	18.312	0.021	$4\ 10^{-3}$	$6.4\ 10^{-2}$
1.997	19.816	0.021	$4.33\ 10^{-3}$	$6.23\ 10^{-2}$

Table A.9 EFD Data for ship advancing in waves- **Fn=0.75**

λ/L_{pp}	*Wave Amplitude, A, (mm)*	*Steepness*	*Heave RAO* $\left(x_{3_1}/A\right)$	*Heave phase (deg)*	*Pitch RAO* $\left(x_{5_1}/kA\right)$	*Pitch phase(deg)*
1.596	18.082	0.024	2.428	-73.22	1.078	171.38
1.806	19.95	0.022	2.532	-47.209	1.088	174.7
1.983	14.00	0.015	2.42	-19.895	1.482	-172.66
2.012	14.00	0.014	2.408	-20.848	1.503	-173.85

Table A.10 CFD Results for ship advancing in waves- **Fn=0.75**

λ/L_{pp}	*Wave Amplitude, A, (mm)*	*Steepness*	*Heave RAO* $\left(x_{3_1}/A\right)$	*Heave phase (deg)*	*Pitch RAO* $\left(x_{5_1}/kA\right)$	*Pitch phase(deg)*
1.596	18.082	0.024	2.32	-79.556	0.796	165.3
1.806	19.95	0.022	2.735	-51.66	1.082	172.44
1.983	14.00	0.015	2.669	-30.78	1.545	-177.3
2.012	14.00	0.014	2.604	-29.16	1.602	-173.88

Table A.11 CFD Results for 0^{th} harmonic Amplitude- **Fn=0.75**

λ/L_{pp}	*Wave Amplitude, A, (mm)*	*Steepness*	*Heave* $\left(x_{3,0}/A\right)$	*Pitch* $\left(x_{5,0}/kA\right)$
1.596	18.082	0.024	$1.88\ 10^{-3}$	$5.68\ 10^{-2}$
1.806	19.95	0.022	$1.65\ 10^{-3}$	$5.83\ 10^{-2}$
1.983	14.00	0.015	$1.83\ 10^{-3}$	$5.71\ 10^{-2}$
2.012	14.00	0.014	$1.84\ 10^{-3}$	$5.71\ 10^{-2}$

A.3 Effects of incoming wave steepness on ship response

Table A.12 CFD Results for ship motions for different wave steepness values- **Fn=0.75**

λ/L_{pp}	*Wave Amplitude, A, (mm)*	*Steepness*	*Heave RAO* (x_3/A)	*Heave phase (deg)*	*Pitch RAO* (x_5/kA)	*Pitch phase(deg)*
1.596	18.082	0.024	2.32	-79.556	0.796	165.3
1.806	19.95	0.022	2.735	-51.66	1.082	172.44
1.983	14.00	0.015	2.669	-30.78	1.545	-177.3
2.012	14.00	0.014	2.604	-29.16	1.602	-173.88
1.596	38.12	0.05	2.1429	-114.4	0.7376	160.3
1.806	43.13	0.05	2.589	-99.07	0.8	172.5
1.983	47.36	0.05	2.686	-77.4	1.056	-162.47
2.012	48.06	0.05	2.678	-9.936	1.112	-170.6
1.596	76.242	0.1	1.629	-74.66	0.7852	165.28
1.806	86.4	0.1	2.025	-34.568	0.9089	172.44
1.983	94.728	0.1	2.325	-12.423	0.9087	-177.3
2.012	96.114	0.1	2.3643	-9.22	0.8778	-179.5

A.4 Total resistance coefficient, C_T, for the catamaran advancing in regular head waves

Table A.13 CFD Results for ship advancing in waves- **Fn=0.45**

λ/L_{pp}	*Wave Amplitude, A, (mm)*	*Steepness*	$C_T\ (x10^{-3})$
1.001	18.559	0.038	7.04
1.201	17.813	0.031	7.18
1.396	18.039	0.027	7.05
1.595	17.409	0.023	6.93
1.991	18.236	0.019	6.88
Average Value=			**7.02**

Table A.14 CFD Results for ship advancing in waves- Fn=0.6

λ/L_{pp}	*Wave Amplitude, A, (mm)*	*Steepness*	$C_T\ (x10^{-3})$
1.393	18.801	0.028	5.99
1.49	19.151	0.0269	5.9
1.6	19.148	0.025	5.88
1.795	18.312	0.021	5.73
1.997	19.816	0.021	5.71
	Average Value=		**5.84**

Table A.15 CFD Results for ship advancing in waves- Fn=0.75

λ/L_{pp}	*Wave Amplitude, A, (mm)*	*Steepness*	$C_T\ (x10^{-3})$
1.596	18.082	0.024	4.67
1.806	19.95	0.022	4.67
1.983	14.00	0.015	4.56
2.012	14.00	0.014	4.55
	Average Value=		**4.61**

Table A.16 CFD Results for ship advancing in waves- Fn=0.75-Ak=0.05

λ/L_{pp}	*Wave Amplitude, A, (mm)*	*Steepness*	$C_T\ (x10^{-3})$
1.596	38.12	0.05	5.24
1.806	43.13	0.05	5.36
1.983	47.36	0.05	5.32
2.012	48.06	0.05	5.32
	Average Value=		**5.31**

Table A.17 CFD Results for ship advancing in waves- Fn=0.75-Ak=0.1

λ/L_{pp}	*Wave Amplitude, A, (mm)*	*Steepness*	$C_T\ (x10^{-3})$
1.596	38.12	0.1	6.69
1.806	43.13	0.1	7.42
1.983	47.36	0.1	8.78
2.012	48.06	0.1	8.07
	Average Value=		**7.66**

References

[1] Carrica, P., Wilson, R.V., Noack, R.W. & Stern, F. (2007). 'Ship motions using single-phase level set with dynamic overset grids'. Computers & Fluids, **36**, pp.1415-1433.

[2] Carrica, P., Wilson, R.V. & Stern, F. (2006). 'Unsteady RANS simulation of the ship forward diffraction problem'. Computers & Fluids, **35**, pp. 545-570.

[3] Carrica, P., Wilson, R.V. & Stern, F. (2007). 'An unsteady single-phase level-set method for viscous free surface flows'. International Journal of Numerical Methods in Fluids, **53(2)**, pp. 229-256.

[4] Cura Hochbaum, A. & Vogt, M. (2002). 'Towards the simulation of seakeeping and manoevering based on the computation of free surface viscous ship flow'. Proceedings of the 24th Symposium on Naval Hydrodynamics, Fukoka, Japan.

[5] Faltinsen, O. M. (2005). 'Hydrodynamics of high speed marine vehicles'. Cambridge University Press.

[6] Felli, M., Pereira, F., Calcagno, G. & Di Felice, F. (2002). 'Application of Stereo-PIV: Propeller wake analysis in a large circulating water channel'. International Symposium of Application of Laser Anemometry to Fluid Mechanics, Lisbon, Portugal.

[7] Fonseca, N., Soares, C.G. (2004a,b). 'Experimental investigation of the non-linear effects on the statistics of vertical motions and loads of a containership in irregular waves'. Journal of Ship Research, **48**, pp.148-167,148-167.

[8] Froude, W. 'The foundamental principles of resistance of ships' Transactions INA, 1955, pp.298-310.

[9] Froude, W. 'Experiments on the surface friction experienced by a plane moving through water'. Transactions INA, 1955, pp.138-146.

[10] Gerritsma, J., Beukelman, W.(1972). 'Analysis of the resistance increase in waves of a fast cargo ship'. International Shipbuilding Progr. **19**, pp.285-293.

[11] Gorsky, J.J. (2002) 'Present state of numerical ship hydrodynamics and validation experiments'. Transactions of ASME, 124, pp.74-80.

[12] Gui, L., Longo, J., Metclaff, B., Shao, J., Stern,F. (2001) 'Forces, moment, and wave pattern for surface combatant in regular head waves-part 1; measurement systems and uncertainty assessment'. Experiments in Fluids, 31, pp.674-680.

[13] ITTC-57. 'Skin friction and turbulence Committee Report'. Proceedings of the 8th International Towing Tank Conference, pp 71-227.

[14] ITTC 2005. Proceedings of the 24th International Towing Tank Conference, Edinburgh, Scotland.

[15] Irvine, M., Longo, J. & Stern, F. (2008). 'Pitch and heave tests and uncertainty assessment for a surface combatant in regular waves'. Journal of Ship Research, **52**, pp.146-163.

[16] Janson, C.E. (1997). 'Potential flow panel methods for the calculation of free surface flows with lift'. PhD Thesis. Chalmers University of Technology.

[17] Larsson, L., Stern, F. & Bertram, V. (2000). 'Gothenburg 2000: A workshop on numerical Ship Hydrodynamics', Gothenburg, Sweden.

[18] Lee, S.J, Koh, M.S. & Lee, C.M. (2003). 'PIV velocity field measurements of flow around a KRISO 3600 TEU container ship model'. Journal of Marine Science and Technology, **8**, pp. 76-87.

[19] Lewis, E.V. 'Principles of Naval Architecture-Vol II:Resistance, Propulsion and Vibrations'. Society of Naval Architects and Marine Engineers, 1989.

[20] Lugni, C., Colagrossi, A., Landrini, M., Faltinsen, O.M. (2004). 'Experimental and numerical study of semi-displacement monohull and catamaran in calm water and incident waves'. Proceedings of the 25th Symposium on Naval Hydrodynamics, Washington DC: Dept. of the Navy Office of Naval Research.

[21] Menter, F.R.(1994). 'Two equations eddy viscosity turbulence models for engineering applications'. AIAA Journal, **32**, pp.1598-1605.

[22] Molland, A.F., Wellicome, J.F., Couser, P.R. (1996). 'Resistance Experiments on a systematic series of high speed displacement catamaran hull forms: Variation of length-displacement ratio and breadth-draught ratio'. Transactions RINA, **138 pt A**, pp.55-72.

[23] Newman, J.N.(1977). 'Marine Ship Hydrodynamics'.Cambridge:The MIT Press.

[24] Noack, R. (2005). 'SUGGAR: a general capability for moving body overset grid assembly'. AIAA paper 2005-5117, 17th AIAA Computational Fluid Dynamics conference, Ontario, Canada.

[25] O'Dea, J.,Powers, E., Zselecsky, J. (1992). 'Experimental determination of non-linearities in vertical plane ship motions'. Proceedings, 8th International Conference on numerical ship hydrodynamics, Busan, Korea.

[26] Orihara, H., Miyata, H. (2003). 'A numerical method for arbitrary ship motions in arbitrary wave conditions using overlapping grid system'. Proceedings, 19th ONR Symposium on Naval Hydrodynamics, Seoul, Korea

[27] Paterson, E.G, Wilson, R. & Stern, F.(2003). 'General purpose parallel Unsteady RANS ship hydrodynamics code: CFDSHIP-Iowa'. IIHR Report No.432.

[28] Powering Performance Commitee (1990). 'Final report and recommendations to the 15th ITTC'. Proceedings of the 1990 American Towing Tank Conference, Ann Harbor Science.

[29] Prasad, A.K. (2000). 'Stereoscopic Particle Image Velocimetry'. Experiments in Fluids, **29**, pp.103-116.

[30] Proceedings of the SSPA-CTH-IIHR Workshop, 1990, Gothenburgh, Sweden.

[31] Proceedings of the CFD Workshop Tokyo, 1994, Ship Research Institute, Ministry of Transport, Ship & Ocean Foudation, Japan.

[32] Proceedings of the CFD Workshop Tokyo, 2005, National Maritime Research Institute, Tokyo, Japan.

[33] Raven, H.C. (1996). ' A solution method for the non-linear ship wave resistance problem'. PhD Thesis, Technical University of Delft.

[34] Resistance and Flow Committee (1996). 'Final report and recommendations to the 21st ITTC'. Proceedings of the 1996 American Towing Tank Conference, Ann Harbor Science.

[35] Salvensen, N., Tuck, E.O. & Faltinsen, O. (1970). 'Ship motions and sea loads'. Transactions of the society of Naval Architects and marine engineers, **78**, pp.250-287.

[36] Sato, Y., Miyata, H. & Sato, T. (1999). 'CFD Simulation of 3-dimensional motion of a ship in waves: application to an advancing ship in regular head waves'. Marine Science and Technology, **4**, pp.108-116.

[37] Salvensen, N., Tuck, E.O., Faltinsen, O.M. (1970). 'Ship motions and sea loads'. Transactions SNAME, **78**, pp.250-287.

[38] Schlitching, H.(1979). 'Boundary layer theory'.New York:McGraw Hill Book Company.

[39] Simonsen, C., Otzen, J. & Stern, F. (2008). ' EFD and CFD for KCS heaving and pitching in regular head waves'. Proceedings of the 27 th Symposium on Naval Hydrodynamics, Seoul, Korea.

[40] Stern, F., Wilson, R.V., Coleman, H., Paterson, E.G. (2001). 'Comprehensive approach to Verification & Validation of CFD simulations-Part 1: Methodology and Procedures'. Journal of Fluids Engineering, **123**, pp.793-802.

[41] Stern, F., Carrica, P., Kandasamy, M., Gorsky, J., O'Dea, J., Hughes, M., Miller, R., Hendrix, D., Kring, D., Milewsky, W., Hoffman, R., Cary, C. 'Computational Hydrodynamic tools for high-speed saelift'. IIHR Report No.465.

[42] Stern, F., Wilson, R., Longo, J., Carrica, P., Xing,T., Tahara, Y., Simonsen, C., Kim, J., Shao, J., Irvine, M., Kandasamy, M., Ghosh, S., Weymouth, G. (2003). ' Paradigm for development of simulation based design for ship hydrodynamics'. The 8th International Conference on Numerical Ship Hydrodynamics, Busan, Korea.

[43] Tursini, L. (1953). 'Leonardo da Vinci and the problems of navigation and naval design'. Transactions INA, **95**, pp.97-102.

[44] Van't Veer, R. (1998). 'Experimental results of motions, hydrodynamic coefficients and wave loads on the 372 Catamaran model'. Delft University Report 1129.

[45] Van't Veer, R. (1998). 'Experimental results of motions and structural loads on the 372 Catamaran model in head and oblique waves'. Delft University Report 1130.

[46] Weymouth, G.D., Wilson, R.V. & Stern, F. (2005). 'RANS Computational fluid dynamics predictions of pitch and heave ship motions in haed seas'. Journal of Ship Research, **49**, pp.80-97.

[47] Wilson, R. V., Carrica, P. & Stern, F. (2005). 'Unsteady RANS method for ship motions with application to roll for a surface combatant'. Computers & Fluids, **35**, pp.501-524.

[48] Xing, T., Carrica, P. & Stern, F. (2008). "Computational Towing Tank Procedures for Single Run Curves of Resistance and Propulsion'. Submitted for publication in ASME Journal of. Fluids Engineering.

Acknowledgements

I would like to deeply thank Prof. Sergio Bova and Prof. Fred Stern, who gave me the opportunity to undertake a very interesting path in the field of ship hydrodynamics, for their dedication, their interest, their personal and professional support and for the care with which they reviewed the manuscript.

My thanks to Prof. Sergio Rizzuti for reading the manuscript and for his valuable comments.

My thanks to Dr. Mani Kandasamy of University of Iowa for his precious guide to the code use, his helpful collaboration, his patience and his friendship.

Many thanks to Ernesto Ramundo and Renato Bentrovato, who with their valuable work, set up the circulating channel in very short time.

I want also to thank Mrs. Assunta and Mrs. Antonella. Their friendship and professional collaboration meant a great deal for me. It was an honor for me to work with all the staff of the Department of Mechanical Engineering.